

INFLUENCE OF ANNEALING TREATMENT ON THERMOELECTRIC
PROPERTIES OF ANTIMONY TELLURIDE AND BISMUTH TELLURIDE
FILMS DEPOSITED BY DC MAGNETRON SPUTTERING TECHNIQUE FOR
THERMOELECTRIC GENERATOR APPLICATIONS



A THESIS SUBMITTED IN PARTIAL FULFILLMENT OF THE REQUIREMENT FOR
THE DEGREE OF DOCTOR OF SCIENCE IN APPLIED PHYSICS
DEPARTMENT OF PHYSICS SCHOOL OF SCIENCE
KING MONGKUT'S INSTITUTE OF TECHNOLOGY LADKRABANG

2021

KMITL- 2021-SC-D-030-052

This material is reserved for educational use only, not allowed for commercial use.

Forbidden to modify the content, and cite the document when use.



COPYRIGHT 2021

SCHOOL OF SCIENCE

KING MONGKUT'S INSTITUTE OF TECHNOLOGY LADKRABANG

This material is reserved for educational use only, not allowed for commercial use.

Forbidden to modify the content, and cite the document when use.

หัวข้อวิทยานิพนธ์	อิทธิพลของการอบอ่อนต่อสมบัติทางเทอร์โมอิเล็กทริกของฟิล์มแอนติมอโนเทลลูไรด์และบิสมัทเทลลูไรด์ปลูกโดยเทคนิคซีแมกนีตรอนสปัตเตอริงสำหรับนำไปประยุกต์ใช้เป็นเทอร์โมอิเล็กทริกเจเนอเรเตอร์
ชื่อนักศึกษา	ศุภศักดิ์ เขียนวิมล
รหัสประจำตัว	61605125
ปริญญา	ปรัชญาดุษฎีบัณฑิต (ฟิสิกส์ประยุกต์)
ภาควิชา	ฟิสิกส์
พ.ศ.	2564
อาจารย์ที่ปรึกษาวิทยานิพนธ์	รองศาสตราจารย์ดร.อาภาภรณ์ สุกุลการะเวก

บทคัดย่อ

งานวิจัยนี้ได้ทำการเปรียบเทียบสมบัติทางเทอร์โมอิเล็กทริกและปัจจัยความเข้ากันได้ของฟิล์มแอนติมอโนเทลลูไรด์และบิสมัทเทลลูไรด์ปลูกโดยเทคนิคซีแมกนีตรอนสปัตเตอริงสำหรับนำไปประยุกต์ใช้เป็นเทอร์โมอิเล็กทริกเจเนอเรเตอร์ ฟิล์มบิสมัทเทลลูไรด์มีความเป็นผลึกสูงกว่าแอนติมอโนเทลลูไรด์เนื่องจากพลังงานที่ใช้ในการก่อตัวของบิสมัทเทลลูไรด์ต่ำกว่าแอนติมอโนเทลลูไรด์ ความหนาแน่นของพาหะของฟิล์มแอนติมอโนเทลลูไรด์มีค่าเพิ่มขึ้นแต่ความหนาแน่นของพาหะของฟิล์มบิสมัทเทลลูไรด์ลดลงเนื่องจากการระเหยของอะตอมเทลลูเรียมในกระบวนการอบอ่อน ค่าสัมประสิทธิ์ซีเบคของฟิล์มแอนติมอโนเทลลูไรด์และบิสมัทเทลลูไรด์มีค่าแปรผกผันกับค่าความหนาแน่นของพาหะ หลังจากการอบอ่อนค่าสภาพนำไฟฟ้าของฟิล์มแอนติมอโนเทลลูไรด์มีค่าเพิ่มขึ้นมากกว่าบิสมัทเทลลูไรด์เนื่องจากการเปลี่ยนแปลงของค่าสภาพคล่องของพาหะและค่าความหนาแน่นของพาหะ การเพิ่มขึ้นของค่าสภาพนำความร้อนของฟิล์มแอนติมอโนเทลลูไรด์และบิสมัทเทลลูไรด์เนื่องจากปัจจัยของความเป็นผลึกของฟิล์ม หลังจากการอบอ่อนประสิทธิภาพเทอร์โมอิเล็กทริกของฟิล์มแอนติมอโนเทลลูไรด์และบิสมัทเทลลูไรด์มีค่าประมาณ 0.5 และ 0.25 ตามลำดับที่อุณหภูมิ 513 องศาเซลวิน ปัจจัยความเข้ากันได้ของฟิล์มแอนติมอโนเทลลูไรด์และบิสมัทเทลลูไรด์มีค่าไม่เกิน 2 การออกแบบขนาดของขาเทอร์โมอิเล็กทริกโดยใช้ค่าสภาพนำไฟฟ้าและค่าสภาพนำความร้อนของฟิล์มที่ผ่านกระบวนการอบอ่อน ในการประดิษฐ์เทอร์โมอิ

เล็กทรอนิกส์เนอเรเตอร์ต้องใช้มาส์กที่จำเป็น 3 ชั้นสำหรับแอนติโมนีเทลลูไรด์ บิสมัทเทลลูไรด์ และ
ซั้วไฟฟ้า(ทองแดง) โดยขนาดของเทอร์โมอิเล็กทริกเจเนอเรเตอร์ที่สมบูรณ์แล้วมีขนาด 140x36x1.1
ลูกบาศก์มิลลิเมตร เทอร์โมอิเล็กทริกเจเนอเรเตอร์แบบปิดงอได้สามารถสร้างแรงดันไฟฟ้าวงจรเปิดได้
ประมาณ 32 มิลลิโวลต์และกำลังไฟฟ้าสูงสุดได้ 3.2 ไมโครวัตต์ที่ความแตกต่างของอุณหภูมิเท่ากับ 40
องศาเซลเซียสและยังสามารถสร้างแรงดันไฟฟ้าวงจรเปิดได้ประมาณ 1.5 มิลลิโวลต์จากความร้อนจากร่างกายมนุษย์

คำสำคัญ : เทอร์โมอิเล็กทริกเจเนอเรเตอร์แบบปิดงอได้ การอบอ่อน แอนติโมนีเทลลูไรด์ บิสมัทเทลลูไรด์



Thesis Title	Influence of annealing treatment on thermoelectric properties of antimony telluride and bismuth telluride films deposited by DC magnetron sputtering technique for thermoelectric generator applications
Student Name	Supasak Kianwimol
Student ID	61605125
Degree	Doctor of Philosophy (Applied physics)
Department	Physics
Year	2021
Thesis Advisor	Assoc. Prof. Dr. Aparpon Sakulkalavek

Abstract

In this study, compared the thermoelectric properties and compatibility factors of n-Bi₂Te₃ and p-Sb₂Te₃ films deposited by direct current magnetron sputtering for thermoelectric generator applications. The n-Bi₂Te₃ was more crystalline than p-Sb₂Te₃, since the formation energy of n-Bi₂Te₃ was lower than that of p-Sb₂Te₃. The carrier concentration of p-Sb₂Te₃ increased, whereas that of n-Bi₂Te₃ decreased because some Te evaporated during annealing. The Seebeck coefficient of p-Sb₂Te₃ and n-Bi₂Te₃ was inversely proportional to the carrier concentration. The electrical conductivity of the annealed p-Sb₂Te₃ increased more than that of annealed n-Bi₂Te₃, owing to the changed mobility and carrier concentration. Crystallization was the main factor enhancing the thermal conductivity. The highest figure of merit achieved from the annealed p-Sb₂Te₃ was ~0.5 and for n-Bi₂Te₃ ~0.25, at 513 K. Both annealed n-Bi₂Te₃ and p-Sb₂Te₃ had appropriate compatibility factors, differing by a factor < 2. To design geometric cross-sectional areas of the thermocouple legs with electrical and thermal conductivity from annealed film condition. The fabrication method of the prototype necessary 3 masks, two for p-Sb₂Te₃ and n-Bi₂Te₃ deposition and last one for electrode (Cu). The archived

thermoelectric generator has an are approximately $140 \times 36 \times 1.1 \text{ mm}^3$. The flexible thermoelectric generator generated maximum of open circuit output voltage about 32 mV and maximum output power about 3.2 μW at 40 K different temperature. The open circuit output voltage with heat from human body was generated about 1.52 mV.

Keywords :Flexible thermoelectric generator; Annealing treatment; Antimony telluride; Bismuth telluride



Acknowledgements

This thesis was successfully completed by supporting my advisor Assoc. Prof. Dr. Aparporn Sakulkalavek for her guidance and support throughout my thesis. I would like to thank King Mongkut's Institute of Technology Ladkrabang for student fund support. I would like to thanks to Professor Dr. John Morris and who review and comment and proofreading several chapters of this manuscript. Special thanks to Assoc. Prof. Dr. Rachsak Sakdanuphab and College of Advanced Manufacturing Innovation, King Mongkut's Institute of Technology Ladkrabang for provide assistance in the use of research equipment and tools. I also would like to thank the lab group members and all those who helped me to stay focused on completing the thesis and who have provided me with the encouragement to continue when the going got tough. The author gratefully acknowledges the support Optical Thin-Film Technology Laboratory, NSTDA, Thailand, for carrying out Hall measurements, the Rajamangala University of Technology Suvarnabhumi for ZEM-3 measurements.

Mr. Supasak Kianwimol

Table of contents

	Page
Abstract in Thai	i
Abstract in English	iii
Acknowledgements	v
Table of contents	vi
List of tables	x
List of figures	xi
Chapter 1 Introduction	1
1.1 Research Motivation	1
1.2 Objectives of the study	2
1.3 Scope of the study	3
1.4 Benefits of the study	3
Chapter 2 Theory and literature reviews	4
2.1 Thermoelectric phenomena and their parameters	4
2.1.1 Seebeck Effect	5
2.1.2 Peltier Effect	6
2.1.3 Thomson Effect	8
2.1.4 Figure of Merit	9
2.1.5 Seebeck Coefficient	10
2.1.6 Electrical resistivity and Electrical conductivity	11
2.1.7 Carrier mobility	13
2.1.8 Thermal conductivity	18
2.2 Thermoelectric Applications	21
2.2.1 Thermoelectric power generator (TEG)	23
2.2.2 Thermoelectric cooling (TEC)	25
2.3 Antimony telluride thermoelectric material	26
2.4 Bismuth Telluride thermoelectric material	28

Table of contents (continue)

	Page
2.5 The film deposition process	30
2.5.1 Chemical Vapor Deposition (CVD)	31
2.5.2 Physical Vapor Deposition (PVD)	31
2.5.3 Advantages and Disadvantages of film deposition	31
2.6 Sputtering process	32
2.6.1 Sputtered atoms	35
2.6.2 Sputtering yield	38
2.6.3 The practical aspect of sputtering systems	41
2.7 Characterization techniques	46
2.7.1 X-ray diffraction (XRD)	46
2.7.2 Field-emission scanning electron microscopy (FE-SEM)	49
2.7.3 Hall effect measurement	51
2.7.4 Seebeck Coefficient/Electrical Resistance Measurement System (ZEM-3)	54
2.7.5 Thin Film Analyzer (TFA)	55
2.7.6 X-Ray Photoelectron Spectroscopy	59
2.8 Literature Reviews	61
Chapter 3 Research methodology	66
3.1 Development of thermoelectric properties of bismuth telluride thick film deposited by DC magnetron sputtering via post-annealing treatment	66
3.1.1 Material and equipment	66
3.1.2 Experimental procedures	68
3.2 Development of thermoelectric properties of p-Sb ₂ Te ₃ and n-Bi ₂ Te ₃ films deposited by DC magnetron sputtering via post-annealing treatment	70
3.2.1 Material and equipment	70

Table of contents (continue)

	Page
3.2.2 Experimental procedures	71
3.2.3 Material and equipment	72
3.3 Design and fabricate thermoelectric generator	73
3.4 Characterizations	79
3.4.1 X-ray Diffraction	79
3.4.2 Field-emission scanning electron microscopy	80
3.4.3 Hall effect measurement	82
3.4.4 Seebeck Coefficient/Electrical Resistance Measurement System	83
3.4.5 Thin Film Analyzer (LINSEIS TFA)	85
3.4.6 X-Ray Photoemission spectroscopy	87
3.4.7 The measurement thermoelectric generator as functions of different temperature between hot and cold junctions	88
Chapter 4 Result and discussion	90
4.1 Effect of annealing temperature on thermoelectric properties of bismuth telluride thick film deposited by DC magnetron sputtering	90
4.2 Comparison of the thermoelectric properties of Bi_2Te_3 and Sb_2Te_3 films deposited via the DC magnetron sputtering technique	104
4.3 Fabricate and measuring power output from thermoelectric generator	118
Chapter 5 Conclusion	121
5.1 Effect of annealing temperature on thermoelectric properties of bismuth telluride thick film deposited by DC magnetron sputtering	121
5.2 Comparison of the thermoelectric properties of Bi_2Te_3 and Sb_2Te_3 films deposited via the DC magnetron sputtering technique	121
5.3 Fabricate and measuring power output from thermoelectric generator	122

Table of contents (continue)

	Page
References	123
Appendices	130
Appendix A	131
Appendix B	139
Author biography	148



List of tables

Table	Page
2.1 Several techniques of the film deposition	30
3.1 Conditions used for the deposition of Bi_2Te_3 thick films by DC magnetron sputtering with different post-annealing temperature	68
3.2 Conditions used for the deposition of the p- Sb_2Te_3 and n- Bi_2Te_3 films	72
3.3 Data for calculate leg area of the p- Sb_2Te_3 and n- Bi_2Te_3 films	74
4.1 Calculated average grain size and Te content of thick Bi_2Te_3 films annealed at different temperatures	95
4.2 Room-temperature power factor of thick Bi_2Te_3 films deposited by various techniques	102
4.3 Chemical composition, RMS roughness and mean grain size from as-deposited and annealed films	107
4.4 Electrical properties of as-deposited and annealed films at room temperature	109
4.5 Different deposited conditions and thermoelectric properties of p- Sb_2Te_3 and n- Bi_2Te_3 films deposited by DC magnetron sputtering at 513 K	115
4.6 Electrical conductivity and lattice thermal conductivity of n- Bi_2Te_3 at room temperature with various dopants	117
4.7 A comparable maximum output power of TEG device with different method and substrate	119

List of figures

Figure	Page
2.1 A temperature difference creates a potential difference in the junction between material A and B	5
2.2 A thermal gradient exists at the junction of dissimilar materials when an electrical current flows	7
2.3 the absorption of heat by current carrying conductor exposed to a temperature gradient	8
2.4 Carrier concentration on thermoelectric properties of a material	12
2.5 Carrier scattering from an ionized As donor	14
2.6 Temperature dependence on carrier mobility due to lattice and impurity scattering with a various donor concentration of semiconductor	16
2.7 Temperature dependence on electrical conductivity, carrier concentration and carrier mobility	17
2.8 Schematic of the thermoelectric module	23
2.9 The schematics of (a) thermoelectric generator and (b) thermoelectric cooling	25
2.10 Atomic layers of Sb_2Te_3 crystal structure. Dash line indicates van der Waals gap of one quintuple layer (QL)	27
2.11 Hexagonal unit cell of (a) Bi_2Te_3 and (b) $BiTe$ with the base vectors indicated by the black arrows	29
2.12 Physical sputtering process	33
2.13 Schematic of the magnetron sputtering system	35
2.14 (a) Kinetic energy transfer (b) kinetic energy transfer between two masses in the forward direction	37
2.15 DC power of the sputtering system	43
2.16 Mass flow controller	44
2.17 Schematic diagram of substrate temperature	45
2.18 Bragg's law	47

List of figures (continue)

Figure	Page
2.19 Schematic of field-emission scanning electron microscope	49
2.20 Signals generated at electron-specimen interactions	51
2.21 Hall effect measurement set up	53
2.22 Schematic of van der pawn set up (a) for material resistivity and (b) for hall voltage measurements	54
2.23 Schematic of Seebeck Coefficient/Electrical Resistance Measurement System	55
2.24 Cut through the chip (a) and schematic cross-sectional view of the big membrane including thermometer (b). Top view of the two-membrane setup including heating stripes and resistance thermometer. $I_{Mi,A}$, $I_{Mi,B}$ as well as $V_{Mi,A}$, and $V_{Mi,B}$ are the current and voltage connection pads for the two heaters on membranes 1 and 2, I_{RT} and V_{RT} are the connection pads for the resistance thermometer, and $V_{TH,H}$ is the pad for the hot contact of the thermovoltage measurement (c)	59
2.25 X-Ray Photoelectron Spectroscopy Measurement System	59
2.26 Influence of sputtering power on (a) structural and (b) power factor of films	61
2.27 Influence of sputtering pressure on (a) structural and (b) power factor of films	62
2.28 Influence of annealing treatment on (a) structural and (b) power factor of films	63
2.29 Influence of annealing treatment on (a) structural and (b) power factor of films	64
2.30 show (a) A pair of p–n couple of the device, and parameters that specify the dimension of the device (b) Photograph of fabricated flexible TEG on Kapton HN. and schematic of flexible thermoelectric generator	65
3.1 Schematic of DC magnetron system	67

List of figures (continue)

Figure	Page
3.2 (a) Photograph of thick bismuth telluride film deposited by DC magnetron sputtering on a flexible substrate. (b) Schematic illustration of apparatus for measuring power output from thick, single-leg Bi ₂ Te ₃ film. (c) Infrared top-view image of Bi ₂ Te ₃ film taken during measurement	69
3.3 Experimental procedures of the preparation of p-Sb ₂ Te ₃ and n-Bi ₂ Te ₃ films via DC magnetron sputtering technique	71
3.4 Set up heat treatment system in a vacuum chamber	72
3.5 (a) The main geometrical scale of the device (b) the prototype of thermoelectric generator	75
3.6 the prototype of thermoelectric generator (a) P-type (Sb ₂ Te ₃) (b) N-type (Bi ₂ Te ₃) and (c) Electrode (Cu)	76
3.7 (a) The mask for fabricate thermoelectric generator (b) Mask with sputtered film and (c) sputtered film	76
3.8 Photograph of TEG integrates 6 thermocouples on Kapton substrate	77
3.9 (a) Model and (b) photograph of two TEG integrates were connected with silver conductive paint	77
3.10 (a) Model and (b) photograph of two TEG integrates were connected with (for hot), and silicone (for cool)	78
3.11 (a) Sample holder (b) SmartLab Studio II software	79
3.12 X-ray diffraction (Rigaku diffractometer Smartlab)	80
3.13 Field-emission scanning electron microscopy (JSM-7001F)	81
3.14 (a) hall measurement state (b) sample mounting parts	82
3.15 Hall effect measurement system (Ecopia, HMS-3000)	83
3.16 (a) sample clamping block (b) Seebeck coefficient and electrical resistance measurement system software (V3.5 for SDC35)	84
3.17 Seebeck Coefficient/Electrical Resistance Measurement System (Ulvac RIKO)	85

List of figures (continue)

Figure	Page
3.18 Thin Film Analyzer (LINSEIS TFA)	85
3.19 (a) Diagram of the chip ZT test structure for Van der Pauw, Seebeck coefficient, and 3ω thermal conductivity measurement, (b) the chip with shadow mask, before deposition	86
3.20 The schematic of test chip for thermoelectric properties (Seebeck coefficient, electrical conductivity and thermal conductivity) measurement	87
3.21 (a) samples were prepared in dimension of 1x1 cm and attached to the microscope slide (b) X-Ray Photoemission spectroscopy measurement system software	87
3.22 X-Ray Photoemission spectroscopy at Synchrotron Light Research Institute	88
3.23 Schematic illustration of equipment for measuring open circuit output voltage and output power of the thermoelectric generator from TEG flexible thin films	89
3.24 (a) Schematic illustration of apparatus for measuring power output and (b) Infrared top-view image of thermoelectric module taken during measurement	89
3.25 (a) Infrared top-view image of thermoelectric module taken during measurement and (b) Thermoelectric generator open circuit output voltage (V_{OC}) with body heat human	89
4.1 X-ray diffraction patterns from thick Bi ₂ Te ₃ films annealed for 30 minutes at various temperatures	90

List of figures (continue)

Figure	Page
4.2 XPS spectra of as-deposited and annealed bismuth telluride thick films. (a) Bi 4f core level with binding energies of 157.5 and 163 eV, corresponds to the states of Bi 4f _{7/2} and 4f _{5/2} . (b) Te 3d core level with binding energies of 572.5 and 583 eV, corresponds to the states of Te 3d _{5/2} and 3d _{3/2} . The inset shows peaks fitting XPS data of Bi 4f _{7/2} and 4f _{5/2} for unbound (Bi) and bound (Bi ³⁺) chemical states of annealed films at 150 °C (c) and 250 °C (d), and peaks fitting XPS data of Te 3d _{5/2} and 3d _{3/2} for unbound (Te) and bound (Te ²⁻) chemical states of annealed films at 150 °C (e) and 250 °C (f)	92
4.3 Schematics of defect generation in Bi ₂ Te ₃ atomic structure from the annealing process. In step 1, V_{Te} is formed by the volatile of tellurium atoms on surface. step 2, a Bi_{Te}-V_{Bi} pair is formed by the migration of bismuth atom from an adjacent Bi site	93
4.4 Cross section of thick Bi ₂ Te ₃ films (a) as-deposited and annealed at (b) 150 °C, (c) 250 °C, and (d) 350 °C	95
4.5 (a) Carrier concentration and mobility; (b) mean free path and mobility of thick Bi ₂ Te ₃ films annealed at different temperatures	97
4.6 (a) Electrical conductivity, (b) Seebeck coefficient, and (c) power factor as functions of applied temperature for thick Bi ₂ Te ₃ films annealed at different temperatures	99
4.7 Power factor as a function of electrical conductivity for thick Bi ₂ Te ₃ films annealed at different temperatures	101
4.8 Power output of single-leg, thick, thermoelectric Bi ₂ Te ₃ film as a function of temperature difference for as-deposited film and film annealed at 250 °C	103
4.9 X-ray diffraction spectra of the as-deposited (a) p-Sb ₂ Te ₃ and (b) n-Bi ₂ Te ₃ films annealed at 200 °C	104

List of figures (continue)

Figure	Page
4.10 Optimal annealing temperatures for improving the thermoelectric properties of p-Sb ₂ Te ₃ and n-Bi ₂ Te ₃ obtained from LV et. el.[12], Fang et. el.[19], Junlabhut et. el.[20], Zeng et. el.[21], Wang et. el.[23], Kianwimol et. el.[25], Hong et. el.[27], Wang et. el.[28], , Lin et. el.[29], and Hosokawa et. el.[30]	105
4.11 Atomic force microscopy (2D) topography of as-deposited and annealed (a-b) p-Sb ₂ Te ₃ and (c-d) n-Bi ₂ Te ₃ films	106
4.12 FE-SEM images and cross-sections of the as-deposited (a-d) p-Sb ₂ Te ₃ and (e-h) n-Bi ₂ Te ₃ thin films annealed at 200 °C	108
4.13 (a) Electrical conductivity and (b) Seebeck coefficient vs applied temperature for as-deposited and annealed films	110
4.14 Temperature dependent (a) total thermal conductivity, (b) calculated Lorentz numbers, (c) electronic thermal conductivity and (d) lattice thermal conductivity for as-deposited and annealed films	112
4.15 Dimensionless figure of merit vs applied temperature for as-deposited and annealed films	114
4.16 Thermoelectric compatibility factor, S, of as-deposited and annealed p-Sb ₂ Te ₃ and n-Bi ₂ Te ₃ films	116
4.17 Prototype flexible thermoelectric module	118
4.18 (a) Thermoelectric generator open circuit output voltage (V _{OC}) and output power (P _{out}) of the generator as functions of different temperature gradients	118
4.19 Thermoelectric generator open circuit output voltage (V _{OC}) with body heat human	120

Chapter 1

Introduction

1.1 Research Motivation

Thermoelectric techniques are used in a wide temperature range as power generators, solid-state coolers and sensors due to many attractive features, such as clean and noiseless energy without discharging any hazardous substance, high reliability and long lifetime [1,2]. The amount of generator electrical power being produced from TEG depends on material properties (ZT) and a temperature difference between two sides of the module. The thermoelectric figure of merit (ZT), used to characterize the performance of a thermoelectric material, is defined in equation 1.

$$ZT = \frac{S^2 \sigma T}{K} \quad (1.1)$$

Where

S is Seebeck coefficient (V/K)
 σ is Electrical conductivity (S/m)
 K is Thermal conductivity (W/Km)
 T is Temperature (K)

Antimony telluride (Sb_2Te_3) and Bismuth telluride (Bi_2Te_3) are the most interesting thermoelectric materials that have been used widely due to high ZT value, and high performance at room temperature. The ZT value can be made to increase when improvements are made to low-dimensional materials due to the influences of quantum confinement effect and phonon scattering on nano-structured materials [3,4]. The thermoelectric devices are two kinds: bulk and thin film. The thermoelectric film has a low dimensional that less thermal conductivity than bulk thermoelectric and enhance the figure of merit value [5-9].

Several research deposited p- Sb_2Te_3 and n- Bi_2Te_3 thin films using various techniques such as evaporation [10-12], metal organic chemical vapor deposition (MOCVD) [13], molecular beam epitaxy (MBE) [14] pulse laser deposition (PLD) [15] and sputtering

[5,16-25]. This work, the direct current (DC) magnetron sputtering technique was selected due to extremely high adhesion, produces high quality films and excellent uniformity over a large substrate area [16,26]. In addition, annealing treatment was used to improve thermoelectric properties of p-Sb₂Te₃ and n-Bi₂Te₃ thin films [12,19-30]. According to the annealing treatment can be adjusted the carrier concentration, surface defect and grain size [20]. However, the comparison of annealing treatment on thermoelectric properties of p-Sb₂Te₃ and n-Bi₂Te₃ thin films prepared direct current (DC) magnetron sputtering has hardly been discussed.

In this study, the p-Sb₂Te₃ and n-Bi₂Te₃ film were deposited by DC magnetron sputtering using a single stoichiometric compound target. The influence of annealing treatment on the chemical composition, structural, electrical and thermoelectric properties between p-Sb₂Te₃ and n-Bi₂Te₃ were compared and discussed. The designed thermoelectric generator from the thermoelectric properties of annealed p-Sb₂Te₃ and n-Bi₂Te₃ film were also applied for the fabricate of thermoelectric generator and measurer power output from thermoelectric generator.

1.2 Objectives of the study

The objective of this thesis is conducted in order to

- 1) Study the influence of annealing treatment on the chemical composition, structural, electrical and thermoelectric properties between p-Sb₂Te₃ and n-Bi₂Te₃ film deposited by DC magnetron sputtering.
- 2) Study the designing thermoelectric generator from the thermoelectric properties of annealed p-Sb₂Te₃ and n-Bi₂Te₃ film.
- 3) Study the fabrication thermoelectric generator and measuring power output from thermoelectric generator.

1.3 Scope of the study

The scope of this thesis is as follows:

- 1) The p-Sb₂Te₃ and n-Bi₂Te₃ films were deposited by using DC magnetron sputtering via post- annealing treatment at temperature 200 °C for 30 min.
- 2) Characterization chemical composition, structural, electrical and thermoelectric properties of as-deposited and annealed p-Sb₂Te₃ and n-Bi₂Te₃ films by following techniques:
 - 2.1) Energy dispersive spectrometry (EDS)
 - 2.2) Field emission scanning electron microscope (FE-SEM)
 - 2.3) X-ray diffractometer (XRD)
 - 2.4) Hall effect measurement (Hall)
 - 2.5) Thin film analyzer (TFA)
- 3) Design thermoelectric generator from the thermoelectric properties of annealed p-Sb₂Te₃ and n-Bi₂Te₃ film.
- 4) Fabricate thermoelectric generator.
- 5) Measuring power output from thermoelectric generator.

1.4 Benefits of the study

- 1) The optimization of p-Sb₂Te₃ and n-Bi₂Te₃ thermoelectric films was studied and clarified.
- 2) The relevant parameters of the deposited such as suitable sputtering parameters, thermoelectric properties, annealing conditions and thickness will be notified.
- 3) The relevant key parameters chemical composition, structural, electrical and thermoelectric properties of as-deposited and annealed p-Sb₂Te₃ and n-Bi₂Te₃ films has been clearly understood.
- 4) A prototype of the thermoelectric generator using optimized p-Sb₂Te₃ and n-Bi₂Te₃ was achieved.

Chapter 2

Theory and literature reviews

In overview, the objective of this chapter is to investigate the fundamental of thermoelectric, thermoelectric applications, antimony telluride and bismuth telluride thermoelectric material film deposition techniques, and the characterization technique. In this chapter, the relevant theories and literature reviews are explained.

2.1 Thermoelectric phenomena and their parameters

The advent of thermoelectric devices discovered in 1821 when Thomas Johann Seebeck found the deviation of a compass needle due to two junctions of two dissimilar materials at different temperatures. This now called Seebeck effect was caused by the formation of an electric potential difference due to a temperature difference. In 1834 Jean Peltier discovered that an electric current passes through two dissimilar materials alter the temperature at the junction. It called the Peltier effect. Some years later, Thomson explained found that the connection between the Seebeck effect and the Peltier effect within the framework of thermodynamics, known as the Thomson effect. All thermoelectric phenomena are described. These effects are the phenomenological foundations for the description of thermoelectric materials and the functioning of thermoelectric devices and thermoelectric application.

2.1.1 Seebeck Effect

The Seebeck effect is the relation between electrical potential and a temperature gradient. The increase of the electrical potential is occurred due to a temperature difference. Seebeck gave an overview of several material combinations applicable in thermocouples.

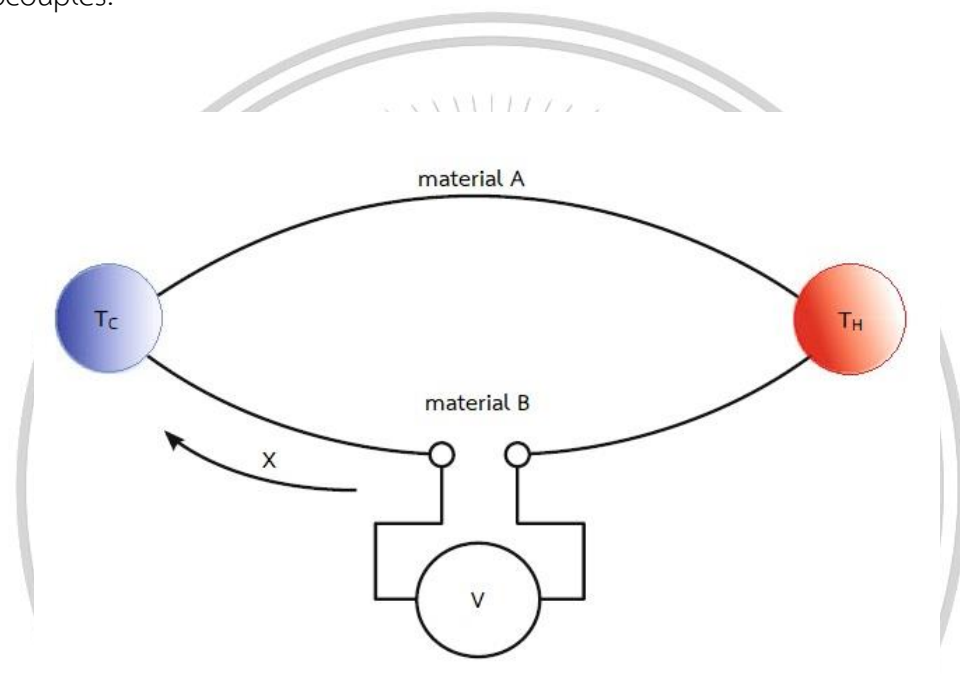


Figure 2.1 A temperature difference creates a potential difference in the junction between material A and B.

A thermocouple consists of two junctions of two dissimilar materials. The two junctions are held at the temperatures T_C and T_H , experiencing a temperature difference (ΔT) and thus exhibit a temperature gradient along with the materials. A temperature difference causes the majority carriers (electrons and holes) in the material to migrate from the hot side to the cold side. The minority carriers are left at the hot side thus giving rise to a thermoelectric voltage. The buildup of charge carriers on the cold side eventually ceases when an equal amount of charge carriers drift back to the hot side as a result of

the electric field created by the charge separation. At this point, the materials reach a steady state. The given temperatures difference generates a thermoelectric voltage difference (ΔV) measured at the device contacts:

$$\Delta V \propto \Delta T \quad (2.1)$$

The Seebeck coefficient (S) is defined via the limit at infinitesimal temperatures difference:

$$S(T) = \lim_{\Delta T \rightarrow 0} \frac{\Delta V}{\Delta T} \quad (2.2)$$

The total thermoelectric voltage is obtained.

$$dV = \int_{T_c}^{T_h} S(T) dT \quad (2.3)$$

The temperature dependent Seebeck coefficient along two different materials allows expressing a combined coefficient for the material couple under given thermal conditions.

$$\Delta V = (S_A - S_B) \int_{T_c}^{T_h} dT = (S_A - S_B) \Delta T \quad (2.4)$$

Where S_A and S_B are a Seebeck coefficient of material A and B. while P -type materials possess a positive Seebeck coefficient, N -type materials offer negative ones. The thermoelectric voltages drive current flowing through the materials when their junction kept the temperature difference [31].

2.1.2 Peltier Effect

The Peltier effect is a phenomenological effect reverse to the Seebeck effect. When an electric current passes through two dissimilar materials are connected at two junctions, heat can be absorbed in the junction, while it is released at the other one. As a result, heat flux through the materials is induced. The heat flux at the junction will be interpreted as energy conservation within the junctions and the change of total energy of

the carriers when electrical current passing. The Peltier coefficients represent how much heat current is carried per unit change through a material. The Peltier heat (Q) absorbed by the cold junction per unit time is given by [31-32]

$$dQ \propto IdT \quad (2.5)$$

$$\frac{dQ}{dT} = (\Pi_A - \Pi_B)I \quad (2.6)$$

In this equation, Π_A and Π_B are the Peltier coefficients of the materials A and B. The unit of the Peltier coefficient is W/A or V . Furthermore, the Peltier coefficients are also temperature dependence like the Seebeck coefficients. The Peltier coefficient and the Seebeck coefficient are related to each other by the first Kelvin relation. The relation is given by:

$$(\Pi_A - \Pi_B) = (S_A - S_B)T \quad (2.7)$$

$$\Pi_{AB} = S_{AB}T \quad (2.8)$$

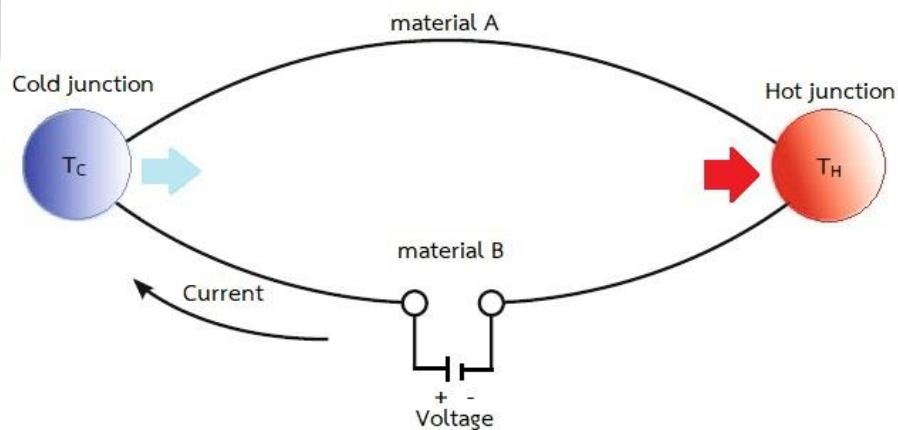


Figure 2.2 A thermal gradient exists at the junction of dissimilar materials when an electrical current flows.

2.1.3 Thomson Effect

The Thomson effect was predicted and observed the third thermoelectric effect by William Thomson (Lord Kelvin). It refers to the emission or absorption of heat by the current carrying conductor exposed to a temperature gradient. The heat generated by the Thomson effect is called Thomson heat. Thomson heat is proportional to the current and time can be expressed as: [31-33].

$$dQ = \chi I dt \frac{dT}{dx} \quad (2.9)$$

In which Q is Thomson heat, χ denoted the Thomson coefficient, I is the current intensity, t is time, and dT/dx is the temperature gradient along with the material. Thomson coefficient is different from two main thermoelectric coefficients because It can be determined by direct measurement on an individual material.

As mention before, three thermoelectric coefficients are related by the Kelvin equations:

$$\chi = T \frac{dS}{dT} \quad (2.10)$$

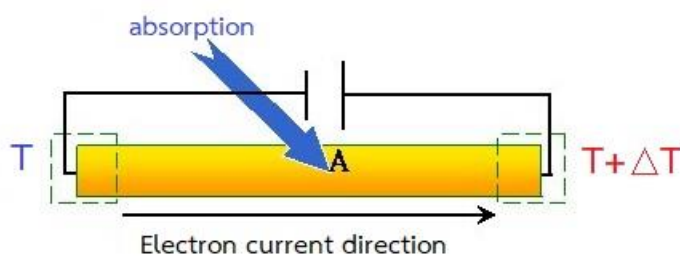


Figure 2.3 the absorption of heat by current carrying conductor exposed to a temperature gradient.

2.1.4 Figure of Merit

The efficiency of thermoelectric material can be determined by the figure of merit (ZT), defined as:

$$ZT = \frac{S^2 T}{\rho \kappa} \quad (2.11)$$

In which S is the Seebeck coefficient, T is temperature, ρ is electrical resistivity and κ is thermal conductivity. A good candidate thermoelectric material should have low ρ to minimize Joule heating, low κ to maintain a large temperature gradient, and a large Seebeck coefficient for maximum conversion of heat to electrical power or electrical power to cooling performance. The optimization ZT is not simply because the material properties are interrelated, so optimizing one can have a negative effect on the others. Especially, thermal conductivity and electrical resistivity are related to carrier concentrations as well as carrier mobility. A given temperature has a constant ratio based on the Wiedemann-Franz law

$$\frac{\kappa}{\sigma} = LT \quad (2.12)$$

$$L = \frac{\pi^2}{3} \left(\frac{\kappa_B}{e} \right)^2 = 2.45 \times 10^{-8} \left(\frac{W\Omega}{K^2} \right) \quad (2.13)$$

Where κ_B is the Boltzmann constant and e is the electron charge. The semiconductor materials have a high power factor (S^2/ρ) and a low thermal conductivity, which makes a high ZT materials. However, the Seebeck coefficient and electrical resistivity of semiconductor are related to the separation between the conduction band in N-type (valence band in P-type) and the Fermi level of the material. It is indicated that the increasing of the Seebeck coefficient by manipulating the Fermi level also increases the electrical resistivity as well. In order to reduce thermal conductivity, the common approach is to introduce additional short-range disorder into the crystalline structure. On the other hand, the distortion inevitably block transport, which may reduce the electrical conductivity.

2.1.5 Seebeck Coefficient

The Seebeck coefficient (S) of thermoelectric material is a measure of the induced thermoelectric voltage produced by a temperature difference across the material. A good thermoelectric should have an absolute value of S in the range of hundreds of $\mu\text{V}/\text{K}$, which is given by:

$$S(T) = \frac{8\pi^2 \kappa_B^2}{3eh^2} m^* T \left(\frac{\pi}{3n} \right)^{2/3} \quad (2.14)$$

$$S(T) \propto \frac{m^*}{n^{2/3}} \quad (2.15)$$

Where, h is the Plank's constant, m^* is the effective mass and n is the carrier concentration. Based on the equation, the Seebeck coefficient is negative if carriers are the electron, positive if carriers are holes. A maximum Seebeck coefficient can be achieved for large effective mass and low carrier concentration. On the other hand, a high Seebeck coefficient can result in low electrical conductivity. Generally, a high Seebeck coefficient is always found in semiconductors (N-type and P-type). This relation can be described based on the band model :

$$S(T) = \pm \frac{\kappa_B}{e} \left[\left(\frac{5}{2} + s \right) + \ln \frac{2(2\pi m^* \kappa_B T)^{3/2}}{h^3 n} \right] \quad (2.16)$$

In which s is the scattering parameter, assuming that the carrier relaxation time can be expressed in terms of carrier energy ($\tau = \tau_0 E^s$), where τ is the carrier relaxation time, τ_0 is a constant and E is the carrier energy. It can be expressed as:

$$S(T) = \pm \frac{\kappa_B}{\sigma} n\mu \left[\left(\frac{5}{2} + s \right) + \ln \frac{2(2\pi m^* \kappa_B T)^{3/2}}{h^3 n} \right] \quad (2.17)$$

As a result, the Seebeck coefficient, carrier concentration electrical conductivity and carrier mobility are interrelated in a semiconductor.

2.1.6 Electrical resistivity and Electrical conductivity

Electrical resistivity (ρ) is a measure of the ability of thermoelectric material to conduct the transport of an electrical current which can influence the value of ZT . Electrical conductivity (σ) is a measure of the ability of thermoelectric material to carry the transport of the charge carriers (electrons or holes). The charge carrier transport occurs due to the thermal energy and the associated random motion of carriers. In semiconductors, the carrier concentration depends strongly on the temperature. At zero temperature, the conductivity is zero. Also, the scattering processes and thus the relaxation time constant exhibit a temperature dependence. The conductivity of semiconductors spans a wide range from insulating to almost metallic conduction.

The electrical conductivity is inversely proportional to the electrical resistivity. SI unit of time the electrical resistivity is $\Omega.m$ while the electrical conductivity is per $\Omega.m$ or (S/m) . The electrical conductivity and mobility can be related to relaxation time as equations

$$\sigma = \frac{1}{\rho} = \frac{ne^2\tau}{m^*} \quad (2.18)$$

In an intrinsic semiconductor, the carrier mobility (μ) is determined by scattering with phonons. Further scattering is introduced by impurities, defects or alloy disorder. The electrical conductivity is proportional to the carrier concentration (n), the electron charge (e) and the carrier mobility (μ), which is given by:

$$\sigma = en\mu \quad (2.19)$$

For each carrier type, the mobility in the relaxation time approximation is given by:

$$\mu = \frac{e\tau}{m^*} \quad (2.20)$$

In the presence of both electrons and holes,

$$\sigma = \sigma_e + \sigma_h = -en\mu_e + en\mu_h \quad (2.21)$$

Where τ is the charge carrier relaxation time which depends on the charge carrier scattering, μ_e and μ_h is the mobility for electrons and holes, respectively. These are given by $\mu_e = -e\tau/m^*$ and $\mu_h = +e\tau/m^*$. As the unit for mobility, usually cm^2/Vs is used. In small bandgap semiconductors, high mobility is caused by its small effective mass [32]. The majority carriers greatly outnumber minority carriers, so that Equation (2.21) can be reduced to a single term involving the majority carrier. [33]

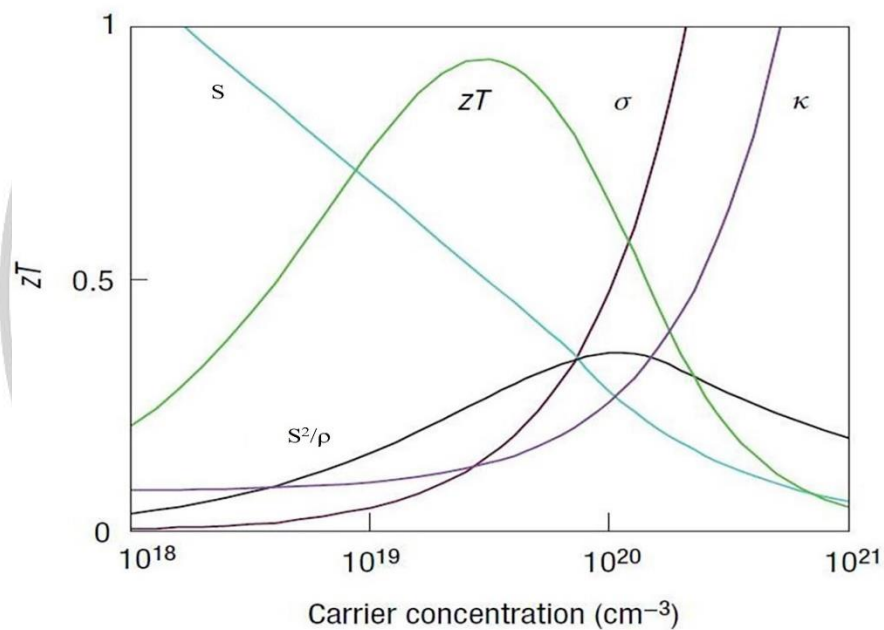


Figure 2.4 Carrier concentration on thermoelectric properties of a material [3].

According to equation (2.11), a high ZT requires a high Seebeck coefficient, a high electrical conductivity and a high thermal conductivity depends on the carrier concentration. However, the Seebeck coefficient decreases with increasing carrier concentration. Both electrical conductivity and electronic thermal conductivity increase with increasing the carrier concentration, as shown in Figure. 2.4. since there are more carriers to transport electron charges and heat energy, through the Wiedemann–Franz relation. The maximum ZT has occurred with a carrier concentration of $n \approx 10^{19} \text{ cm}^{-3}$.

2.1.7 Carrier mobility

According to equation (2.19), the electrical conductivity is proportional to the carrier concentration and carrier mobility. In a semiconductor, the carrier concentration and carrier mobility are temperature dependent. The role of scatters and the effect on mobility can be considered by considering the two main types of scattering mechanisms, lattice scattering and impurity scattering. The mobility due to these scattering mechanisms is illustrated.

1. Lattice scattering

Lattice scattering is a thermal motion of lattice atoms at above-zero temperatures. The carrier scattering is mainly due to the thermal vibration of the lattice at high temperatures. The acoustic waves can be generated in terms of phonons. In metals, carrier-carrier scattering affects the electrical conductivity, but the carrier concentration in semiconductors are low. As a result, carrier-carrier scattering can be ignored in a semiconductor. For lattice scattering, the scattering time (τ) in terms of a scattering cross-section (S) is given by:

$$\tau = \frac{1}{Sv_{th}N_s} \quad (2.22)$$

Where v_{th} is the mean speed of the carriers (thermal velocity) and N_s is the number of scatters per unit volume. If a is the amplitude of lattice vibration of two-dimension scattering, $S = \pi a^2$. The a increases with increasing temperature and hence

the S increases. In terms of v_{th} , an electron in the conduction band is equal to its kinetic energy so that

$$\frac{1}{2} m_e^* v_{th}^2 = \frac{3}{2} k_B T \quad (2.23)$$

$$v_{th} \propto \sqrt{T} \quad (2.24)$$

The N_s is a constant and is independent of temperature. As a result, the lattice scattering time (τ_L) on temperature is given by:

$$\tau_L = \frac{1}{(\pi a^2) v_{th} N_s} \propto \frac{1}{T} \left(\frac{1}{T^2} \right) \propto T^{-\frac{3}{2}} \quad (2.25)$$

Since the scattering time is directly proportional to the mobility. This means that μ due to lattice scattering varies as $T^{-\frac{3}{2}}$. As increasing in temperature, the lattice scattering is influenced to reduce carrier mobility. This means, as the temperature increase, the atomic vibrations increases the electrons moves faster leading to reduce the carrier mobility. A similar argument is valid for *P*-type semiconductors (hole). Despite the decrease of carrier mobility, the electrical conductivity increases with temperature due to the exponential increase in carrier concentration.

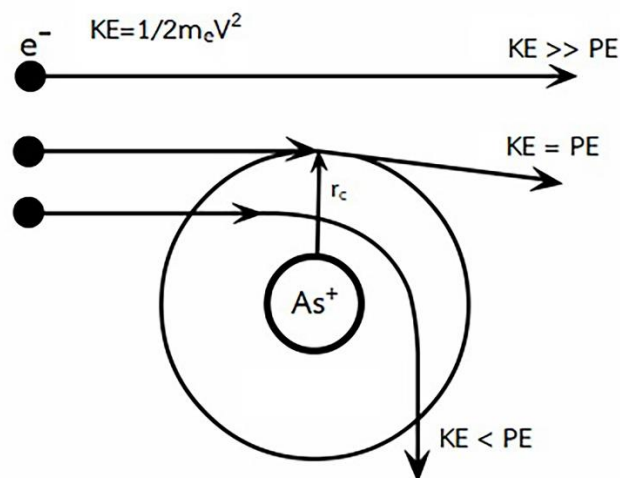


Figure 2.5 Carrier scattering from an ionized As donor.

2. Impurity scattering

Impurity scattering is based on the ionized donor and acceptor impurities. At room temperature the impurities are ionized, there is an electrostatic attraction between the carriers traveling in the lattice and the impurities. The probability of impurities scattering independent of the doping density and the ionized impurities. As seen in Figure. 2.5, as a donor, the scattering cross-section is calculated from the balance between the KE and the PE of the carrier due to the ionized impurities. The carrier will be scattered if PE dominated. The scattering radius (r_c) is the distance at which both effects are equal.

$$\frac{3}{2} k_B T = \frac{e^2}{4\pi\epsilon_0\epsilon_r r_c} \quad (2.26)$$

$$S = \pi r_c^2 \propto T^{-2} \quad (2.27)$$

The scattering time due to impurities (τ_I) is given by:

$$\tau_I = \frac{1}{(\pi r_c^2) \nu_{th} N_I} \propto \frac{1}{(T^{-2}) \left(T^{\frac{1}{2}} \right)} \propto T^{\frac{3}{2}} \quad (2.28)$$

Since the scattering time is directly related to mobility, the mobility due to impurities increases with temperature. It opposites to the lattice scattering behavior. At low temperatures, the carriers can travel slower and this makes it easier to ionized impurities. Also with increasing temperature, the charge carriers are moving faster and this makes the interaction with the impurity for a shorter time. The carrier mobility due to impurity scattering decreases as $T^{\frac{3}{2}}$.

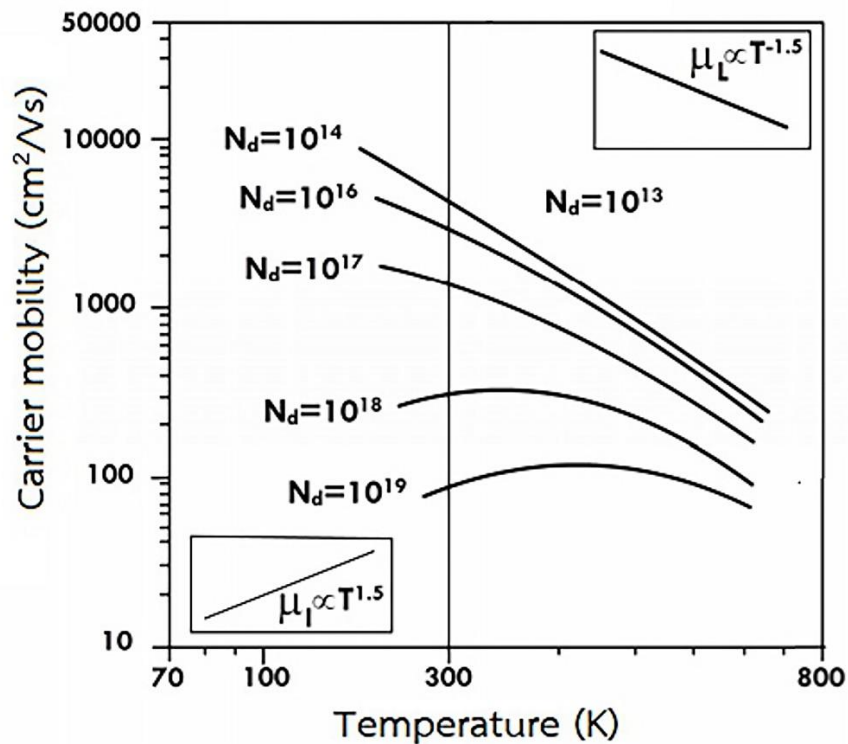


Figure 2.6 Temperature dependence on carrier mobility due to lattice and impurity scattering with a various donor concentration of semiconductor [4].

At low temperature, the carrier mobility increases due to impurity scattering dominated, while at high-temperature lattice scattering dominated, as seen in Figure 2.6. At low donor concentrations, lattice scattering dominates over the entire temperature range. As increasing donor concentrations impurity scattering starts to dominate at low temperatures. In acceptor concentration is also the same behavior, the carrier mobility decreases with increasing carrier concentration. The temperature dependence of conductivity is seen in Figure 2.7. The dominating term is still the carrier concentration, due to its exponential dependence on temperature but the mobility term also plays a role, especially in the extrinsic region (or saturation region in n). The optimal temperature range σ is nearly the saturation region n .

The carrier concentration in a semiconductor is affected by temperature, as seen:

$$\sigma \propto \exp\left(-\frac{E}{k_B T}\right) \quad (2.29)$$

Where, E is the conduction energy. At low temperatures, the carrier is small while at the high-temperature donor or acceptor atoms are increasingly ionized.

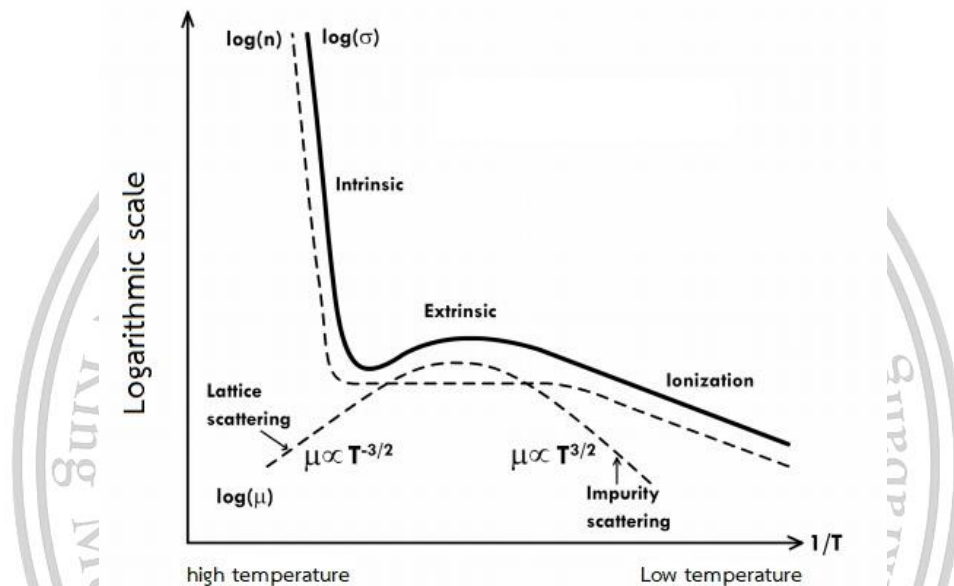


Figure 2.7 Temperature dependence on electrical conductivity, carrier concentration and carrier mobility [4].

During the ionized, carrier concentrations become saturated. At this time a further temperature increase generated the intrinsic carriers by thermal. In the intrinsic region, carrier concentration increases with increasing temperature. In this case, the influence of lattice scattering, $\mu \propto T^{-3/2}$, can be expected. At high-temperature measurement, E is the energy gap (E_g) and at low-temperature measurement, E is the activation energy (E_a).

2.1.8 Thermal conductivity

Thermal conductivity (κ) is the ability of thermoelectric material to describe the heat transfer under the effect of a temperature gradient across a different point. Thermal conductivity is measure in units of W/mK . According to Equation (2.11), low thermal conductivity is required. It is an important factor to be controlled when optimizing for a high ZT .

The total thermal conductivity in semiconductors is classified into two main components, electronic thermal conductivity (κ_e) and lattice thermal conductivity (κ_l) based on the contribution of charge carriers transporting heat and lattice waves (phonons), respectively. The thermal conductivity of semiconductors is temperature-dependent. Total thermal conductivity is given by:

$$\kappa = \kappa_e + \kappa_l \quad (2.30)$$

1. Electrical thermal conductivity

The electrical thermal conductivity is mainly related to carriers transporting heat. The ratio of the electronic transporting heat to the electrical conductivity of a metal is directly proportional to the temperature through the Wiedemann-Franz law, in Equation (2.12). In theoretical, the value $L = 2.45 \times 10^{-8} \text{ (W}\Omega/\text{K}^2)$ is defined that the electrons do not interact with each other. The electron can be scattered with impurities or lattice vibrations. The Wiedemann and Franz law is valid at low temperatures. At high temperature ($T \geq \theta_D$), the carriers are elastically scattered, which θ_D is Debye temperature ($\theta_D = 160\text{K}$ for Sb_2Te_3).

The κ_e is sensitive to carrier concentration and mobility. If the concentration increases, the electrical conductivity increases leading to the electron thermal conductivity increases linearly. However, the carrier mobility has less influence on electrical thermal conductivity due to a small proportion of total thermal conductivity generated by electrical thermal conductivity, the impact of κ_e can be neglected at low temperatures [4, 26].

2. Lattice thermal conductivity

The lattice thermal conductivity is mainly related to the crystal structure, grain boundary, lattice defects, imperfections, dislocations, anharmonicity of the lattice oscillations, carrier concentration, and interactions between the carriers and lattice waves. Lattice thermal conductivity based on classical kinetic energy theory of gases is defined as follows:

$$\kappa_l = \frac{1}{3} C_v \bar{d} \bar{v} \quad (2.31)$$

In which, C_v is the specific heat at constant volume, \bar{d} is the average phonon mean free path and \bar{v} is the average phonon velocity. At above Debye temperature, C_v approaches the classical value of $3R$, where R is a gas constant. At low temperature, C_v is proportional to T^3 , following the law of Debye ($C_v \propto T^3$).

Since Equation. (2.31) is not valid for a wide range of materials. Then, the lattice thermal conductivity, using the Callaway formalism, as seen:

$$\kappa_l = \frac{k_B}{2\pi^2 v_s} \left(\frac{k_B T}{\hbar} \right)^3 \int_0^{\frac{\theta_D}{T}} \tau_c(x) \frac{x^4 e^x}{(e^x - 1)} dx \quad (2.32)$$

In which, \hbar is the reduced Plank's constant ($\hbar = \frac{h}{2\pi}$), x is the dimensionless parameter with $x = \frac{\hbar\omega}{2\pi k_B T}$, ω is the frequency of phonon and v_s is the speed of sound and τ_c is the combined phonon relaxation time. The relation between the phonon scattering mechanisms and the combined phonon relaxation time can be obtained according to Matthiessen's rule, can be written as

$$\tau_c^{-1} = \tau_p^{-1} + \tau_D^{-1} + \tau_B^{-1} + \tau_{EP}^{-1} \quad (2.33)$$

In which, τ_c^{-1} is the total probability of scattering, τ_p^{-1} is the probability for phonon-phonon scattering, τ_D^{-1} is the probability for point defect scattering, τ_B^{-1} is the probability for grain boundary scattering and τ_{EP}^{-1} is the probability for electron-phonon scattering. The total phonon scattering mechanisms are described [34,36].

1. Phonon-phonon scattering

The phonon-phonon scattering has occurred at a high temperature ($T \gg \theta_D$) because there is more phonon. The scattering is given by:

$$\tau_p^{-1} = B\omega^2 T \exp\left(-\frac{\theta_D}{3T}\right) \quad (2.34)$$

The effect of phonon-phonon scattering to temperature dependence on thermal conductivity is expressed by

$$\kappa \propto \exp\left(\frac{\theta_D}{2T} - 1\right) \quad (2.35)$$

At the above Debye temperature, the thermal conductivity is inversely proportional to temperature. As the temperature below, the thermal conductivity should be raised exponentially until other scattered predominate.

2. Point defect phonon scattering

The point defect such as vacancies, dislocations, uncharged impurity sites and different isotopes of the host constituents is an atom with different forms. There has little effect on the long-wavelength (low energy of phonon). But short wavelength, high energy phonons are strongly scattered by point defects. The Point defect phonon scattering is given by:

$$\tau_D^{-1} = A\omega^4 \quad (2.36)$$

3. Grain boundary phonon scattering

The grain phonon boundary scattering is mainly significant to the crystalline size at low temperatures and thus should not be important limitations at high temperatures. The Boundary scattering can be written in term of grain size (d) and film thickness (t) as:

$$\tau_B^{-1} = \frac{v_s}{d} + \frac{v_s}{t} \quad (2.37)$$

4. Carrier-phonon scattering

The charge carrier-phonon scattering is much more effective at low temperatures. The long-wavelength of phonon can interact with all charge carriers. Carrier phonon scattering can be increased when the carrier concentration of material increases. The carrier-phonon scattering is given by:

$$\tau_{EP}^{-1} = C\omega \quad (2.38)$$

Therefore, good thermoelectric materials are crystalline materials that manage to scatter phonon without significantly disrupting the electrical conductivity.

2.2 Thermoelectric Applications

Thermoelectric technology is widely used due to increasing renewable energy and improving energy efficiency. It was stated that thermoelectric devices directly convert heat into a temperature difference and heat flow and vice versa which is made up of three different effects: the Seebeck effect, the Peltier effect and the Thomson effect. A recent development in theoretical studies on the thermoelectric provides new opportunities for wide applications such as equipment used by the military, medical, industrial, and scientific.

Generally, thermoelectric devices contain more than one thermoelectric couples consist of N -type and P -type semiconductors, which are different charge carriers. The voltage for the Seebeck effect and the cooling and heating power for the Peltier effect is

increased directly proportional to the number of couples. The Seebeck and Peltier effects occur due to the charge carrier movement in the thermoelectric materials. In *N*-type semiconductor, the major carriers are electrons. In *P*-type semiconductor, the major carriers are holes. Holes are vacancies in a crystal structure in which an electron could occupy. In the Seebeck effect, the charge carriers can be diffuse from the hot to cold. The buildup of charge at the cold produces a voltage potential. The electrical voltage will drive the electrical current in a completed circuit and produce electrical power. In the Peltier effect, rather than having a resistive load in the circuit, the direct current source is used to move the carriers by an electric field. When the charge carriers transport, the heat was taken with them. The electrons moving to the higher energy absorb heat and electrons that move to a lower energy release heat. This charge carrier movement can be used to pump heat against the direction it naturally flows and produce cooling and heating.

Thermoelectric devices are usually called a thermoelectric module. It consists of thermoelectric couples. The thermoelectric couples are wired electrically in series and thermally in parallel and connected on the top by an electrode. The couples are sandwiched between a substrate that is sometimes ceramic. This provides structural rigidity, a flat surface for good thermal contact and electrical insulation for the electrical interconnects between the *P*-type and *N*-type semiconductors, as seen in the Figure. 2.8.

Thermoelectric devices will provide advantages over alternative technologies. the significant features of thermoelectric modules include: there are no moving parts lead to increased reliability and long life. There are much smaller and lighter than a comparable mechanical system, depending on the application requirement. The systems are silent operation and environmentally friendly. The fast response time of thermoelectric happens depending on the speed of electrons.

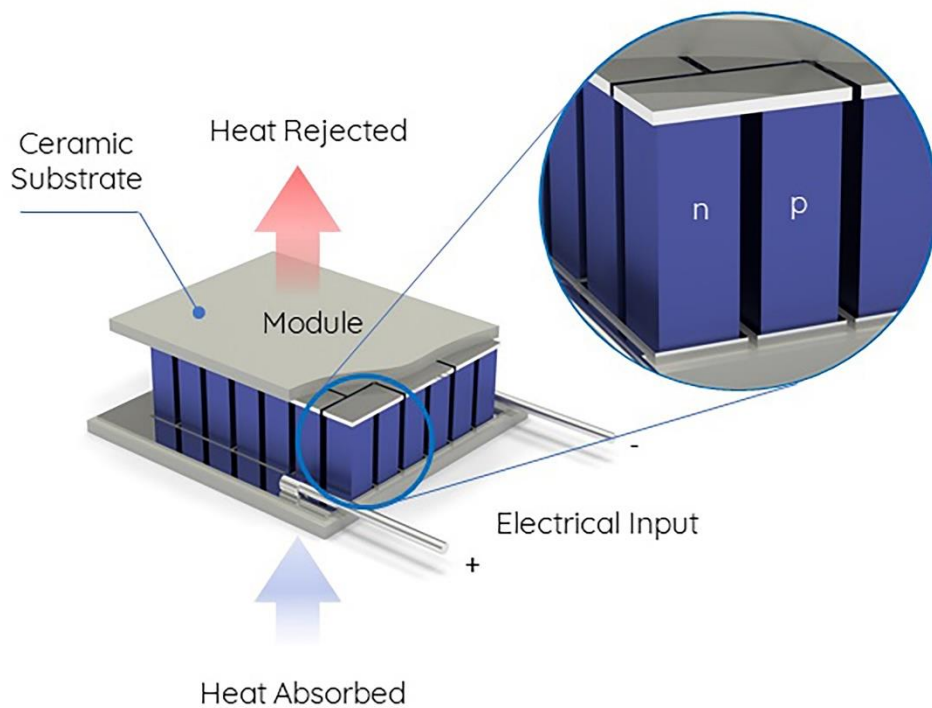


Figure. 2.8 Schematic of the thermoelectric module.

2.2.1 Thermoelectric power generator (TEG)

Thermoelectric generators directly convert heat into electrical power based on the Seebeck effect. Figure. 2.9 (a) is the mechanism of TEG. The thermoelectric couples are wired electrically in series and thermally in parallel. Heat is pumped into the hot side, transported through thermocouples and rejected to other sides. The charge carriers can be diffuse from the hot to cold. The buildup of charge at the cold produces a voltage potential. The electrical voltage will drive the electrical current in a completed circuit and produce electrical power. The output voltage is increased directly proportional to the number of couples (n)

The output voltage (V) can be generated as:

$$V = n(S_p - S_n)\Delta T \quad (2.39)$$

Where, $S_p - S_n$ is the Seebeck coefficients of TEG, ΔT is the temperature gradient between hot and cold junctions.

The output power (P) of the TEG can be calculated as:

$$P = I^2 R_L = \frac{V^2}{(R_p + R_n)^2} R_L \quad (2.40)$$

Where $R_p + R_n$ is the internal resistance of TEG and R_L is the external load. When $R_p + R_n$ equals R_L , the maximum power (P_{\max}) can be obtained:

$$P_{\max} = \frac{n^2 (S_p - S_n)^2 \Delta T^2}{4R} \quad (2.41)$$

The efficiency of TEG (η) is defined as the ratio of the generated power to the power drawn from a heat source (Q_H).

$$\eta = \frac{P}{Q_H} \quad (2.42)$$

If the R_L is chosen to maximize the maximum output, the maximum efficiency (η_{\max}), is given by:

$$\eta_{\max} = \frac{\Delta T}{T_h} \times \frac{\sqrt{1+ZT} - 1}{\sqrt{1+ZT} + \frac{T_c}{T_h}} \quad (2.43)$$

Equation (2.43) show that the power generation efficiency is depending on the ZT of materials, the temperatures of the hot and cold junctions and the external load resistance.

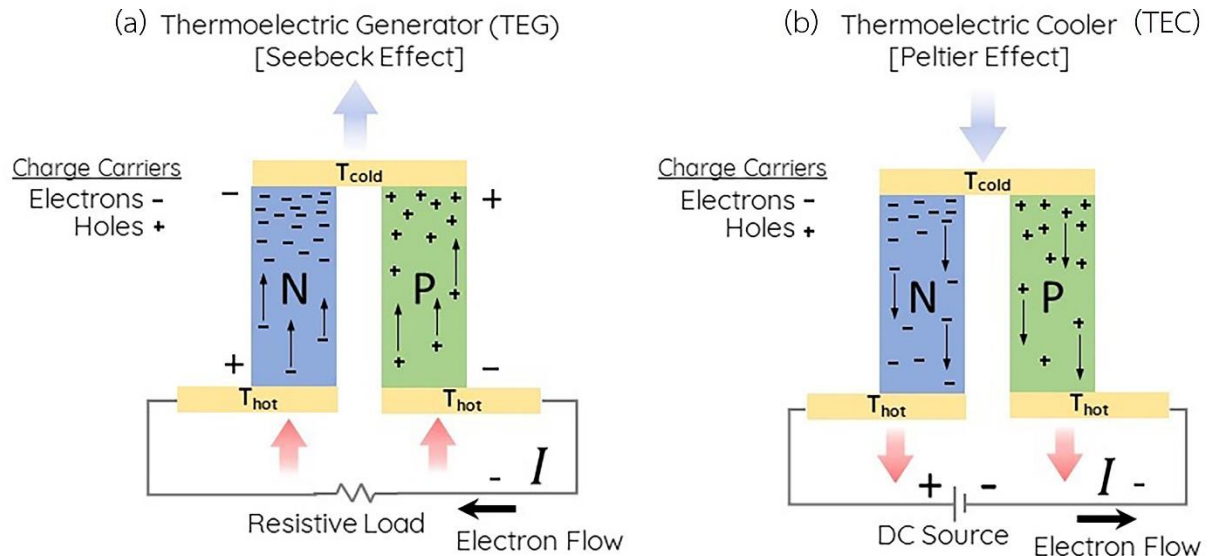


Figure 2.9 The schematics of (a) thermoelectric generator and (b) thermoelectric cooling.

2.2.2 Thermoelectric cooling (TEC)

Thermoelectric cooling or thermoelectric refrigeration directly converts an electrical current to heat based on the Peltier effect to create a heat flux between the junctions of two different types of materials, as seen in the figure. 2.9 (b). This effect is typically used in portable coolers and cooling in electronic circuits. The direct current source is used to move the carriers by an electric field. When the charge carriers transport, the heat was taken with the carriers. The electrons moving to the higher energy absorb heat and electrons that move to a lower energy release heat. This charge carrier movement can be used to pump heat against the direction it naturally flows and produce cooling and heating.

The coefficient of performance ($COP: \phi$) for a TEC is defined as the ratio of the cooling capacity Q_c to the total power consumption (P).

$$\phi = \frac{Q_c}{P} \quad (2.44)$$

The maximum COP is given by:

$$\phi_{\max} = \frac{T_h}{\Delta T} \times \frac{\sqrt{1+ZT} - \frac{T_c}{T_h}}{\sqrt{1+ZT} + 1} \quad (2.45)$$

Equation (2.45) shows that the maximum coefficient of performance of TEC is depending on the ZT of materials, the temperatures of the hot and cold junctions.

2.3 Antimony telluride thermoelectric material

Antimony telluride (Sb_2Te_3) is a promising P -type thermoelectric material from V-VI group. The atomic arrangement is based on general formula $A_2^V B_3^{VI}$ ($A = Sb$ and $B = Te$) with a narrow band gap ($E_g < 0.2$ eV). Sb_2Te_3 compounds have the rhombohedral crystal structure with five atoms per unit cell belonging to the space group $R\bar{3}m$. The Sb and Te atoms consist of the sequence of layers, each layer comprising five atomic planes oriented perpendicular to the c -axis according to the scheme: ... $Te^{(1)}$ - Sb - $Te^{(2)}$ - Sb - $Te^{(1)}$... $Te^{(1)}$ - Sb - $Te^{(2)}$ - Sb - $Te^{(1)}$..., as seen in Figure. 2.10.

Such a sequence is repeated in parallel layers and single sequence known as quintuple. The subscript of Te refer to various types of bonding with antimony. The $Te^{(1)}$ - Sb and Sb - $Te^{(2)}$ was bonded by covalent-ionic bond and there are the van der Waals gap between $Te^{(1)}$ and $Te^{(1)}$ atoms.

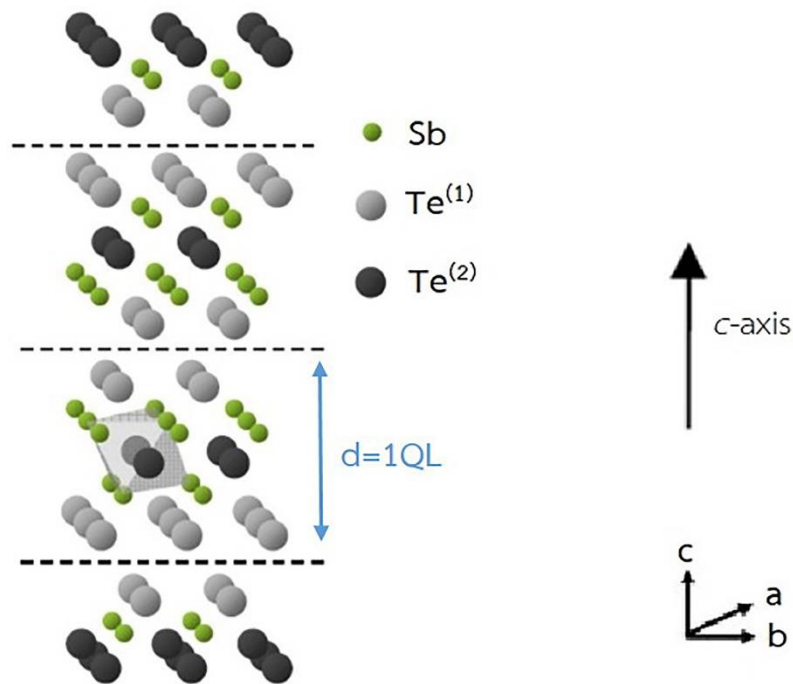


Figure 2.10 Atomic layers of Sb_2Te_3 crystal structure. Dash line indicates van der Waals gap of one quintuple layer (QL).

Because of weak van der Waals bonding, this compound has a layer structure, the crystal can easily cleavage along the c -direction. Typically, the Sb_2Te_3 compound is excellent thermoelectric properties due to the large mean molecular mass, low melting temperature and partial degeneracy of the conduction and valence bands of V-VI chalcogenide [37]. The non-cubic structure of Sb_2Te_3 contributed to anisotropic in thermoelectric properties, the electrical and thermal conductivities are higher along a plane parallel to the cleavage than perpendicular to them.

Recently, tuning the carrier conduction or lowering the phonon conductivity through a reduction in the dimension of the structure have been studied to enhance thermoelectric efficiency. In nanostructured materials, grain boundary scattering plays an important role to suppress the lattice thermal conductivity with phonon, while the electronic thermal conductivity can be controlled efficiently by carrier concentration [26].

Typically, the excellence ZT of Sb_2Te_3 is achieved approximately near room temperature (300 K), which corresponding to human body heat source [24-28].

2.4 Bismuth Telluride thermoelectric material

Bismuth telluride is one of the most interesting thermoelectric materials with a high ZT and it is known to have an excellent thermoelectric performance at room temperature [2]. Z. Zeng et al reported bismuth telluride bulk alloys have a high ZT about 1.14 at room temperature [14]. The ZT value can be made to increase when improvements are made to low-dimensional thermoelectric materials [3]. Bismuth telluride is a narrow gap layered semiconductor with band gap of 0.15 eV.

Bismuth telluride has a severalty of different crystals structures depend on a stoichiometric composition of materials. Bismuth telluride has general formula $(\text{Bi}_{1-x})_2\text{Te}_3$. The crystal structure of the most common is BiTe phase and Bi_2Te_3 phase [15] as shown in Figure 2.4. Bismuth telluride (Bi_2Te_3) thin films normally require a stoichiometric ratio of $[\text{Bi}]$ and $[\text{Te}]$ for achieving the best thermoelectric performance [3].

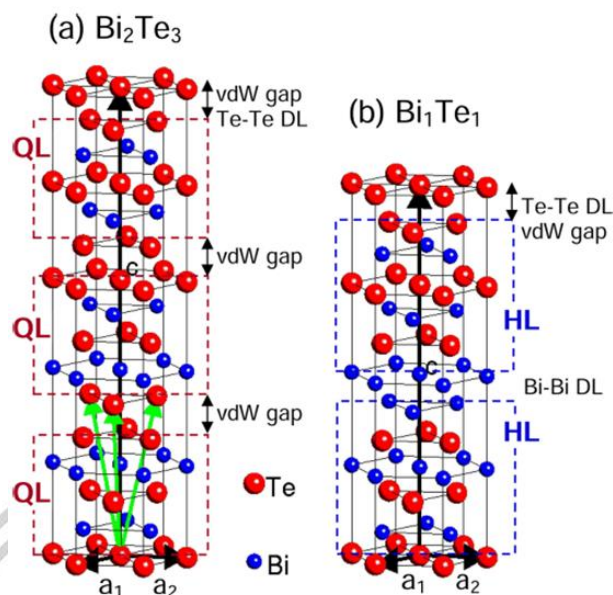


Figure 2.11 Hexagonal unit cell of (a) Bi_2Te_3 and (b) BiTe with the base vectors indicated by the black arrows [15].

Bismuth telluride has been crystallized in a tetradymite-type structure. For Bi_2Te_3 , the stacking sequence of lattice planes results in the formation of three groups consisting of 5 atom layers (quintuple layer, QL) with the sequence $\text{Te}^1\text{-Bi-Te}^2\text{-Bi-Te}^1$ stacking along the c -axis. [15,16,17]. The bonding inside the quintuple layer is described as mixed ionic-covalent bonds ($\text{Te}^1\text{-Bi}$ and Bi-Te^2), while Te-Te bonds between quintuple layers are of only weak van der Waals bonding as shown in Figure 2.6 (a) [15,16]. The unit cell of Bi_2Te_3 is rhombohedral in space group $R\bar{3}m$, which the lattice parameters of Bi_2Te_3 in terms of the hexagonal axes are $a_H = 4.383 \text{ \AA}$, $c_H = 30.487 \text{ \AA}$ [15].

For BiTe , the stacking sequence of lattice planes results in the formation of two groups consisting of 6 atom layers (hextuple layer, HL) with the sequence $\text{Te}^1\text{-Bi}^1\text{-Te}^2\text{-Bi}^2\text{-Te}^3\text{-Bi}^3\text{-Bi}^3\text{-Te}^3\text{-Bi}^2\text{-Te}^2\text{-Bi}^1\text{-Te}^1$ stacking along the c -axis. [15,16,17]. The bonding inside the hextuple layer is described as mixed ionic-covalent bonds, while Te-Te bonds between hextuple layers are of only weak van der Waals bonding as shown in Figure 2.6 (b) [15,16]. The unit cell of BiTe is rhombohedral in space group $R\bar{3}m$, which

the lattice parameters of BiTe in terms of the hexagonal axes are $a_H = 4.402 \text{ \AA}$, $c_H = 24.202 \text{ \AA}$ [15].

2.5 The film deposition process

The film depositions using vacuum technologies are typically classified into two main categories: depending on whether the process is primarily chemical and physical processes. Several processes exhibit unique material properties resulting in the growth process and deposition parameters. The film deposition using vacuum processes contains three main steps:

1. Creation of the appropriate atomic, molecular or ionic depositing species
2. Transport of the species from the source to the substrate
3. Condensation of the depositing species on the substrate directly or via a chemical reaction with reactive constituents, forming a solid deposit.

In atomic processes, the solid film is formed by condensation of the atoms in the vapor phase onto the substrate and migration to nucleation and growth sites. The adsorbed atoms require enough energy to occupy their lowest energy configurations avoiding structural imperfections. The microstructure and morphology of the deposited film are a result of the energy of the atoms which is dependent on the deposition process deposition parameters [29].

Table 2.1 Several techniques of the film deposition

Chemical vapor deposition (CVD) techniques	Physical vapor deposition (PVD) techniques
<ul style="list-style-type: none"> ● Plasma-enhanced CVD (PECVD) ● Atmospheric pressure CVD ● Low-pressure CVD (LPCVD) ● Very low-pressure CVD (VLPCVD) 	<ul style="list-style-type: none"> ● Thermal evaporation ● Sputtering ● Molecule beam epitaxy

2.5.1 Chemical Vapor Deposition (CVD)

In chemical vapor deposition, the films are deposited via a chemical reaction between heat substrate and inert gas in the chamber at low pressure. The precursor is introduced into a reaction chamber and is controlled by balanced flow regulators and control valves. The precursor molecules pass by the substrate, are drawn into the boundary layer, and are deposited on the surface of the substrate.

2.5.2 Physical Vapor Deposition (PVD)

In physical vapor deposition, the precursors (solid, liquid or, vapor) are released and moved to the surface of the substrate. The physical vapor deposition consists of different methods such as thermal evaporation, molecular beam epitaxy, and sputtering.

- Evaporation: Material is heated to a gas phase, where it then diffuses through a vacuum to the substrate.
- Molecular beam epitaxy: The substrate is cleaned and loaded into a chamber that is evacuated and heated to remove the surface contaminants and to roughen the surface of the substrate. The molecular beams emit a small amount of material through a shutter, which then collects on the substrate.
- Sputtering: Plasma is generated; this plasma contains argon ions and electrons. The atoms from the target are ejected after being struck by argon ions. Atoms from the target travel through the plasma and form a layer on the substrate [30].

2.5.3 Advantages and Disadvantages of film deposition

Depending on the applications, there are sound arguments for the use of either process (PVD or CVD). One reason to use a physical vapor deposition process (such as sputtering) instead of chemical vapor deposition is the temperature requirement.

CVD processes run at a much higher temperature than PVD processes. A furnace, RF coil, or laser always generates substrate temperature. Substrates that cannot tolerate this temperature must have films deposited by the physical form of vapor deposition instead. The benefit of the substrate temperature in some CVD processes is that there is

less waste deposition, especially in cold-wall reactors, because only the heated surfaces are coated. With the use of a laser heating system, the CVD process becomes selective to the path of the laser; this is a distinct advantage over PVD methods.

The molecular beam epitaxy (PVD process) has a distinct advantage of atomic-level control of the chemical composition, the film thickness, and the transition sharpness. This process is relatively more expensive but is worth the added cost for applications that demand higher precision.

Sputtering (PVD process) does not require the use of a specialized precursor as used in CVD. Sputtering has a wide range of materials readily available for deposition. Another advantage of PVD over CVD is the safety issue of the materials that are used for CVD.

However, the researcher could easily select CVD or PVD for research based on criteria such as the cost, the film thickness, the precursor availability, and the compositional control. In this work, sputtering was selected due to a wide range of materials. Further, the sputtering process is environmentally friendly and safe compared to other processes. Among these deposition techniques, sputtering has been widely used because it produces high-quality films, extremely high adhesion and excellent uniformity over a large substrate area.

2.6 Sputtering process

The sputtering process is a widely used technique for deposition of the films, defined as the removal of surface atoms of the target by energetic ion bombardment. Momentum transfer theory and Thermal vaporization theory have been proposed for sputtering. Sputter atoms are emitted when kinetic moments of incident ions are transferred to the target surface. The surface of the target is heated to be vaporized due to the bombardment of energetic ions.

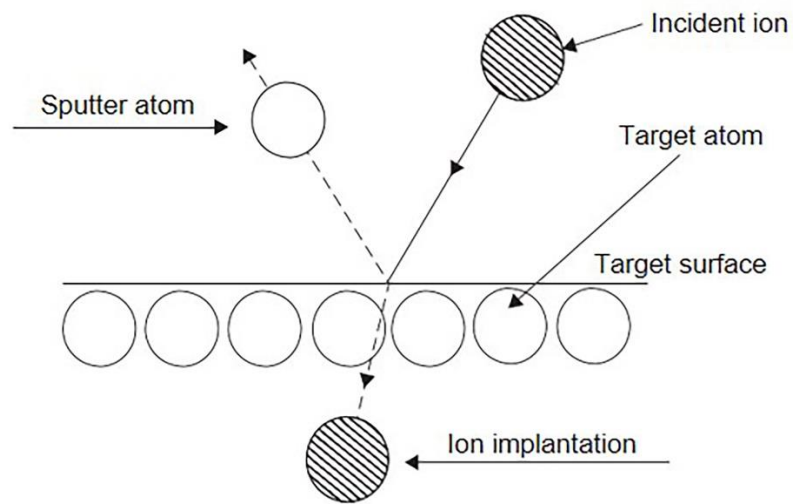


Figure 2.12 Physical sputtering process

Direct current (DC) sputtering system is composed a pair of planar electrodes. One is a cathode and another one is an anode. The top of plasma facing surface is covered with a sputtering target and the reverse side is water-cooled. The substrate is placed on the anode. The sputtering chamber is set to vacuum and filled with inert gas, mostly Argon. The glow discharge is generated under the applied of DC voltage between two electrodes. The Ar^+ ions generated in the glow discharge are accelerated at the cathode fall and sputter the target resulting in the deposition of the film on the substrate at the anode. The target is always conduction material because the glow discharge (current flow) is maintained between metallic electrodes. The advantage of the DC system is simply set up. It is the standard sputter device. The deposition rates are almost constant in various material. The film thickness can be controlled with proportional with current. The deposition rates of the DC is higher than the RF mode. And adhesion strength is high because of high energy process. However, the main disadvantage of the DC system is required high Ar pressure. Sputtering target is restricted to metal. Non-conductive materials cannot be deposited by DC system since the non-conductive coating on the substrate prevents the electron flow through the anode.

Sputtered atoms collide with Ar gas and diffuse to the substrate since the gas pressure is high and the mean free path of the sputtered atoms is less than the electrode spacing. The amount of sputtered atoms deposited on a unit substrate area (W) is determined by deposition rates (R).

$$W = \frac{k_1 W_0}{pl} \quad (2.46)$$

$$R = \frac{W}{t} \quad (2.47)$$

Where, k_1 is a constant, W_0 is the amount of sputtered atoms from the unit cathode area, P is the discharge gas pressure, l is the electrode spacing and t is the sputtering time.

The amount of sputtered particles from the unit cathode area W_0 is given by:

$$W_0 = \left(\frac{j_+}{e} \right) St \left(\frac{A}{N} \right) \quad (2.48)$$

The j_+ is nearly equal to the discharge current I_s , and the sputter yield is proportional to the discharge voltage V_s , the total amount of sputtered particles becomes $V_s I_s t / pl$. Thus, the sputtered deposit is proportional to discharge voltage, discharge current and sputtering time ($V_s I_s t$).

The deposition rates of the sputtering are lower than other vacuum deposition. In general, lower sputtering pressure increases deposition rates. Low-pressure sputtering is a promising process for film production but fewer ions to bombard for deposition, which reduced the deposition rate process. Magnetron sputtering system is used to improve the ions bombarding by installing of the magnet in the rear of the sputtering target. The magnetic flux on the cathode surface is terminated to the magnetic core. A magnetic field is assumed on the cathode which parallels to the surface of the target. The electron in the glow discharge shows cycloid motion and the center of orbit drifts in a direction of $\mathbf{E} \times \mathbf{B}$ with the drift velocity of $\frac{\mathbf{E}}{B}$, where \mathbf{E} and \mathbf{B} denotes the electric field and the magnetic field, respectively. The magnetic field lines trap the escaping energetic electrons, and the trapped electrons make ionizing collisions.

The increasing of the ionization increases the ion current to the cathode target and lowers the operating gas pressure resulting in higher deposition rates. The incident flux of ionized particles increases in the magnetron increasing deposition rates. The incident ionized flux modifies the growth process. Moreover, high ion current density will enhance the chemical reaction at the substrate during the film growth.

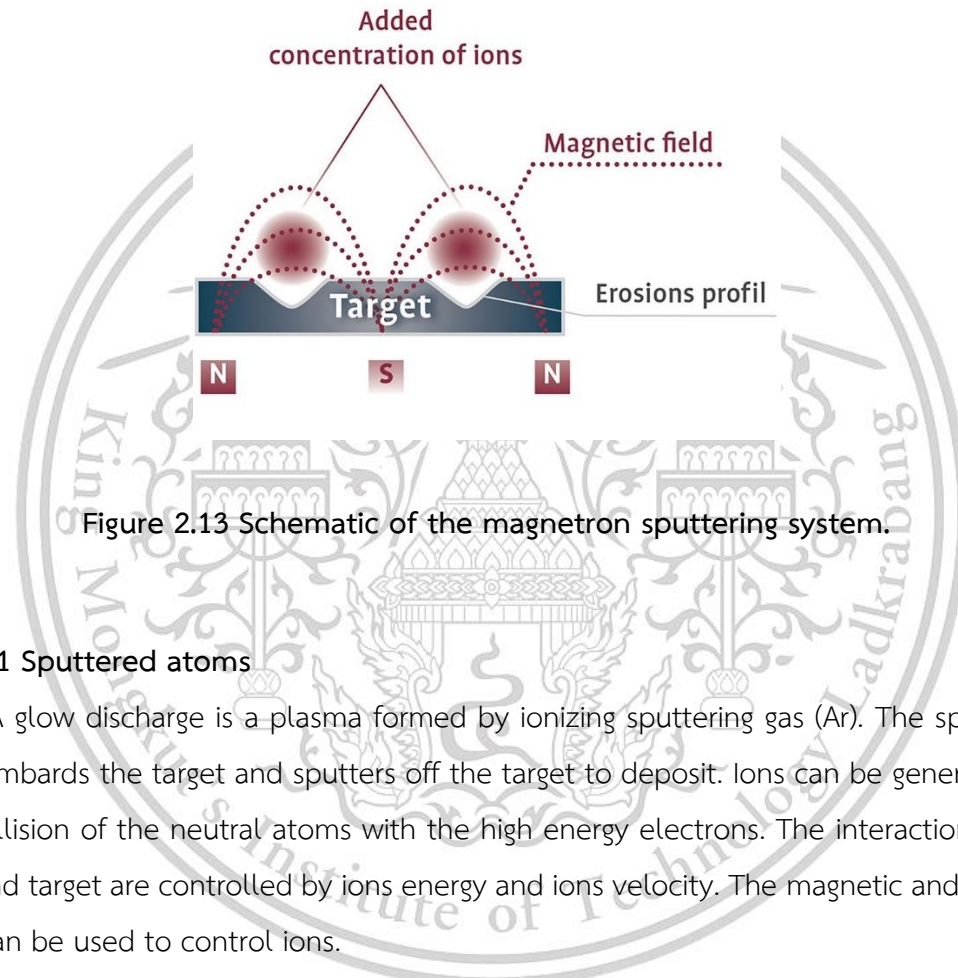


Figure 2.13 Schematic of the magnetron sputtering system.

2.6.1 Sputtered atoms

A glow discharge is a plasma formed by ionizing sputtering gas (Ar). The sputtering gas bombards the target and sputters off the target to deposit. Ions can be generated by the collision of the neutral atoms with the high energy electrons. The interaction of the ions and target are controlled by ions energy and ions velocity. The magnetic and electric field can be used to control ions.

The process begins with applying voltage between two electrodes. The electron near the cathode is accelerated towards the anode and collides with a neutral Ar atom converting it to a positively charged ion.



The interaction result exhibits two atoms of the electron which can collide with other gas atoms and ionize by creating a cascading process until the gas breaks down. The breakdown voltage depends on the pressure and the distance between the anode and the cathode. The interactions between the incident ions and the target are not only the sputtered atoms but also causes the generation of secondary electrons and reflected ion and neutrals. ions bombardment may be implanted into the target material [20]. The secondary electron is maintained the glow discharge process. The sputtered atoms are coated onto the substrate in the formed of neutral atoms.

The sputtered atoms are sputtered by bombardment with ions having a few hundred electron volts. These sputtered atoms are partially ionized, i.e., a few percents of the sputtered atoms, in the discharge region of the sputtering system. An alloy target, if low energy of incident ions have interacted, most of the sputtered atoms are composed of the alloy.

The principle of ions collision with the target is energy and momentum conservation. In any collision, momentum is typically conserved. If the collision is elastic, kinetic energy is also conserved. The energies required for sputtering are higher than lattice bonding which are the causes of inelastic interactions. Therefore, sputtering collisions can be considered elastic.

1. Momentum and Energy

Momentum (P)

$$P = mv \quad (2.50)$$

Kinetic energy (K)

$$K = \frac{1}{2}mv^2 \quad (2.51)$$

Momentum conservation, total momentum before = total momentum after

$$m_1 v_{1i} + m_2 v_{2i} = m_1 v_{1f} + m_2 v_{2f} \quad (2.52)$$

Kinetic energy conservation, total kinetic energy before = total kinetic energy after

$$\frac{1}{2}(m_1 v_{1i}^2 + m_2 v_{2i}^2) = \frac{1}{2}(m_1 v_{1f}^2 + m_2 v_{2f}^2) \quad (2.53)$$

As seen in figure 2.13, the maximum energy transfer between two masses in the forward direction in such a collision occurs when the masses are equal.

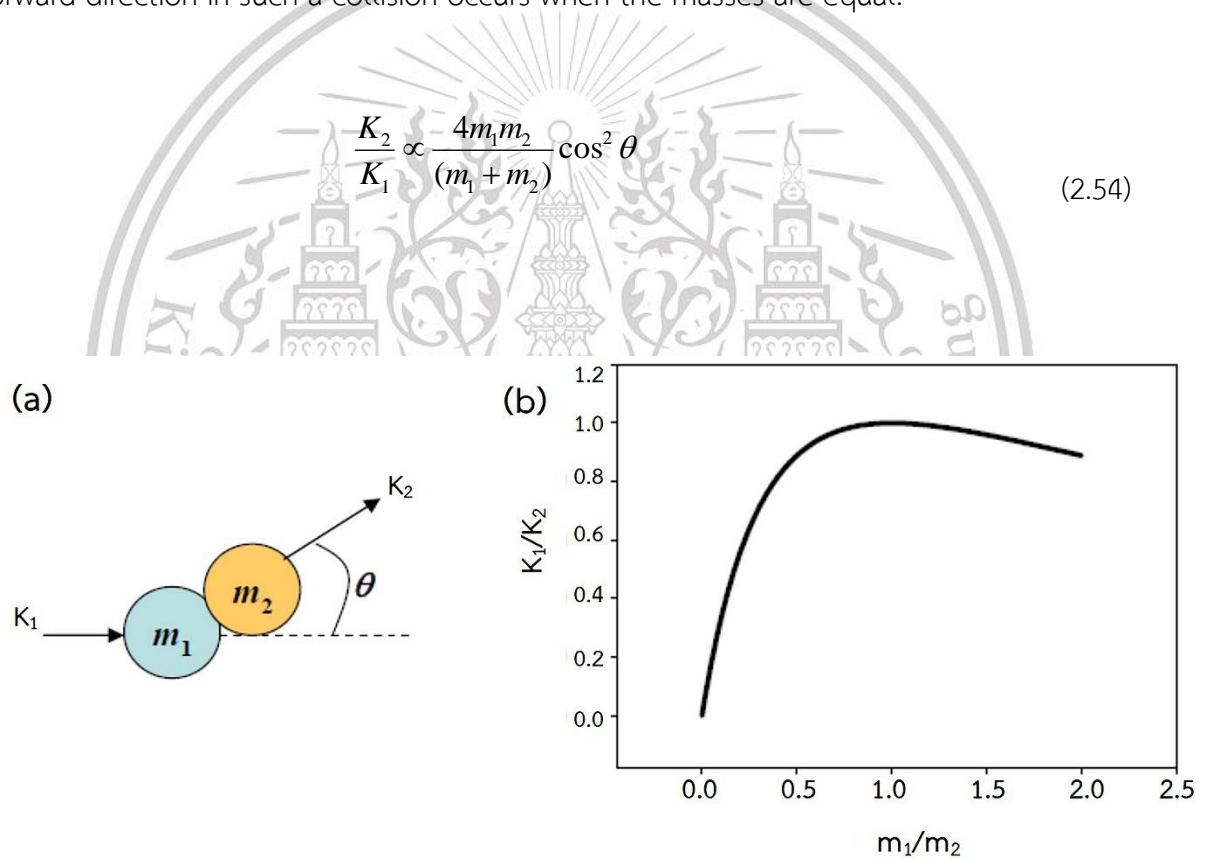


Figure 2.14 (a) Kinetic energy transfer (b) kinetic energy transfer between two masses in the forward direction.

2. Mean free path

The energy of sputtered atoms is typically higher than that of thermally evaporated atoms in a vacuum. The energy of sputtered atoms depends on the incident ion species and the incident bombardment angles.

The mean free path of the sputtered atoms, which pass through the glow discharge space, is given by

$$\lambda_1 \cong \frac{c_1}{\nu_{12}} \quad (2.55)$$

Where c_1 is the sputtered atoms velocity and ν_{12} is the collision frequency between sputtered atoms and sputtering gas. The sputtered atoms velocity is larger than the sputtering gas, ν_{12} is given by:

$$\nu_{12} \cong \pi(r_1 + r_2)^2 c_1 n_2 \quad (2.56)$$

Where r_1 and r_2 are the atomic radius of sputtered atoms and sputtering gas, respectively, n_2 is the density of discharge gas. The mean free path is given by:

$$\lambda_1 \cong \frac{1}{\pi(r_1 + r_2)^2 n_2} \quad (2.57)$$

2.6.2 Sputtering yield

The sputtering yield (**S**) is defined as the mean number of atoms removed from the target due to bombardment per incident ions and is given by:

$$S = \frac{\text{Sputtered atoms}}{\text{Incident ions}} \quad (2.58)$$

The sputtering is the interaction of incident ions with target atoms. The sputtering yield will be influenced by these factors:

- The energy of incident ions
- The incident angle of ions

- The masses of the ions and target atoms
- Sputtering target: the binding energy of the target atoms and relative mass of ions

The sputtering yield can be measured by the following methods: 1) Weight loss of sputtering target, 2) Decrease of thickness target, 3) Collection of the sputtered material and 4) Detection of sputtered ions.

The momentum transfer theory and thermal vaporization theory have been proposed for sputtering. The sputtering process is initiated by the collision between incident ions and target atoms. The displacement of target atoms will be more isotropic due to successive collisions and atoms may finally move from the target. The sputtering yield is insensitive to the temperature of the target except at a very high temperature. It will be shown the increase in the sputtering rates due to accompanying the thermal evaporation. The mechanism of sputtering is considered in detail for the following three different energy regions of the incident ions.

1. Threshold region ($E < 100$ eV)
2. Low-energy region ($E > 100$ eV)
3. High-energy region ($E = 10$ -100 keV)

The threshold region is the energy for ejecting target atoms. The sputtering yield increases with increasing the higher energies in the low-energy region. The saturation of sputtering yield has occurred at the high-energy region for heavier bombarding

According to the elastic-collision theory, the possible energy transferred in the collision process (T_m) is followed by:

$$T_m = \frac{4M_1M_2}{(M_1 + M_2)^2} E \quad (2.59)$$

Where, M_1 and M_2 are the mass of the incident ions and target atoms, respectively. E is the kinetic energy of incident ions. In the first order of approximation, the sputtering yield is proportional to T_m . The sputtering yield (S) of the target material bombarded with different element is given by:

$$S = k \frac{1}{\lambda(E) \cos \theta} \frac{M_1 M_2}{(M_1 + M_2)^2} E \quad (2.60)$$

Where k is a constant which depends on the target material, λ is the mean free path for elastic collisions near the target, θ is the direction of incidence ions. The mean free path is given by:

$$\lambda = \frac{1}{\pi R^2 n_0} \quad (2.61)$$

Where n_0 are the numbers of lattice atoms per unit volume. R is the collision radius in the sphere model.

Finally, the sputtering yield is expressed by the relationships where

1. <1 keV

$$S(E) = (3/4\pi^2) \alpha T_m / U_0 \quad (2.62)$$

2. 1-10 keV

$$S(E) = 0.420 \alpha S_n(E) / U_0 \quad (2.63)$$

Where, T_m is the possible energy transferred in the collision process, U_0 is a heat of sublimation and α is the function of M_2/M_1 .

However, the sputtering yield is depending on the energy of the incident ions, target materials and angle of incidence ions. Sputter yields increase as the mass of incident ion increases due to a process of momentum transfer and also tends to increase as the kinetic energy of incident ions above the threshold energy [35].

2.6.3 The practical aspect of sputtering systems

For the operation of the sputtering system, many equipments are prepared including the sputtering target, sputtering gas, substrate and monitor systems.

1. Sputtering target

The sputtering target is typically made from metal or alloy compound disk. Typically, the diameter is 5-8 cm for research and 15-30 cm for production. A rectangular is used for production. In the sputtering process, the sputtering target is mounted on a water-cooled backing plate by mechanical support. It is surrounded by a dark space, known as a ground shield. When input the power appears as target heating. Rotation of the substrate holder is often used to obtain a uniform composition.

Typically, the compound target is widely used in a single target system. It can be deposited by direct sputtering from the sintered powder of the compounds material. The thickness distribution of the sputtered film is governed by the construction of a magnetic core. The magnetron cathode comprised a permanent magnet. The magnetic flux density of the magnetic core is occurred on the target surface. The magnetron is covered by a permalloy sheet which confines the leakage magnetic flux.

However, the thickness distribution of sputtered films is governed by several factors such as the angular distribution of the sputtered atom, the collisions between sputtered atoms and sputtering gas and the construction of the target shield.

2. Sputtering gas

Typically, the deposition process of the film is affected by the deposition rates (the power density) and the gas pressure. The sputtering gas is widely used an inert-gas (generally a heavy gas, Ar). In the sputtering process, a plasma is created by ionizing a sputtering gas. The sputtering gas bombards the target and sputters off the material to deposit.

At low pressures, higher ions energy increases the deposition rate/sputtering yield. There are not enough collisions between ions and sputtering target atoms to contribute a plasma which deposition rate. On the other hand, at high pressures, there are many collisions that electrons do not have enough time to gather energy between collisions to be able to ionize the atoms. Therefore, the sputtering gas was optimized for providing the deposition rate of the film production. The optimum pressure depends on target-substrate configurations.

3. Substrate

In this work, Sb_2Te_3 films were directly deposited on a flexible polyimide substrate. Polyimide is widely used as a dielectric substrate for its high-temperature resistance, self-extinguishing burn characteristics, toughness and flexibility. It has been used successfully in applications at temperatures as low as $-269\text{ }^\circ\text{C}$ and as high as $400\text{ }^\circ\text{C}$. Moreover, to form a flexible thermoelectric device, polyimide used as a substrate was chosen due to its low thermal conductivity ($0.12\text{ Wm}^{-1}\text{K}^{-1}$) and thermal expansion coefficient ($12 \times 10^{-6}\text{ K}^{-1}$) which closely matches that of the Sb_2Te_3 films. Besides, polyimide can reduce residual stress and increase adhesion in the film.

The temperature rise at magnetron is reduced because the secondary electrons from the target are trapped by the magnetic field near the surface of the cathode target.

4. monitoring systems

The monitoring of sputtering conditions is important to control the properties of the film production. The parameters to be monitored are as follows:

1. Sputtering discharge
 - Voltage
 - Current
 - Power density

2. Sputtering gas in the sputtering chamber
 - Residual gas
 - Total/partial pressure of the sputter gas
3. Substrate temperature

4.1 Sputtering discharge:

The discharge parameters (the sputtering voltage and the sputtering current) can be easily measured by a conventional high impedance voltmeter and a low impedance current meter for DC sputtering.



Figure 2.15 DC power of the sputtering system.

4.2 Sputtering gas:

The gas composition and sputtering pressure in the chamber are measured by a vacuum gauge. When the sputtering gas is introduced into the ion source chamber, the sputtering gas is ionized and resulting ions are accelerated. The concentration of the total/partial pressure of sputtering gas is generally fed to the system through a stainless steel pipe. The non-uniformity in partial gas density during sputter results in non-uniformity in the chemical composition of film production. The gas flow is controlled by a leaking valve. The gas flow is controlled by a mass flow controller.



Figure 2.16 Mass flow controller.

4.3. Substrate temperature:

The substrate temperature is measured by a thermocouple. A 1000 W quartz lamp was used to heating the substrate. The position of the thermocouple was fixed nearly the glass slide as shown by the schematic diagram in figure. 2.17. This reading temperature from a thermocouple called reference temperature (T_{ref}). The temperature control unit was used for setting the T_{ref} . It can be assumed that the T_{ref} is the substrate temperature (T_{sub}) from the calibration. The relationship between T_{ref} and T_{sub} was measured. The thermocouple was contacted under of the polyimide substrate.

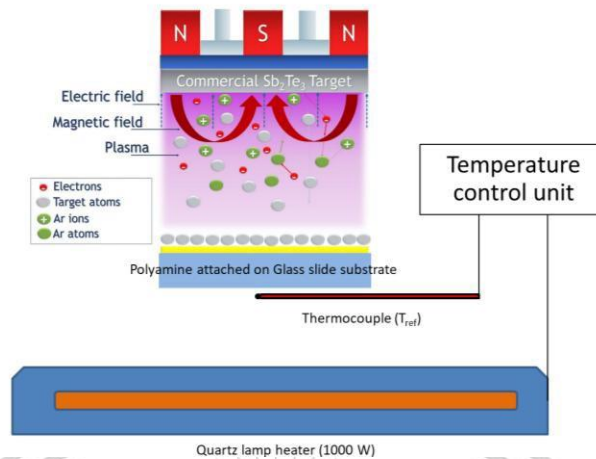


Figure 2.17 Schematic diagram of substrate temperature.

In the sputtering process, sputtered atoms are transported and diffused on the surface of the substrate are called adatoms. The interactions of adatoms and substrate are delicate. The control of film quality is necessary for both scientific research and applications. Fundamentals of the controlling film quality are described in the following sections which are governed by chemical composition, crystal structure, phase structure, uniformity and film stress. The chemical composition is governed by the chemical composition of a material, composition of sputtered atoms, gas atoms, the surface reaction of adatoms, and Interdiffusion between adatoms and substrate. The crystal structure properties are governed by the stoichiometry, Impurity atoms and phase separation. Their physical, chemical, electrical and mechanical properties are affected by the growth process. In the growth process, it is important to understand the relation between the film properties and the sputtering parameters.

2.7 Characterization techniques

In this study, characterization techniques of sputtered Sb_2Te_3 and Bi_2Te_3 films are described. The experimental techniques to analyze thermoelectric film properties including physical, chemical, electrical and thermoelectric are presented.

2.7.1 X-ray diffraction (XRD)

X-ray diffraction technique is used for phase identification of a crystal structure and atomic spacing of materials which can be obtained through electron and neutron diffraction and determined of unit cell dimension. In typical, X-rays are generated by a cathode tube, filtered to produce monochromatic radiation, collimated and directed to the materials. The interaction between the incident rays and sample material produce constructive interference and diffraction rays when the condition satisfy the Bragg's law, as seen in the Figure. 2.18.

$$2d \sin \theta = n\lambda \quad (2.64)$$

Where d is the spacing of atomic plane measured in perpendicular to the planes, θ is Bragg's angle measured between the incident direction and the planes, n is an integer that presents the order of reflection and λ is the wavelength of X-rays.

The Bragg's law relates to the diffraction angle of X-rays radiation and the lattice spacing in a crystalline material. The X-rays diffraction were obtained by scanning sample material in the range of 2θ angles, all diffraction direction of the lattice are attained due to the random orientation of the materials.

The diffraction patterns have conversed with d-spacing leads to the identification of the mineral because each mineral has a unique d-spacing. The standard reference pattern (JCPDS card) is achieved by comparison of d-spacing.

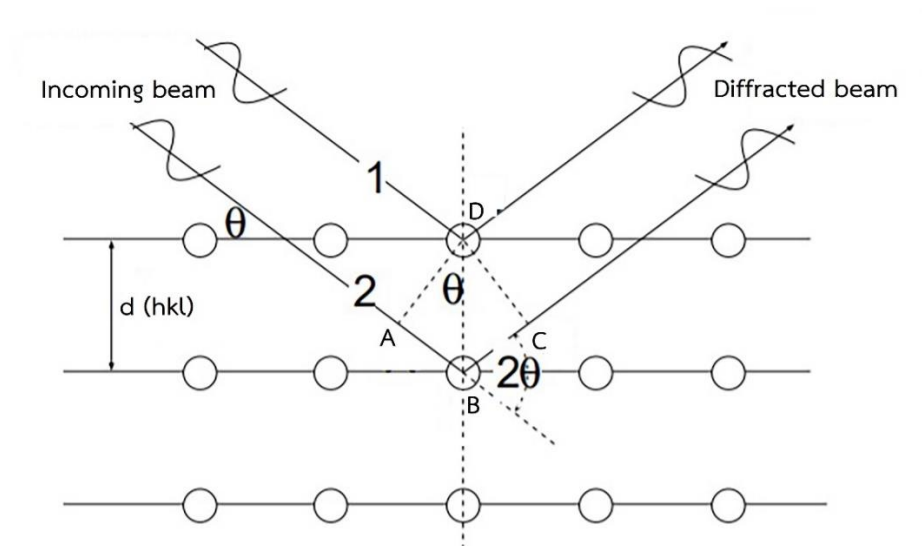


Figure 2.18 Bragg's law.

X-ray diffractometers consist of an X-ray tube, sample holder and X-ray detector. Cathode tube generates X-ray by the heating filament to introduce electrons. The acceleration of electrons toward a target material was done by applying a high voltage, then the bombarding occurred. When electrons have sufficient energy to dislodge inner shell electrons of the target material, characteristic X-ray spectra are produced. In typical, Copper is a common target material to produce monochromatic radiation with $\text{Cu-}K_{\alpha}$ radiation ($\lambda = 1.5418 \text{ \AA}$). Then, the collimated X-rays are directed to the sample. The intensity of reflected X-rays is recorded by rotating the detector. When the incident X-rays impinging the sample satisfies the Bragg Equation, constructive interference occurs and a peak intensity occurs. A detector records the signal data and converts to a count rate which is then output to a monitor.

The Scherer equation is a formula that relates the crystalline size in a sample to the broadening of a diffraction peak. The Scherrer equation can be written as:

$$D = \frac{k\lambda}{\beta \cos \theta} \quad (2.65)$$

Where D is a crystalline size, k is the Scherer constant (0.94), λ is the X-ray wavelength, β is the line broadening at half the maximum intensity (FWHM) and θ is the Bragg angle.

Many factors may contribute to the observed diffraction peak profile such as instrument, crystalline size, temperature and microstrain. The most important factor is the microstrain. In general, microstrain corresponds to atom displacements concerning their position in crystals which are free of any defects including non-uniform lattice distortion, dislocation, antiphase domain boundaries and grain surface relaxation.

The diffraction peaks can be apparent to the crystalline size by the Scherrer equation. And their microstrain, Williamson and Hall suggested a method for finding both, called the Williamson-Hall (W-H) method [38]. The W-H method is a formula that relates to the effect of crystallite size (β_D) and microstrain (β_ε), as seen in equation (2.70).

$$\beta_T = \beta_D + \beta_\varepsilon \quad (2.66)$$

Where β_T is the total broadening, β_D is the broadening due to crystalline size and β_ε is the broadening due to strain. From the Scherer equation (2.65) known that

$$\beta_D = \frac{k\lambda}{D \cos \theta} \quad (2.67)$$

The peak broadening due to microstrain is given by:

$$\beta_\varepsilon = 4\varepsilon \tan \theta \quad (2.68)$$

Where ε is the strain and θ is the peak position. So,

$$\beta_T = \frac{k\lambda}{D \cos \theta} + 4\varepsilon \tan \theta \quad (2.69)$$

Or

$$\beta_r \cos \theta = 4\varepsilon \sin \theta + \frac{k\lambda}{D} \quad (2.70)$$

Equation (2.74) represents a straight line, which ε is the slope of the straight line and $\frac{k\lambda}{D}$ is the y-intercept.

2.7.2 Field-emission scanning electron microscopy (FE-SEM)

The field emission scanning electron microscopy provides topographical and elemental information on the specimen. The electron microscope is also limited by the wavelength of the electron. Since the wavelength of the electron is small, the subatomic resolution can be obtained.

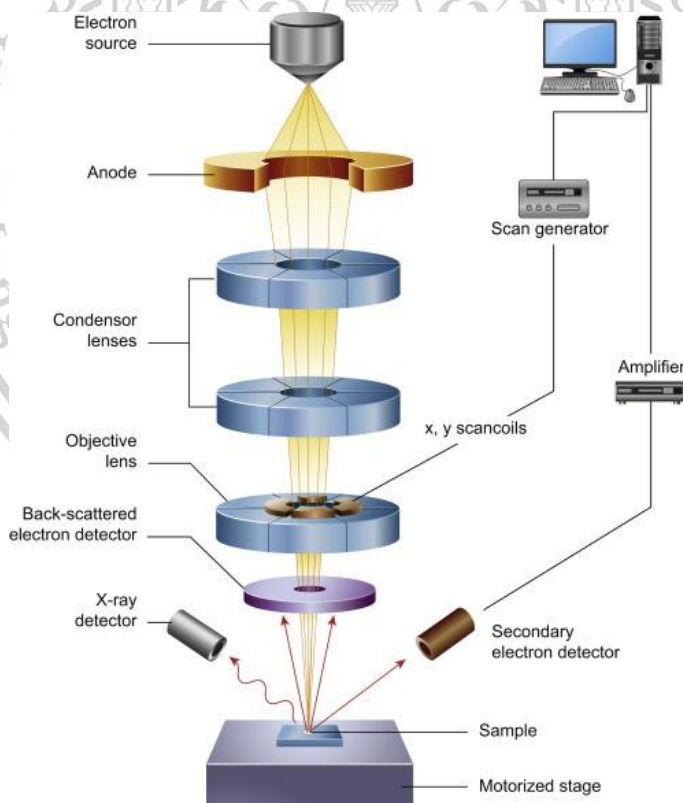


Figure 2.19 Schematic of field-emission scanning electron microscope.

This material is reserved for educational use only, not allowed for commercial use.

Forbidden to modify the content, and cite the document when use.

The electron microscope works with an electron in a negative charge instead of visible light in an optical microscope. Therefore, all samples work with FE-SEM must be conductive under vacuum. The electrons were created by a field emission source made from tungsten filament. A direct current is passed through the filament which heats it about 2700 K. At temperature, the filament emits electrons into the surrounding vacuum by the process called thermionic emission. The high energy electron is accelerated from the filament by applied voltage (0.5-30 kV) within the high vacuum column, called primary electrons. The anode has a pinhole to collimated the electrons beam. The collimated electron pass through a magnetic lens which focuses them to spot on the specimen. The scan coils deflect the electron beam over the object according to a zig-zag pattern. The formation of the image on the monitor occurs in synchrony with the scan movement. The objective lens is the lowest in the column. It can focus the electron beam on the object. After the primary electrons are focused and deflected by electronic lenses to produce a narrow scan beam that bombards the specimen. The atomic electrons ejected from the specimen at low energy (less than 100s of eV) as a result of inelastic scattering are emitted, as known that secondary electrons. Furthermore, the incident electron with high energy (keV) that scattering in elastic through more than 90° as called backscattering electrons. X-ray is also created when core-shell electrons in the specimen are knocked loose, and valence electrons fall into the vacancies using the EDX detector to provide the elemental information. The angle and velocity of these secondary electrons relate to the surface structure of the specimen. A detector catches the secondary electrons and produces an electronic signal that reflects the surface microstructure morphology of the specimen. The signal is amplified and transformed into a screen. FE-SEM provides great topological, chemical compositions that come from different detectors.

Energy-dispersive X-ray spectroscopy (EDS) is an analytical function used for the elemental detector, the pulse processor and the analyzer. The X-ray detector is used to detect and convert the electronic signals. Then, the pulse processor is used to measure the electronic signals for determining the energy of the X-ray detector. After that, the analyzer is used to display and identify the elemental composition.

Finally, the fatigue-cracked specimen surfaces, cross-sections and elemental composition of the specimen were obtained.

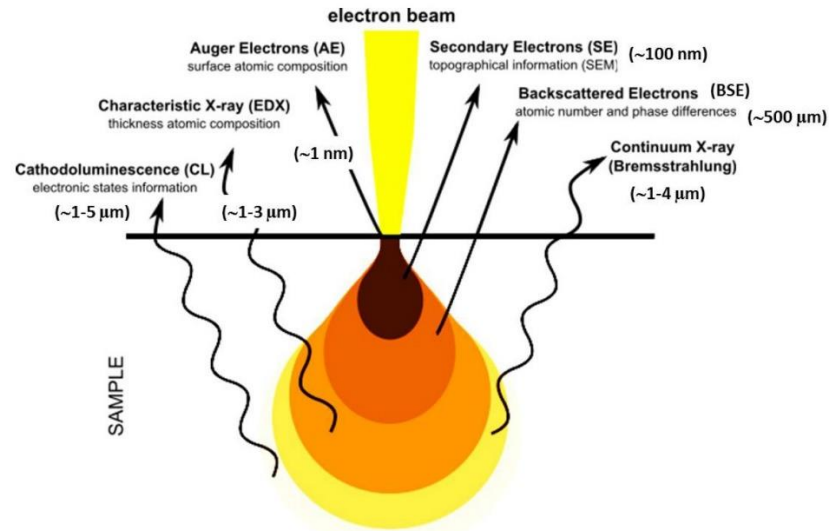


Figure 2.20 Signals generated at electron-specimen interactions.

2.7.3 Hall effect measurement

The Hall effect measurement provides the electrical transport properties of conducting materials. For thermoelectric material, carrier types and electrical mobility can be determined by Hall effect measurement. The Hall effect is based on the Lorentz force acting on the charge carriers moving in a magnetic field. When electrical current (I) flows through a conductor material in the perpendicular to a magnetic field, the magnetic field (B) exerts a Lorentz force on a charge carrier moving, pushing them to one side of the conductor. The combination of the current and the applied magnetic field induces a voltage difference across a conductor, as known as the Hall voltage (V_H). The set up of the Hall effect measurement is shown in the Figure. 2.24. The Hall coefficient (R_H) is defined in equation (2.75).

$$R_H = \frac{E}{jB} \quad (2.71)$$

Where j is the current density of the carrier of electron and E is an electric field. Charge carriers in a magnetic field are subject to the Lorentz force, given by:

$$F = q(v \times B) \quad (2.72)$$

Where q is the charge of carrier and v is the drift velocity of the current. If electric force (qE) is equal to the Lorentz force, the electric field is given by:

$$E = v \times B \quad (2.73)$$

The drift velocity of the current or the velocity of the carriers is related to the current density, expressed as equation (2.78).

$$j = n_c q v \quad (2.74)$$

Where n_c is the charge carrier concentration. So, the electric field can be defined as:

$$E = \frac{jB}{qn_c} \quad (2.75)$$

From the Hall coefficient definition in equation (2.75), the carrier type and the carrier concentration is derived to be:

$$n_c = \frac{1}{R_H q} \quad (2.76)$$

If the Hall coefficient is positive, the carrier type is hole or P -type and the Hall coefficient is negative, the carrier type is electron or N -type. The carrier mobility (μ) is determined by the electrical resistivity (ρ) and hall coefficient, given by:

$$\mu = \frac{R_H}{\rho} \quad (2.77)$$

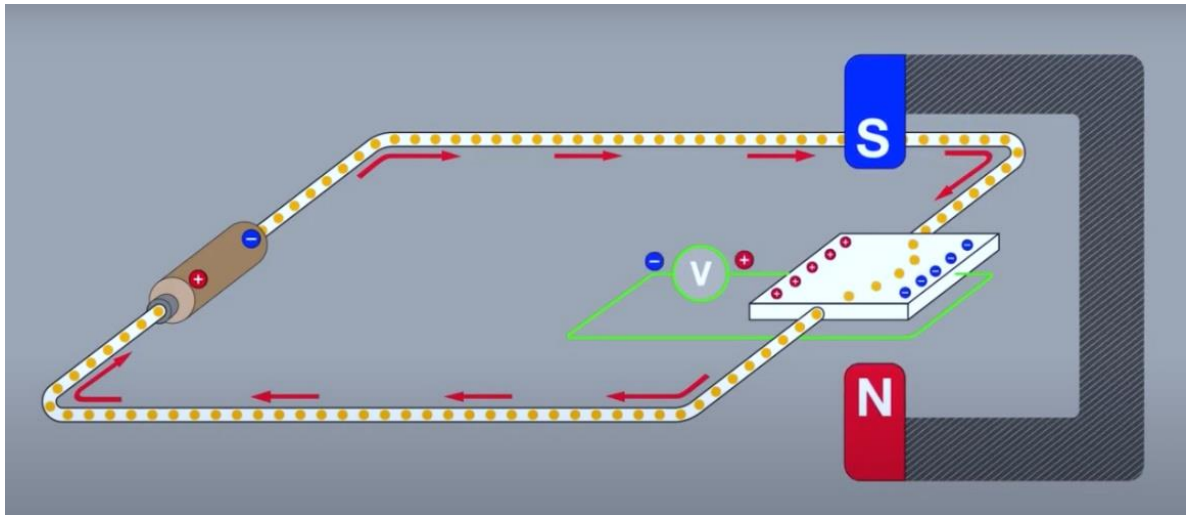


Figure 2.21 Hall effect measurement set up.

In general, a few simple instruments of Hall effect measurement are required a current source (100 mA-10 PA), a voltmeter, a current meter and a magnetic field. The Van der Pauw is the common geometry to determine the electrical resistivity using either a four-point probe. In this case, the film was placed on a square substrate. The current is applied to two adjacent contacts and voltages are measured between the other two. Van der Pauw equation for material resistivity is given by [44]:

$$\rho = \frac{\pi}{\ln 2} ft \frac{(R_{1234} + R_{2341})}{2} \quad (2.78)$$

To measure the hall voltage, the contact configuration will be rearranged. the current source and the measured voltage are applied across opposite contacts. To obtain the precise result of the hall voltage, the recommended technique involves a combination of reversing source current polarity, sourcing on additional terminals, and reversing the direction of the magnetic field.

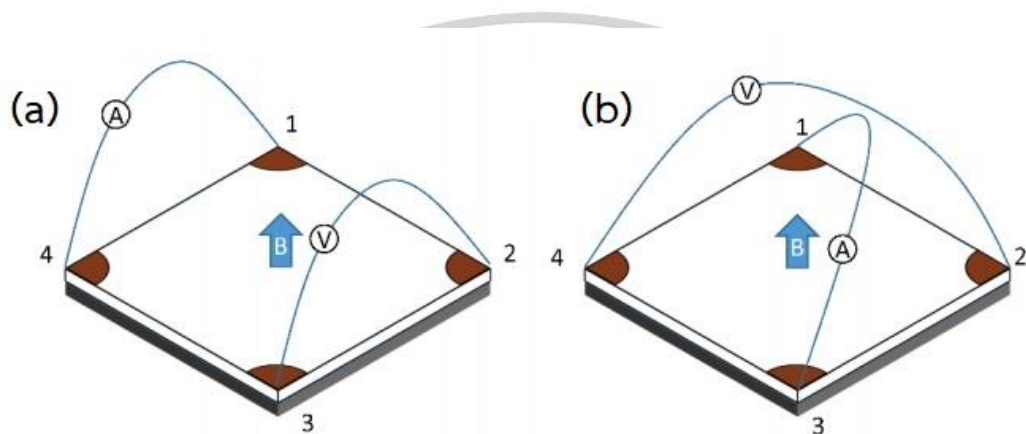


Figure 2.22 Schematic of van der Pauw set up (a) for material resistivity and (b) for hall voltage measurements.

2.7.4 Seebeck Coefficient/Electrical Resistance Measurement System (ZEM-3)

Seebeck coefficient and electrical resistivity are standards for thermoelectric material measurement which widely used with material including metals, semiconductors and oxides. ZEM-3 measurement is to measure the voltage difference of the sample material under the temperature gradient. The schematic of ZEM-3 is shown in figure 2.23. The electrical arrangement is set the sample in a vertical position in the infrared heating furnace under low-pressure helium ambient. While the sample is heated, the temperature gradient (ΔT) across the sample was measured. Two thermocouples were pressed at the surface of the sample to measure the thermal electromotive force (dE). Following the Seebeck equation, the Seebeck coefficient is obtained. Electrical resistance (R) is measure

via the dc four-terminal method. The electrical current (I) was applied through the sample between current electrodes. The voltage (dV) drop when the current flows between the sample wires were measured. Ohm's law, the dimension of the sample is used to convert the resistance to resistivity (ρ), as seen in equation (2.79).

$$R = \frac{\rho L}{A} \quad (2.79)$$

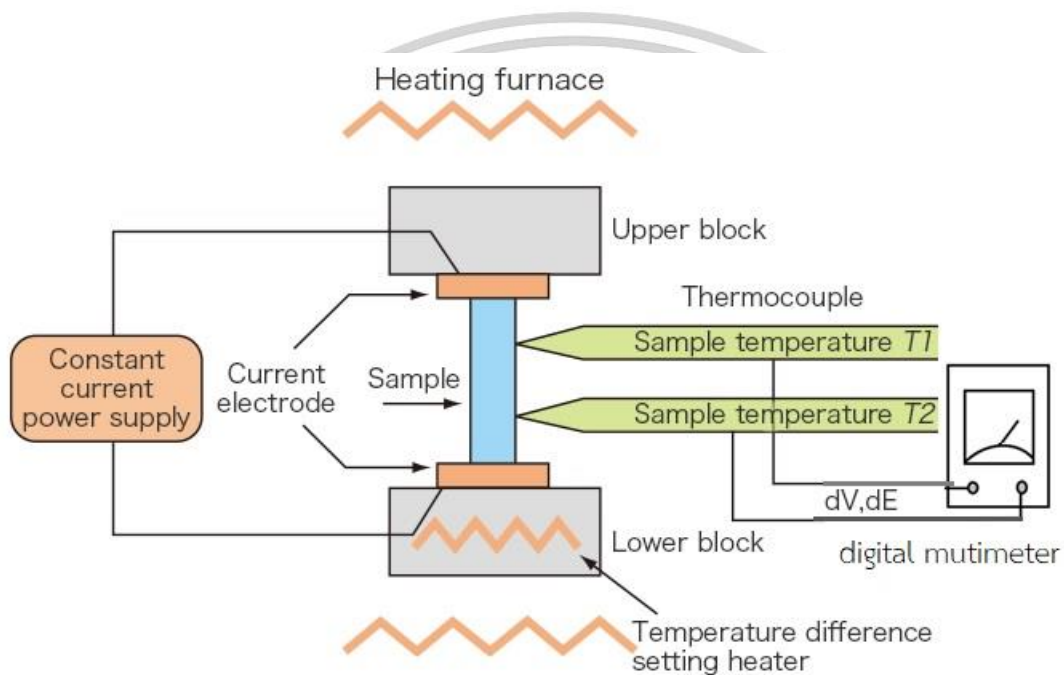


Figure 2.23 Schematic of Seebeck Coefficient/Electrical Resistance Measurement System.

2.7.5 Thin Film Analyzer (TFA) [38]

1. Electrical conductivity and Hall coefficient

To determine the electrical conductivity (σ) and Hall coefficient (A_H) of the sample, the Van-der-Pauw method is used in combination with the needle contacts 2, 3, 8, and 9. The shadow mask, which was used during the deposition process, defines

the optimum contact position in terms of symmetry and location at the very edge of the sample.²⁰ For the resistivity measurement, a current is applied between two contacts at one edge and the corresponding voltage drop is measured between the remaining two electrodes. After cyclic changing of the contacts, the measurement is repeated and the resistivity ρ can be calculated solving the Van-der-Pauw formula

$$\exp\left(-\frac{\pi t_s}{\rho} \cdot R_{23,98}\right) + \exp\left(-\frac{\pi t_s}{\rho} \cdot R_{39,82}\right) = 1 \quad (2.80)$$

with

$$R_{23,98} = \frac{V_{98}}{I_{23}}, \quad (2.81)$$

A common measurement procedure for the DC Van-der-Pauw method, including polarity reversal of the applied current in order to cancel out occurring offset voltages, has been presented by NIST and can be found here.

2. Seebeck coefficient

For the determination of the sample's Seebeck coefficient, a resistance thermometer with a small sample contact $V_{TH,H}$ has been structured near the heating stripe on the big membrane. This contact is electrically connected to pad 1, which is used as the hot contact for the thermovoltage measurement. As cold contact, pad 8 is used, which is located on the bulk silicon and remains at T_0 , even when a temperature gradient is applied to the membrane. For the measurement, a current is applied to the heating stripe between the pads 7 and 10, causing a temperature gradient along the membranes' x-axis, starting at the heating stripe and ending at the platinum rim. For the temperature determination of the hot contact, the resistance of the thermometer is measured in a 4-point configuration using the pads 1, 4, 5, and 6 (T_{hot}). The required temperature coefficient of resistance is again calibrated using the thermocouple directly under the chip at thermal equilibrium conditions during the

measurement routine. The same thermocouple is also used for the determination of the cold contact temperature $T_{\text{cold}} = T_0$

$$T_{\text{hot}} \sim \frac{V_{14}}{I_{56}}. \quad (2.82)$$

For the Seebeck measurement procedure at a certain temperature point, various temperature gradients in the x-direction of the membrane are applied, and the temperature difference, $\Delta T = T_{\text{hot}} - T_{\text{cold}}$, as well as the thermoelectric voltage V_{th} between pads 1 ($V_{TH,H}$) and 8 ($V_{TH,C}$) is measured successively at steady state conditions. The Seebeck coefficient can then be evaluated using

$$S - S_{\text{Pt}} = \frac{-V_{th}}{\Delta T} = \frac{-(V_{TH,H} - V_{TH,C})}{T_{\text{hot}} - T_{\text{cold}}}, \quad (2.83)$$

where S_{Pt} denotes the Seebeck coefficient of the platinum contacts. When the applied temperature rise, at a certain temperature measurement point, is small enough to stay within the constant regime of the sample's Seebeck coefficient over temperature, the evaluation can also be done by plotting the measured thermovoltage over the applied temperature gradient and taking the slope of this graph as the Seebeck coefficient.

3. Thermal conductivity measurement

To determine the thermal conductivity, specific heat c_p , and emissivity of thin films, an advanced setup based on the setup presented by Volklein et al. is used [see Figs. 2.24(a)– 4(c)]. For the measurement, two thin heating/sensor stripes with a width $<5 \mu\text{m}$ are deposited on the front side of the two free standing Si_3N_4 membranes with different geometries. A platinum rim surrounding the membranes has been added, in order to act as a well-defined heat sink, correcting unavoidable uncertainties in the membrane size arisen during the production process. Because of this, a high reproducibility can be realized without additional geometry measurements. In contrast to the previously published setup for this configuration, the sample is deposited on the top side of the membrane, requiring an additional dielectric layer avoiding shortcuts

with the heater when investigating electrically conductive samples. The additional thermal conductance $G_{Al_2O_3}$ through the passivation layer is a crucial factor and can hamper the capability of the setup, as the thermal conductance of the sample G_S should be at least in the same order of magnitude or bigger than the thermal conductance G_m of the measurement setup consisting of the Si_3N_4 membrane and Al_2O_3 passivation layer,

$$\lambda_s t_s = G_s \geq G_m = \lambda_{Si_3N_4} t_{Si_3N_4} + \lambda_{Al_2O_3} t_{Al_2O_3} = \lambda_m t_m. \quad (2.84)$$

In this formula, λ_i is the thermal conductivity and t_i is the thickness of the sample s , measurement setup m , silicon nitride Si_3N_4 , and alumina oxide Al_2O_3 . As the passivation layer is 30 nm thick, with a measured thermal conductivity of 1.4W/mK at room temperature, the thermal conductance of the measurement setup is increased by only 15% and now allows the usage of new deposition techniques which grow thin films from the liquid phase. In contrast to the previously published measurement chip, where the film under investigation has to be deposited into the etched holes, the surface of the chip is now flat, making it possible to deposit a thin film with homogeneous thickness, using spin coating, drop casting, or ink-jet printing.

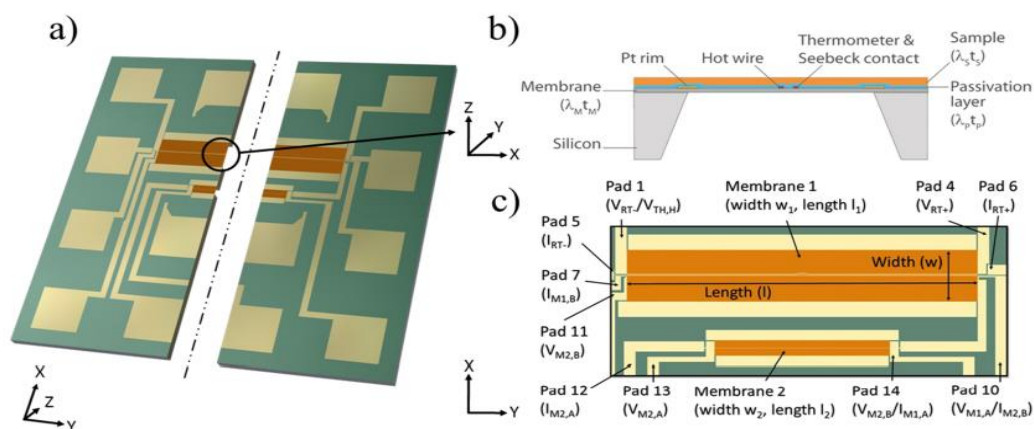


Figure 2.24 Cut through the chip (a) and schematic cross-sectional view of the big membrane including thermometer (b). Top view of the two-membrane setup including heating stripes and resistance thermometer. $I_{Mi,A}$, $I_{Mi,B}$ as well as $V_{Mi,A}$ and $V_{Mi,B}$ are the current and voltage connection pads for the two heaters on membranes 1 and 2, I_{RT} and V_{RT} are the connection pads for the resistance thermometer, and $V_{TH,H}$ is the pad for the hot contact of the thermovoltage measurement (c).

2.7.6 X-Ray Photoelectron Spectroscopy

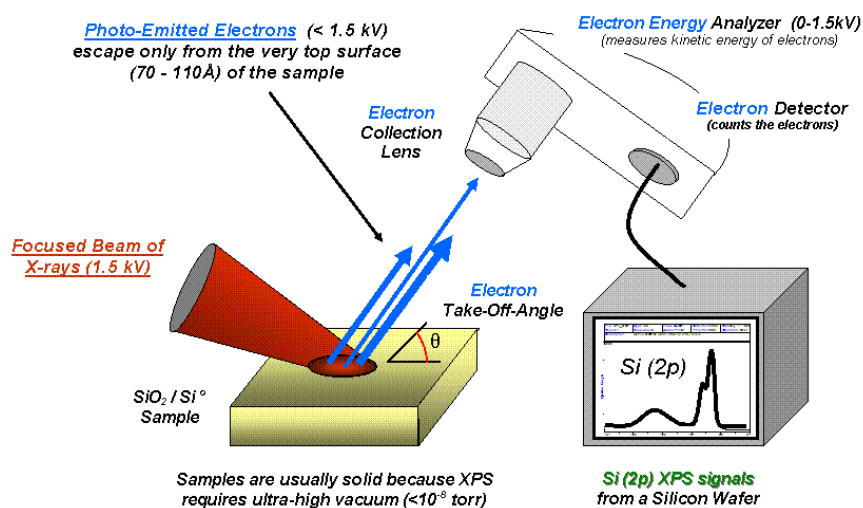


Figure 2.25 X-Ray Photoelectron Spectroscopy Measurement System.

This material is reserved for educational use only, not allowed for commercial use.

Forbidden to modify the content, and cite the document when use.

Figure 2.25 show the X-Ray photoelectron spectroscopy measurement System. X-ray Photoelectron Spectroscopy (XPS) also known as Electron Spectroscopy for Chemical Analysis (ESCA) is the most widely used surface analysis technique because it can be applied to a broad range of materials and provides valuable quantitative and chemical state information from the surface of the material being studied. The average depth of analysis for an XPS measurement is approximately 5 nm. PHI XPS instruments provide the ability to obtain spectra with a lateral spatial resolution as small as 7.5 μm . Spatial distribution information can be obtained by scanning the micro focused x-ray beam across the sample surface. Depth distribution information can be obtained by combining XPS measurements with ion milling (sputtering) to characterize thin film structures. The information XPS provides about surface layers or thin film structures is important for many industrial and research applications where surface or thin film composition plays a critical role in performance including: nanomaterials, photovoltaics, catalysis, corrosion, adhesion, electronic devices and packaging, magnetic media, display technology, surface treatments, and thin film coatings used for numerous applications. XPS is typically accomplished by exciting a samples surface with mono-energetic Al $K\alpha$ x-rays causing photoelectrons to be emitted from the sample surface. An electron energy analyzer is used to measure the energy of the emitted photoelectrons. From the binding energy and intensity of a photoelectron peak, the elemental identity, chemical state, and quantity of a detected element can be determined. Physical Electronics XPS instruments function in a manner analogous to SEM/EDS instruments that use a finely focused electron beam to create SEM images for sample viewing and point spectra or images for compositional analysis. With the PHI XPS instruments, a finely focused x-ray beam is scanned to create secondary electron images for sample viewing and point spectra or images for compositional analysis. The size of the x-ray beam can be increased to support the efficient analysis of larger samples with homogeneous composition. In contrast to SEM/EDS which has a typical analysis depth of 1-3 μm , XPS is a surface analysis technique with a typical analysis depth of less than 5 nm and is therefore better suited for the compositional analysis of ultra-thin layers and thin microscale sample features.

2.8 Literature Reviews

P. Junlabhut et al. [20] study effect of sputtering power on thermoelectric properties of Sb_2Te_3 thin films deposited by DC magnetron sputtering technique. Effect of sputtering power can be improved structural of Sb_2Te_3 thin films as show in figure 2.26(a) and improved power of Sb_2Te_3 thin films as show in figure 2.26(b). The best sputtering power for deposited Sb_2Te_3 thin films about 45 Watt.

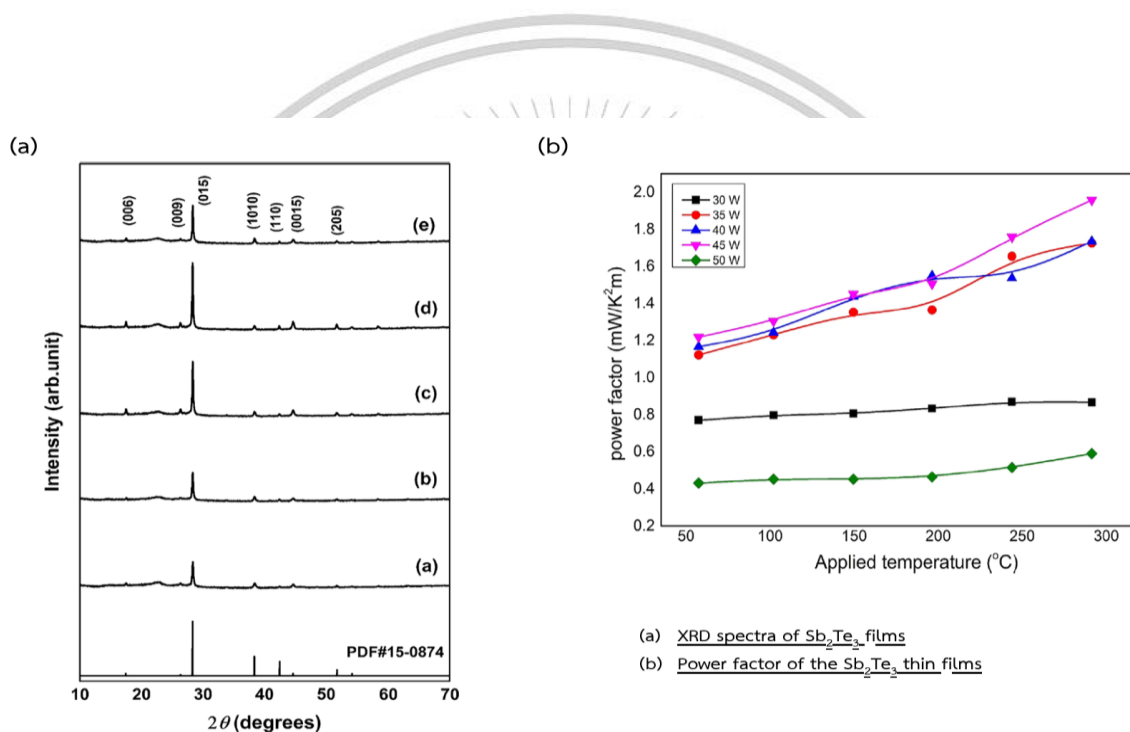


Figure 2.26 Influence of sputtering power on (a) structural and (b) power factor of films.

N. Somdok et al. [39] study effect of sputtering pressure on thermoelectric properties of Bi_2Te_3 thin films deposited by DC magnetron sputtering technique. Effect of sputtering pressure can be improved structural of Bi_2Te_3 thin films as show in figure 2.27(a) and improved power of Bi_2Te_3 thin films as show in figure 2.27(b). The best sputtering pressure for deposited Bi_2Te_3 thin films about 1.8×10^{-2} mbar.

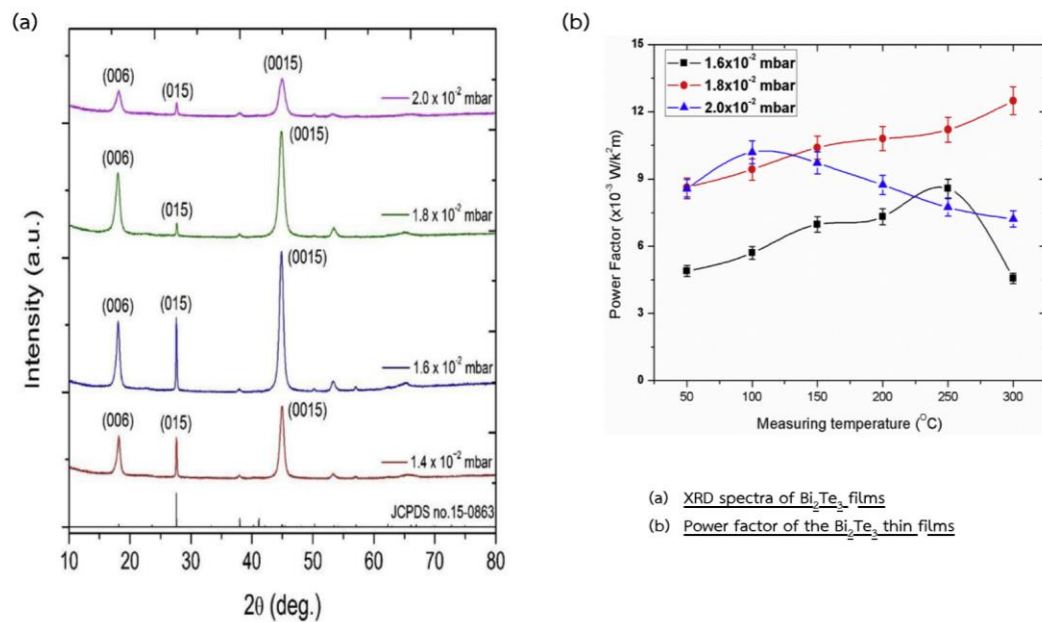


Figure 2.27 Influence of sputtering pressure on (a) structural and (b) power factor of films.

P. Fan et al. [18] study effect of annealing temperature on thermoelectric properties of Sb_2Te_3 thin films deposited by DC magnetron sputtering technique. Effect of annealing temperature can be improved structural of Sb_2Te_3 thin films as show in figure 2.28(a) and improved power of Sb_2Te_3 thin films as show in figure 2.28(b). The best annealing temperature for improve Sb_2Te_3 thin films about 400 °C.

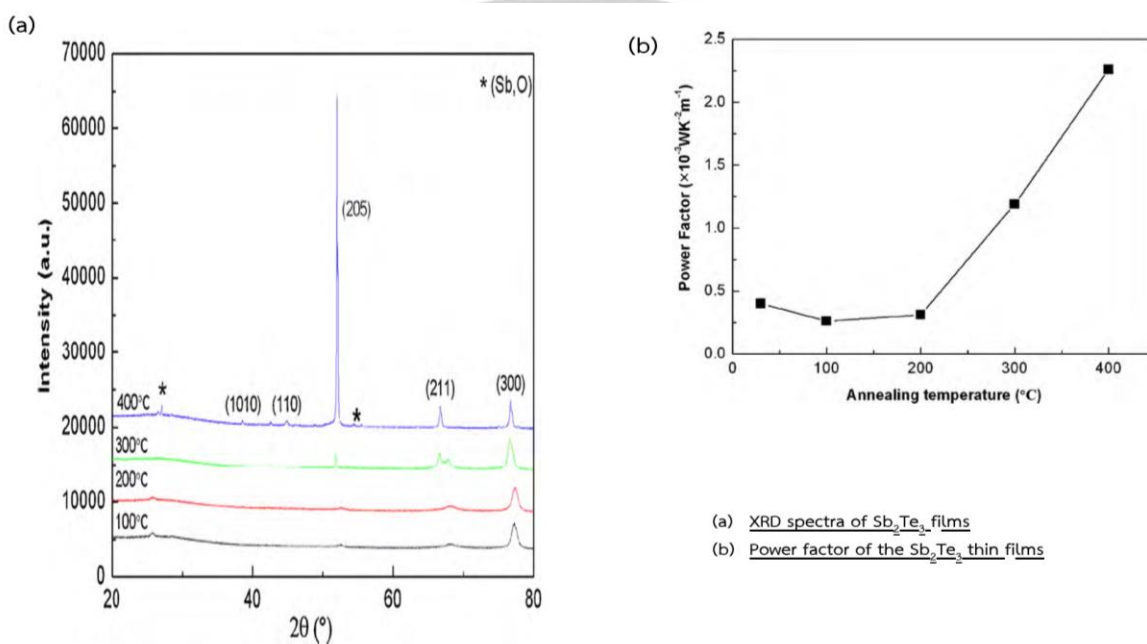


Figure 2.28 Influence of annealing treatment on (a) structural and (b) power factor of films.

Z. Zheng et al. [21] study effect of annealing temperature on thermoelectric properties of Bi_2Te_3 thin films deposited by DC magnetron sputtering technique. Effect of annealing temperature can be improved structural of Bi_2Te_3 thin films as show in figure 2.29(a) and improved power of Bi_2Te_3 thin films as show in figure 2.29(b). The best annealing temperature for improve Bi_2Te_3 thin films about $300\text{ }^\circ\text{C}$.

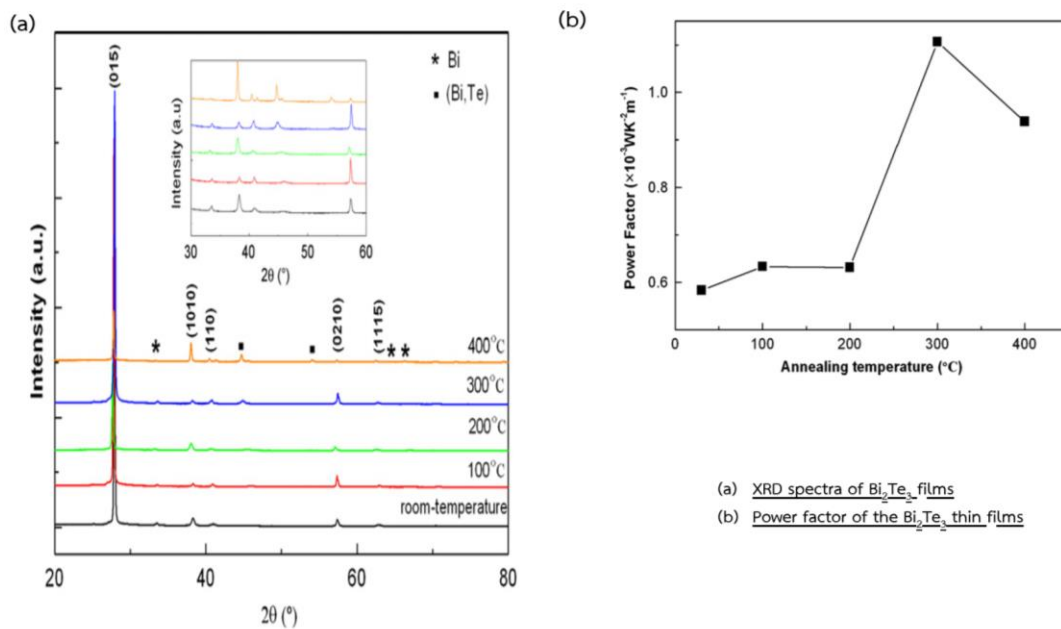


Figure 2.29 Influence of annealing treatment on (a) structural and (b) power factor of films.

L. Francioso et al. [1] study the flexible thermoelectric generators base antimony telluride (p-type) and bismuth telluride (n-type) were fabricated by DC magnetron sputtering and improved thermoelectric properties with annealing process. Design thermocouple leg for best conversion ability from the data of electrical conductivity and thermal conductivity, and measuring open circuit output voltage and output power of the thermoelectric generator from TEG flexible thin films as function of different temperature gradients. The maximum power output about 32 nW.

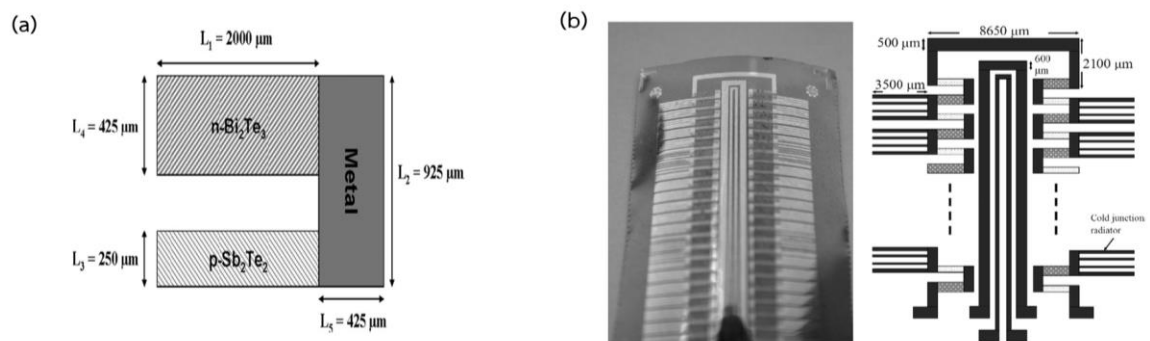


Figure 2.30 show (a) A pair of p-n couple of the device, and parameters that specify the dimension of the device (b) Photograph of fabricated flexible TEG on Kapton HN. and schematic of flexible thermoelectric generator.

In this work, the p-Sb₂Te₃ and n-Bi₂Te₃ film were by DC magnetron sputtering using a single stoichiometric compound target. The influence of annealing treatment on the chemical composition, structural, electrical and thermoelectric properties between p-Sb₂Te₃ and n-Bi₂Te₃ were compared and discussed. The designed thermoelectric generator from the thermoelectric properties of annealed p-Sb₂Te₃ and n-Bi₂Te₃ film were also applied for the fabricate of thermoelectric generator and measurer power output from thermoelectric generator.

Chapter 3

Research methodology

This chapter is to explain the p-Sb₂Te₃ and n-Bi₂Te₃ film were by DC magnetron sputtering using a single stoichiometric compound target. The enhancement on p-Sb₂Te₃ and n-Bi₂Te₃ with annealing treatment. The designed thermoelectric generator from the thermoelectric properties of annealed p-Sb₂Te₃ and n-Bi₂Te₃ film were also applied for the fabricate of thermoelectric generator and measure power output from thermoelectric generator.

3.1 Development of thermoelectric properties of bismuth telluride thick film deposited by DC magnetron sputtering via post-annealing treatment.

3.1.1 Material and equipment

1. 25 μm polyimide film Kapton® Dupont
2. Alloy Bi₂Te₃ target (purity: 99.9%, Stanford Advanced Materials)
3. Microscope slide
4. Aluminum tape
5. Ultrasonic bath
6. Methanol and DI-water
7. Nitrogen gas 99.99%
8. Argon gas 99.99%
9. DC Power Supply
10. Diffusion pump
11. Rotary pump
12. Sputtering chamber
13. Mass flow
14. Water cooling syste
15. Monitoring system
16. DC Power Supply

17. Halogen lamp

18. Thermocouple

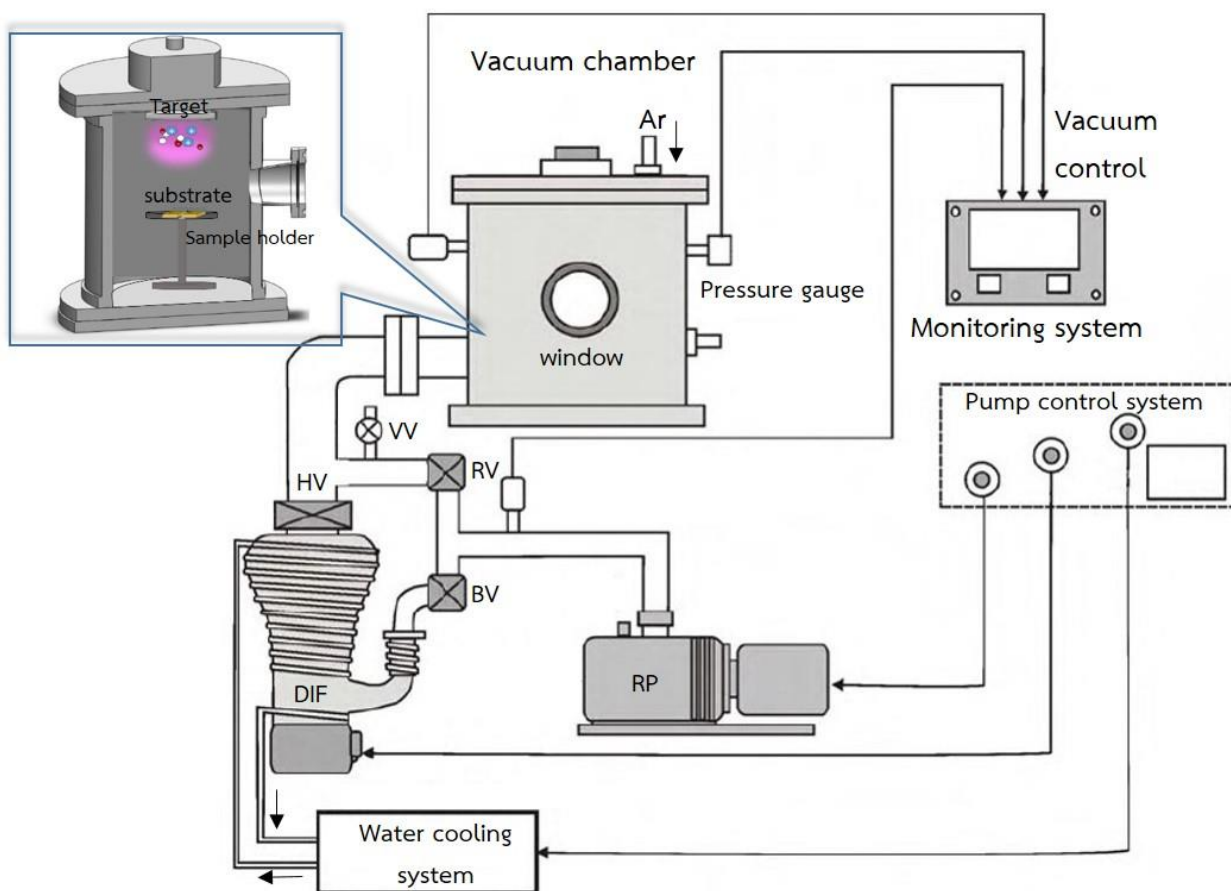


Figure 3.1 Schematic of DC magnetron system

3.1.2 Experimental procedures

Table 3.1 Conditions used for the deposition of Bi_2Te_3 thick films by DC magnetron sputtering with different post-annealing temperature.

Target	Alloy Bi_2Te_3 purity 99.9%
Base pressure	2.5×10^{-5} mbar
Sputtering pressure	1.8×10^{-2} mbar
Sputtering power	45 W
Deposition time	75 min
Post-annealing	150, 250, and 350 °C for 30min

Thick Bi_2Te_3 films were deposited on a polyimide-film substrate by using DC magnetron sputtering from a three-inch-diameter Bi_2Te_3 alloy target of 99.9% impurity. Before sputtering, the polyimide substrates were ultrasonicated in methanol, acetone, and deionized water for 15 minutes and then dried with nitrogen gas. Before deposition, the base pressure in the deposition chamber was 2.5×10^{-5} mbar, and pre-sputtering was done for 5 minutes to remove contamination from the target surface. Before deposition, the substrate was pre-heated to 350 °C for 15 minutes. The DC sputtering power and pressure were maintained at 45 W and 1.8×10^{-2} mbar, respectively, and the sputtering time was fixed at 75 minutes. The films were annealed at 150, 250, and 350 °C under an ambient argon atmosphere for 30 minutes.

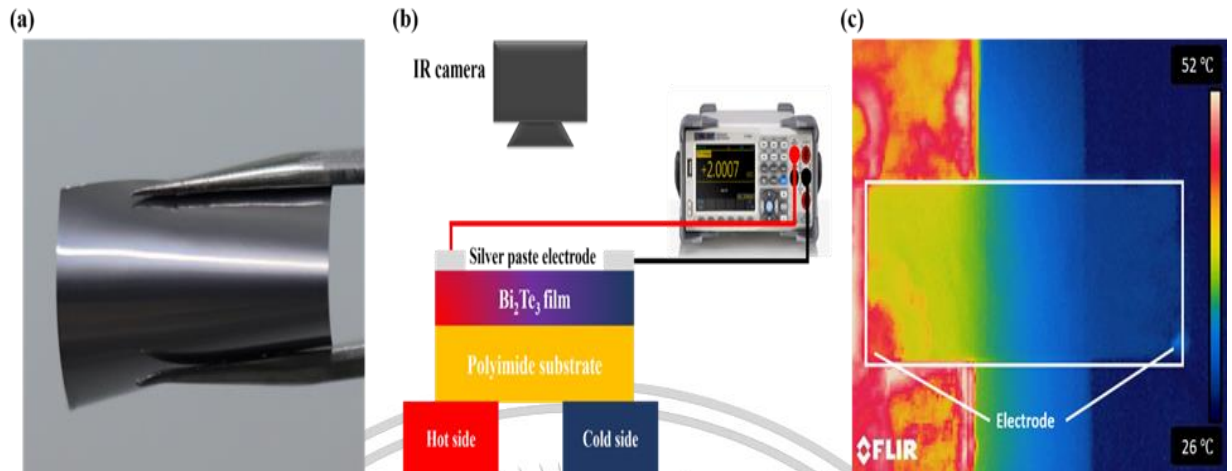


Fig. 3.2 (a) Photograph of thick bismuth telluride film deposited by DC magnetron sputtering on a flexible substrate. (b) Schematic illustration of apparatus for measuring power output from thick, single-leg Bi_2Te_3 film. (c) Infrared top-view image of Bi_2Te_3 film taken during measurement.

Figure 3.2 (a) shows a photograph of a thick Bi_2Te_3 film, which can be flexed without cracking. The thermoelectric power output of thick single-leg Bi_2Te_3 film was measured by using a heater and heat sink to create a temperature gradient and measuring the temperature difference with an infrared camera (FLIR E40) [see Figs. 3.2(b) and 3.2(c)]. The current and voltage produced between two silver-paste electrodes were measured by using a digital multimeter. The output voltage, current, and power produced by the thick single-leg Bi_2Te_3 film were measured at several temperature differences.

3.2 Development of thermoelectric properties of p-Sb₂Te₃ and n-Bi₂Te₃ films deposited by DC magnetron sputtering via post-annealing treatment.

3.2.1 Material and equipment

1. Test chip, Si wafer and 25 μm polyimide film Kapton® Dupont
2. Alloy Sb₂Te₃ and Bi₂Te₃ target (purity: 99.9%, Stanford Advanced Materials)
3. Microscope slide
4. Aluminum tape
5. Ultrasonic bath
6. Methanol and DI-water
7. Nitrogen gas 99.99%
8. Argon gas 99.99%
9. DC Power Supply
10. Diffusion pump
11. Rotary pump
12. Sputtering chamber
13. Mass flow
14. Water cooling system
15. Monitoring system
16. DC Power Supply
17. Halogen lamp
18. Thermocouple

3.2.2 Experimental procedures

The p-Sb₂Te₃ and n-Bi₂Te₃ films were deposited on silicon wafer and test chips by using DC magnetron sputtering technique. High purity Sb₂Te₃ (99.9%) and Bi₂Te₃ (99.9%) 3-inch diameter targets. Sputtering parameters of the p-Sb₂Te₃ and n-Bi₂Te₃ films as show in table 3.2. The chamber vacuum pressure was approximately 2.5×10⁻⁵ mbar. Before deposition process, pre-sputtering was applied for 5 minutes to eliminate contamination and oxide layer on the surface of p-Sb₂Te₃ and n-Bi₂Te₃ alloy targets. The p-Sb₂Te₃ and n-Bi₂Te₃ thin films were deposited at sputtering pressure of 2.6×10⁻² and 1.8×10⁻² mbar respectively. The p-Sb₂Te₃ and n-Bi₂Te₃ were maintained sputtering power at 45 W, and the deposition process time was about 5 minutes. The p-Sb₂Te₃ and n-Bi₂Te₃ thin films were annealed at 200 °C under argon atmosphere for 30 min.

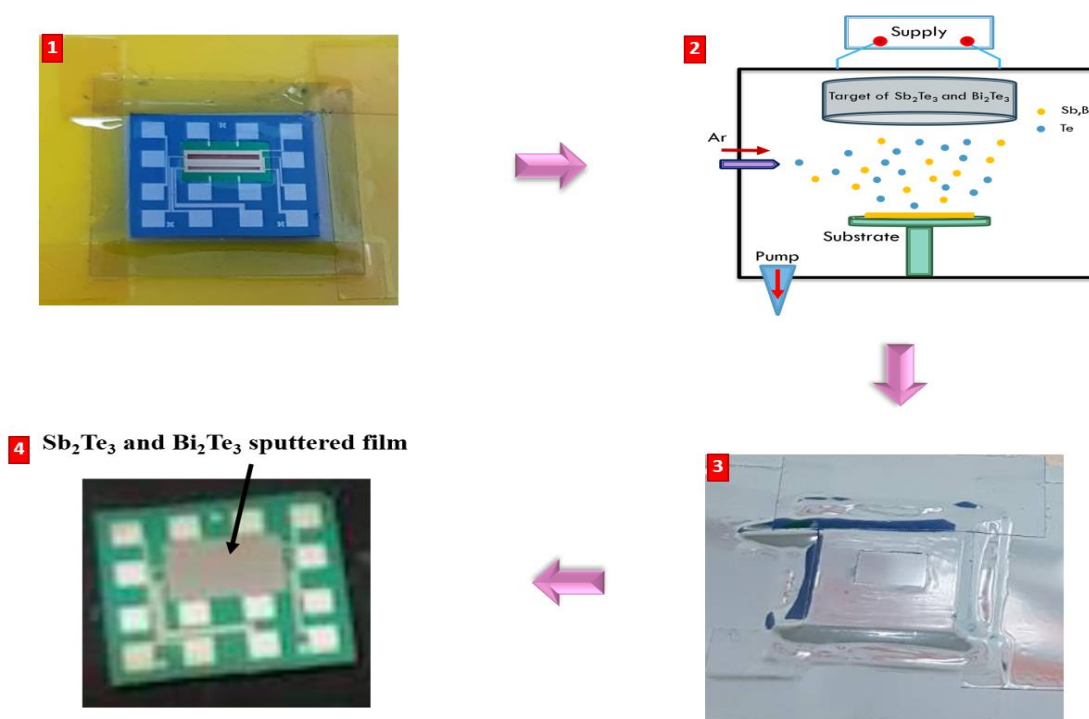


Figure 3.3 Experimental procedures of the preparation of p-Sb₂Te₃ and n-Bi₂Te₃ films via DC magnetron sputtering technique.

3.2.3 Material and equipment

In this study, all equipment is the same as the preparation of p-Sb₂Te₃ and n-Bi₂Te₃ films. The halogen lamp and thermocouple were added into the sputtering system inside the vacuum chamber under the sample holder, as seen in the Figure. 3.4.

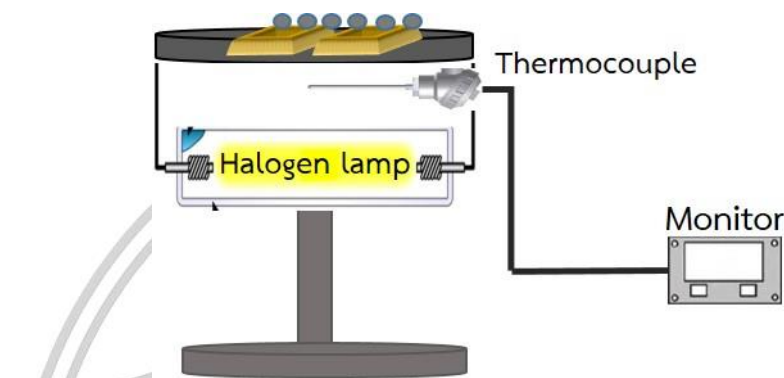


Figure 3.4 Set up heat treatment system in a vacuum chamber

Table 3.2 Conditions used for the deposition of the p-Sb₂Te₃ and n-Bi₂Te₃ films.

Sputtering parameter

Target	Alloy Sb ₂ Te ₃ purity 99.9%	Alloy Bi ₂ Te ₃ purity 99.9%
Base pressure	2.7x10 ⁻⁵ mbar	2.7x10 ⁻⁵ mbar
Sputtering pressure	2.6x10 ⁻² mbar	1.8x10 ⁻² mbar
Sputtering power	45 W	45 W
Deposition time	5 min	5 min
Post-annealing	200 for 30min	200 for 30min

3.3 Design and fabricate thermoelectric generator.

The transformation ability of TEG is depended on electrical conductivity, thermal conductivity, and geometric cross-sectional areas of the thermocouple legs. The geometric cross-sectional areas of the n-type and p-type thermocouple legs can be calculated by [15]

$$\frac{A_n}{A_p} = \sqrt{\frac{K_p \sigma_p}{K_n \sigma_n}} \quad (3.1)$$

Where A_n are geometric cross-sectional areas of the n-type and A_p are geometric cross-sectional areas of the p-type. Using typical material properties given in electrical conductivity and thermal conductivity (see Table 3.3).

Table 3.3 Data for calculate leg area of the p-Sb₂Te₃ and n-Bi₂Te₃ films.

Temperature (K)	Electrical conductivity - Sb ₂ Te ₃ (S/cm)	Electrical conductivity - Bi ₂ Te ₃ (S/cm)	Thermal conductivity - Sb ₂ Te ₃ (S/cm)	Thermal conductivity - Bi ₂ Te ₃ (S/cm)	A _n /A _p
303	226.42	204.43	0.44	0.47	1.018269
318	228.81	207.95	0.45	0.47	1.026397
333	231.23	211.82	0.46	0.47	1.033638
348	233.67	215.88	0.46	0.48	1.018483
363	234.39	220.13	0.47	0.49	1.010604
378	235	224.38	0.48	0.51	0.992836
393	235.47	228.63	0.49	0.52	0.985139
408	236.06	233.05	0.5	0.54	0.968445
423	236.73	237.56	0.51	0.56	0.952645
438	243.99	242.29	0.53	0.58	0.959273
453	252.43	246.85	0.54	0.6	0.959346
468	263.15	251.06	0.56	0.63	0.965243
483	271.47	251.91	0.58	0.67	0.965861
498	278.62	251.12	0.61	0.7	0.983289
513	285.76	250.33	0.63	0.74	0.985822

The thickness of antimony telluride and bismuth telluride at the annealed films approximately $0.9 \mu\text{m}$. From the equation 1 ratio was only determined by the proportionality between width of p-type and n-type. The main geometrical scale was illustrated in Fig. 3.5, and design thermoelectric prototype masks.

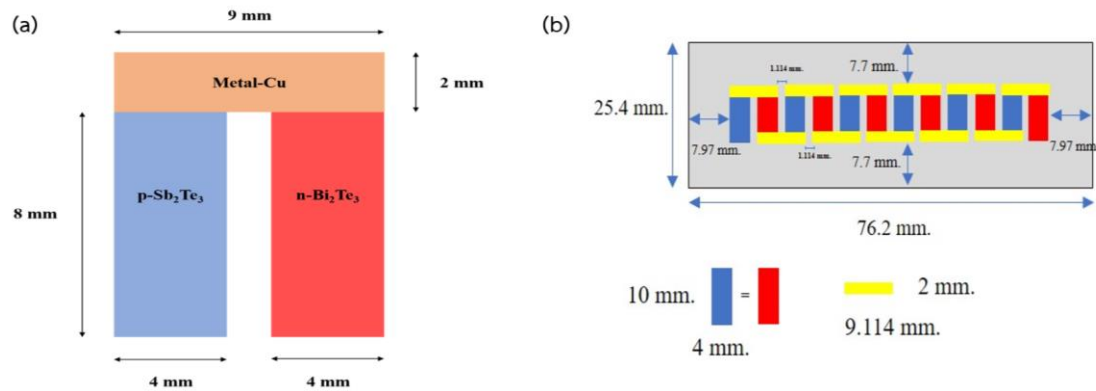


Figure 3.5 (a) The main geometrical scale of the device (b) the prototype of thermoelectric generator.

Figure 3.6 show the fabrication method of the prototype necessary 3 masks, two for Sb_2Te_3 (p-type) and Bi_2Te_3 (n-type) deposition and last one for electrode (Cu). Figure 3.7 show the mask for fabricate thermoelectric generator, mask with sputtered film and sputtered film.

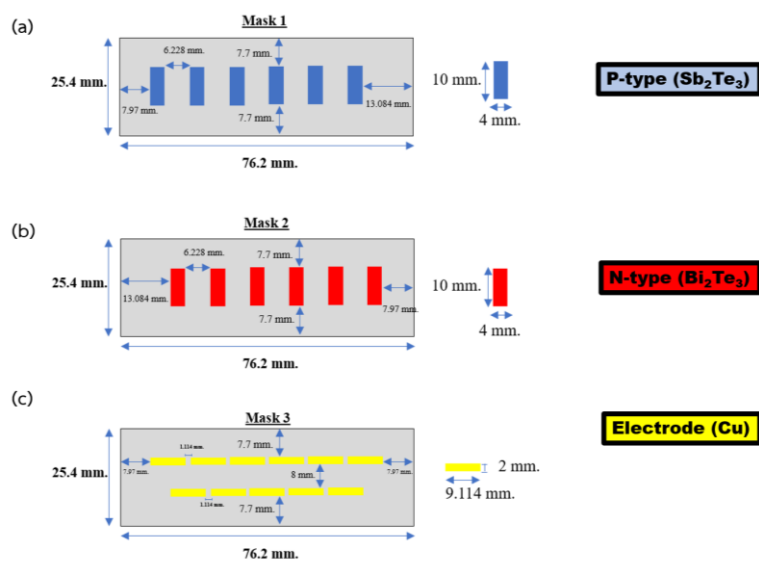


Figure 3.6 the prototype of thermoelectric generator (a) P-type (Sb_2Te_3) (b) N-type (Bi_2Te_3) and (c) Electrode (Cu)

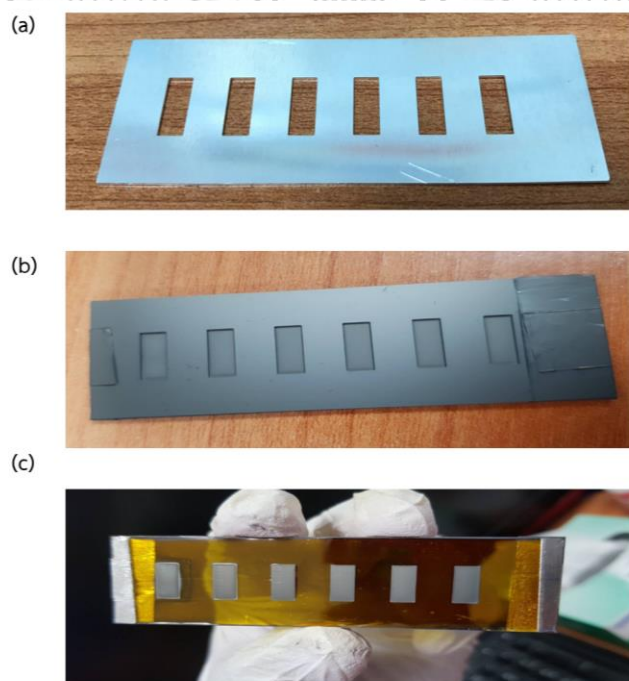


Figure 3.7 (a) The mask for fabricate thermoelectric generator (b) Mask with sputtered film and (c) sputtered film.

The optimum ratio was calculated to be A_n/A_p approximate 1:1. The archived thermoelectric generator has an are approximately $70 \times 18 \text{ mm}^2$ and integrates 6 thermocouples reports a photograph Fig. 3.8.

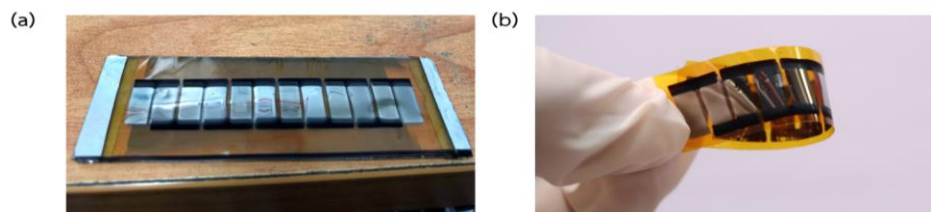


Figure 3.8 Photograph of TEG integrates 6 thermocouples on Kapton substrate.

Figure 3.9 (a) Show the model and (b) photograph of two TEG integrates were connected with silver conductive paint, then at the middle connected with copper tape and graphene sheet for hot side. The cool side that connected with silicone as show in figure 3.10.

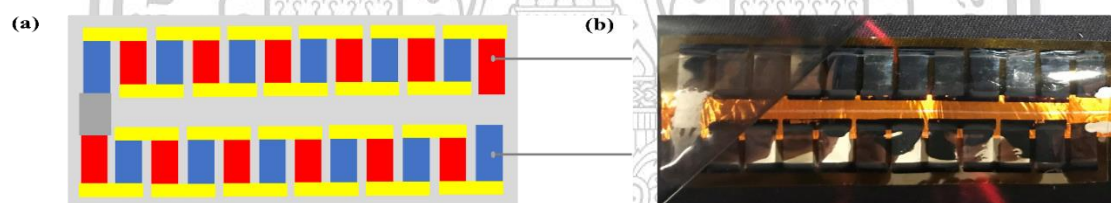


Figure 3.9 (a) Model and (b) photograph of two TEG integrates were connected with silver conductive paint.

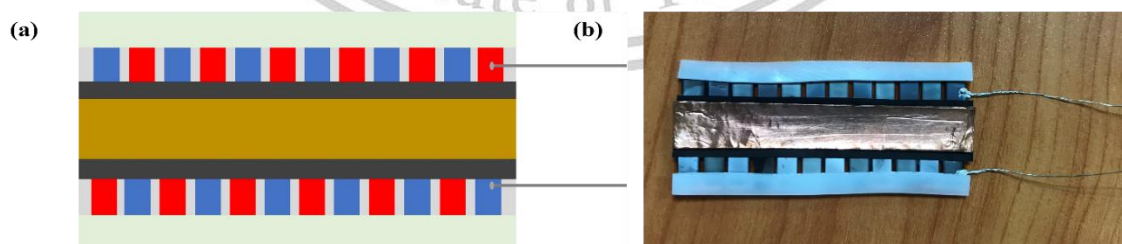


Figure 3.10 (a) Model and (b) photograph of two TEG integrates were connected with Cu tape and graphene sheet (for hot), and silicone (for cool).

3.4 Characterizations

3.4.1 X-ray Diffraction

The crystal structure, including crystal orientation, crystalline size and strain was characterized by X-ray diffraction using a Rigaku diffractometer (Smartlab), as seen in figure 3.11, operated at 40 kV and 20 mA using $\text{Cu-}\kappa_{\alpha}$ radiation. XRD patterns were recorded in the 2θ range of $10\text{-}70^{\circ}$ with a scanning rate of $10^{\circ}/\text{min}$. The XRD system consists of three main parts including the main instrument, computer, cooling system. The measuring the samples are firstly optics set as slits controlled by the SmartLab Studio II software at a computer. After that, the samples were prepared with a dimension 1×1 cm and attached to the center of the sample holder. Places the sample holder into the main instrument and scans. By the sample scanning, qualitative analysis can be done automatically during X-ray diffraction measurement. The XRD patterns were obtained.

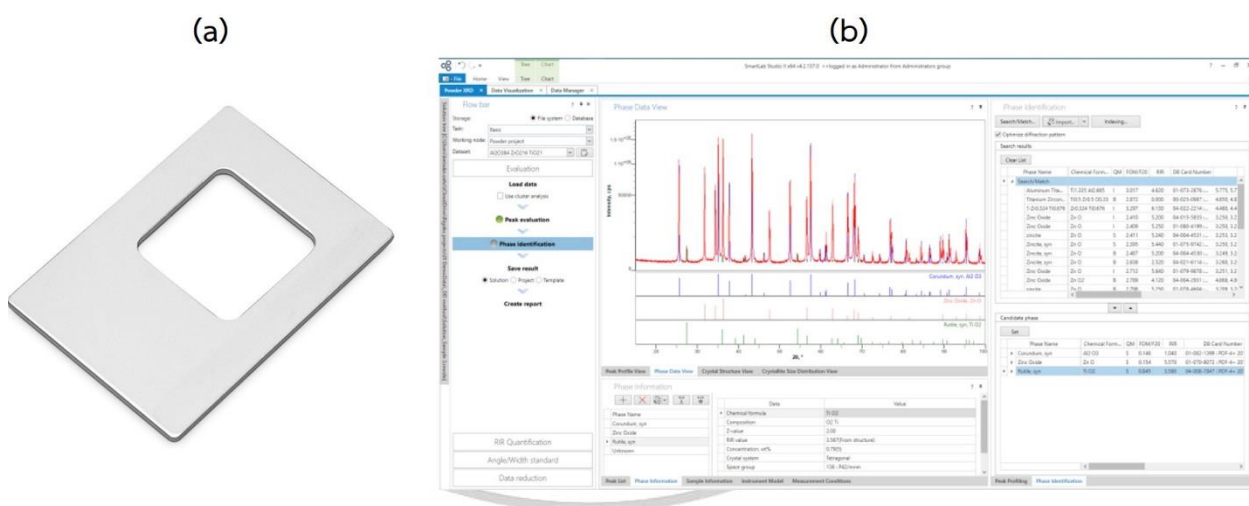


Figure 3.11 (a) Sample holder (b) SmartLab Studio II software.



Figure 3.12 X-ray diffraction (Rigaku diffractometer Smartlab)

3.4.2 Field-emission scanning electron microscopy

The surface morphology and cross-section of the sample material were observed by field-emission scanning electron microscopy (FE-SEM, JSM-7001F) operated at 10 kV. FE-SEM is the electron microscope at high resolution that uses an electron to illuminate the sample operated at the high vacuum. The samples are cut in small pieces and attached the sample to the holder using the carbon tape. And places the sample holder inside the vacuum chamber and pump out the gas. The samples were moved under the electron column and turn on the electron beam to measure the surface morphology of the samples.

The elemental composition was examined by energy-dispersive X-ray spectroscopy (EDX, Oxford Instruments X-Max 20) over a large film area typically three times to obtain the average data. Additionally, EDX is qualitative and quantitative mapping and line scan element analysis.



Figure 3.13 Field-emission scanning electron microscopy (JSM-7001F)

3.4.3 Hall effect measurement.

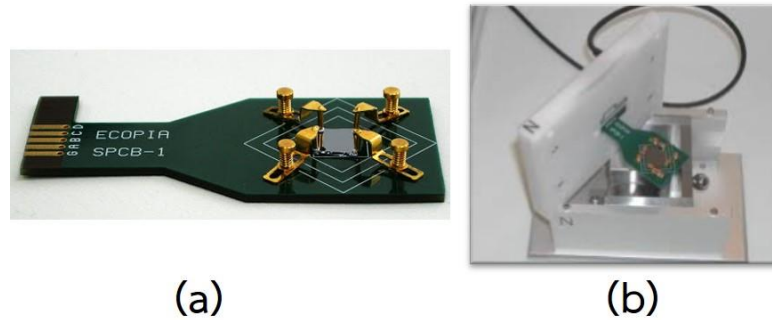


Figure 3.14 (a) hall measurement state (b) sample mounting parts.

The electrical properties and carrier concentration were obtained by Hall effect measurement system at room temperature (Ecopia, HMS-3000) using Van der Pauw configuration. Before Hall measurement, the samples were prepared in dimension of 1x1 cm and attached to the microscope slide. Starting with turns on the Hall system software (HMS-3000) and Swith on the hall system. Places the sample onto the hall measurement state and adjust the four-probe contacts. Put the hall measurement state in the sample mounting parts. Then, input the sample name, IV parameters, record info for the IV curve and save the graph, respectively. Starting hall measurement with a magnetic field of 0.55 Tesla, the software was run and automatically calculated the carrier concentration, the electrical mobility and electrical resistivity of the sample.



Figure 3.15 Hall effect measurement system (Ecopia, HMS-3000).

3.4.4 Seebeck Coefficient/Electrical Resistance Measurement System

The temperature-dependent Seebeck coefficient and electrical conductivity were measured using a ZEM-3 apparatus (ULVAC-RIKO) at 50-300 °C. The ZEM-3 system consists of a computer, the main body of the instrument which contains the power distribution safety, interlock, temperature controller, the power supply and digital multimeter, infrared furnace, vacuum pump and quartz chamber. The sample was cut with a dimension of 3X12 mm. Firstly, slides off the quartz chamber to the left-hand side of the instrument to mount the sample. Take the thermocouple out of the nickel cover which is clamped between upper and lower blocks. Before mounting the sample, the width and depth were measured. After that, opening the clamping block, the sample can be mounted and then

This material is reserved for educational use only, not allowed for commercial use.

Forbidden to modify the content, and cite the document when use.

closing the clamping block. The thermocouple probes are fixed onto the surface of the sample and then the chamber can be closed and pumped. Turn to the measurement software on the computer, input the sample parameters such as sample name, width, depth, probe distance and temperature. Starting the Zem-3 measurement, the measurement system run completes automatically under the helium atmosphere. Finally, analyze the thermoelectric data.

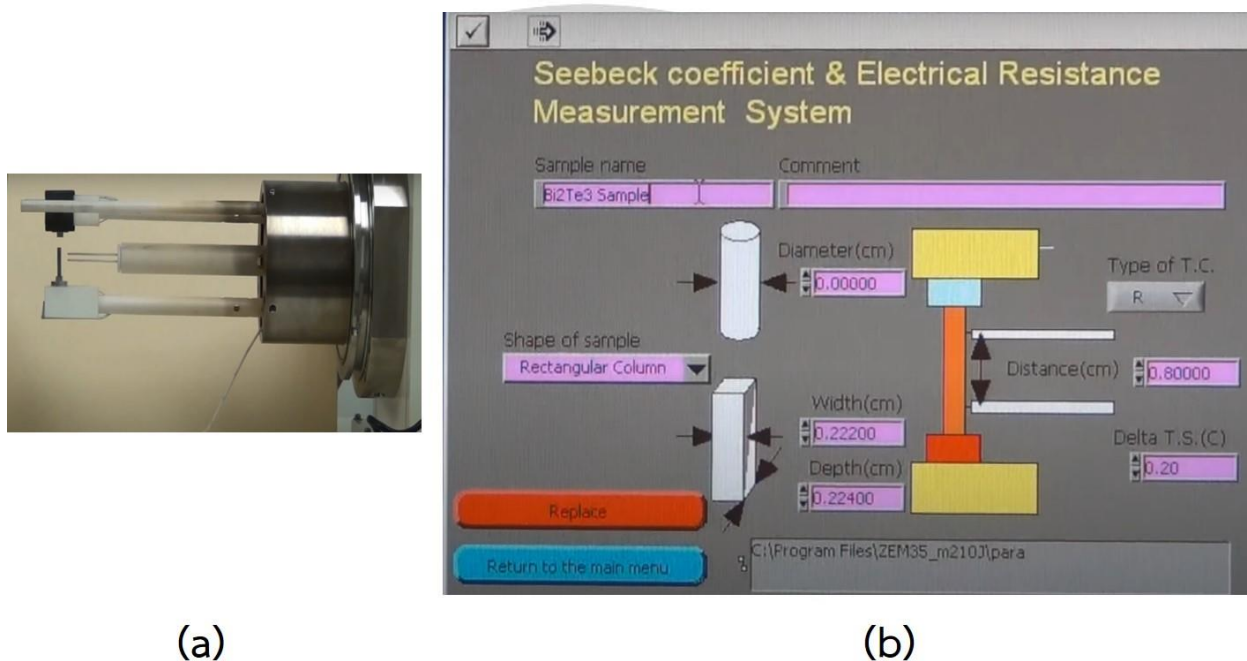


Figure 3.16 (a) sample clamping block (b) Seebeck coefficient and electrical resistance measurement system software (V3.5 for SDC35).

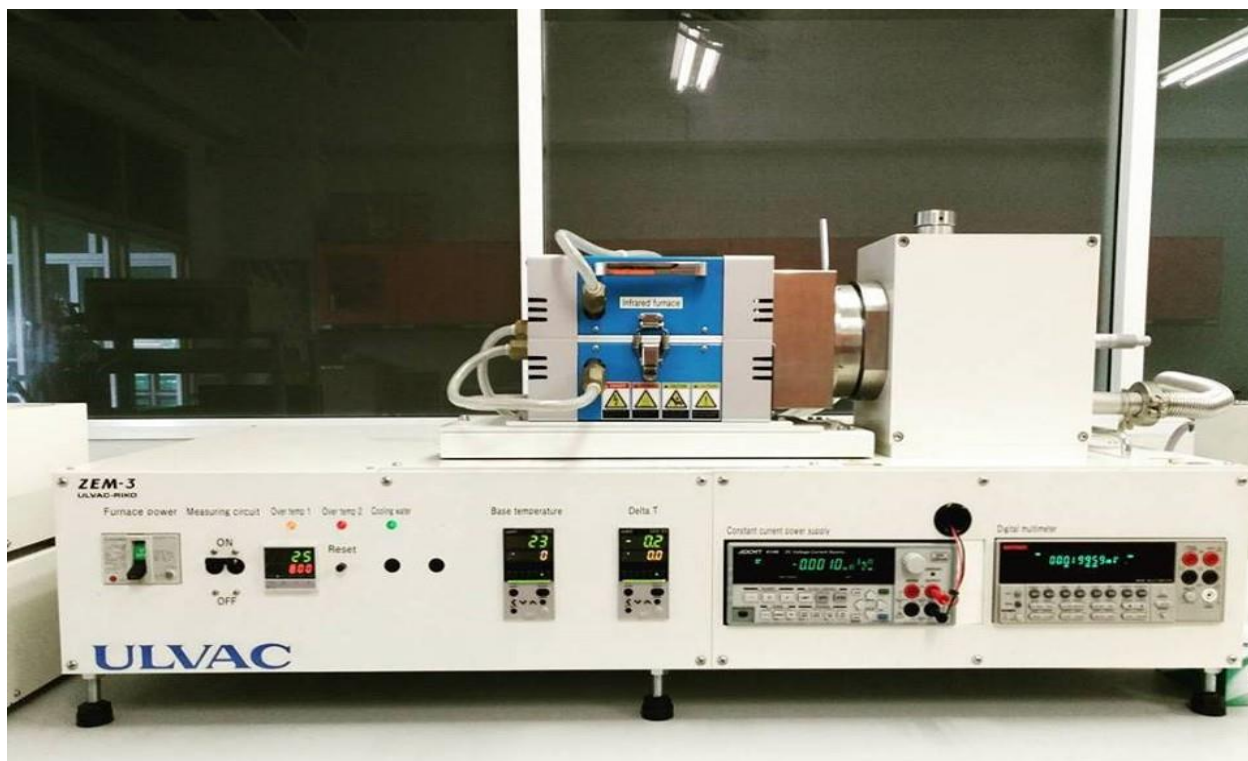


Figure 3.17 Seebeck Coefficient/Electrical Resistance Measurement System (Ulvac RIKO)

3.4.5 Thin Film Analyzer (LINSEIS TFA)

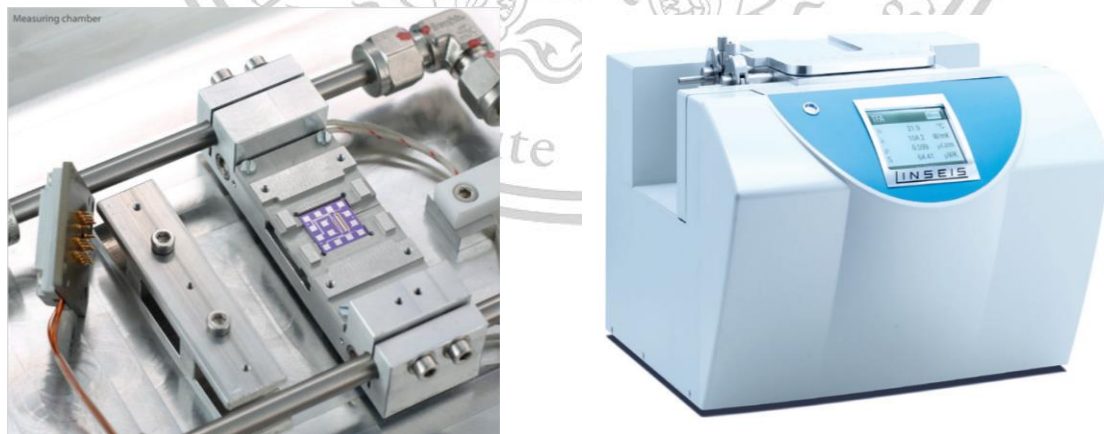


Figure 3.18 Thin Film Analyzer (LINSEIS TFA)

This material is reserved for educational use only, not allowed for commercial use.

Forbidden to modify the content, and cite the document when use.

Figure 3.18 show the Thin Film Analyzer (LINSEIS TFA). The chip is combining the 3 Omega measurement technique for the thermal conductivity measurement with a 4-point Van-der-Pauw setup for the determination of the electrical transport properties as show Figure 3.19 (a) and the chip with shadow mask, before deposition as show Figure 3.19 (b). The Seebeck coefficient can be measured using additional resistance thermometers located near the Van-der-Pauw electrodes. For an easy sample preparation either a strip off foil mask or a metal shadow mask can be used. This configuration allows for a nearly simultaneous characterization of a sample which has been prepared by either PVD (e.g. thermal evaporation, sputtering, MBE), CVD (e.g. ALD), spin coating, drop casting or ink-jet printing in one step and the schematic of test chip for thermoelectric properties (Seebeck coefficient, electrical conductivity and thermal conductivity) measurement as show Figure 3.20.

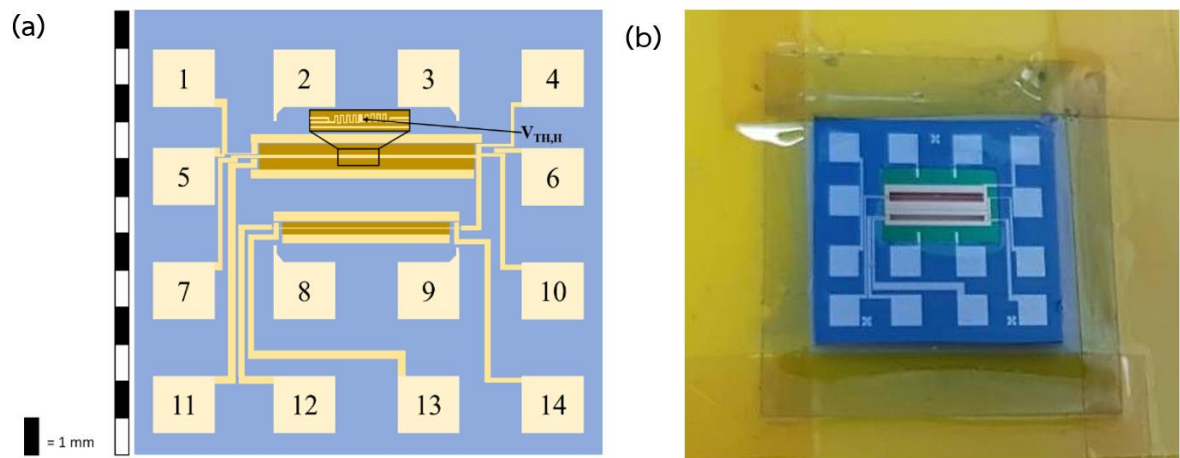


Figure 3.19 (a) Diagram of the chip ZT test structure for Van der Pauw, Seebeck coefficient, and 3ω thermal conductivity measurement, (b) the chip with shadow mask, before deposition

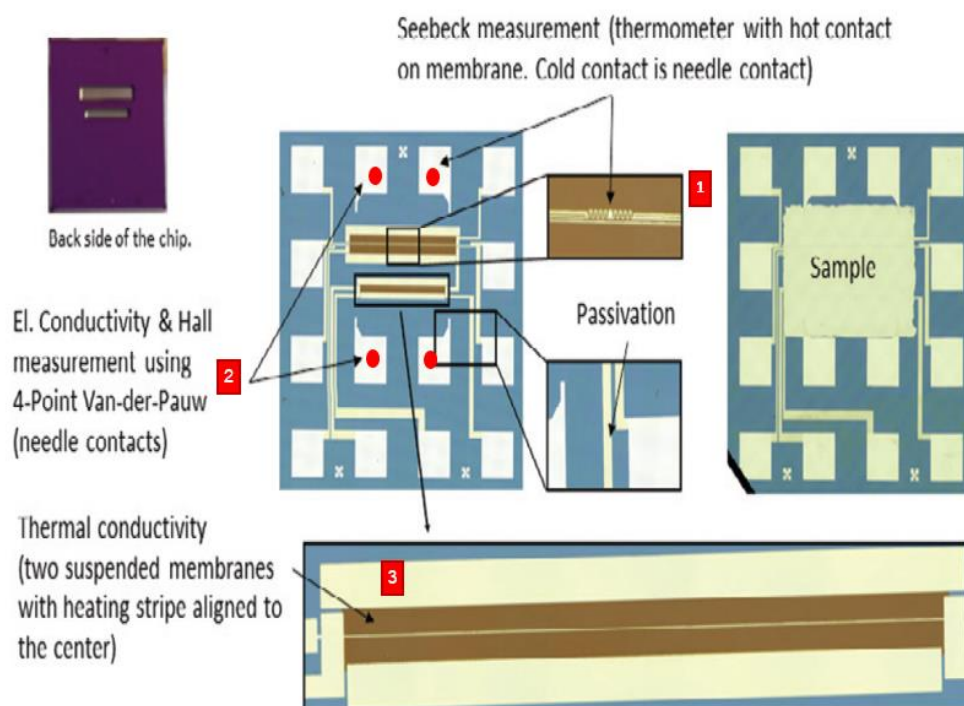


Figure 3.20 The schematic of test chip for thermoelectric properties (Seebeck coefficient, electrical conductivity and thermal conductivity) measurement.

3.4.6 X-Ray Photoemission spectroscopy

(a)



(b)

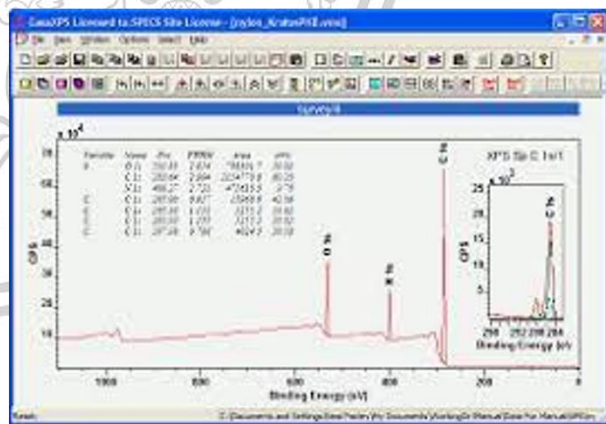


Figure 3.21 (a) samples were prepared in dimension of 1x1 cm and attached to the microscope slide (b) X-Ray Photoemission spectroscopy measurement system software.

The surface chemical properties were obtained by X-Ray Photoemission spectroscopy. Before X-Ray Photoemission spectroscopy measurement, the samples were prepared in dimension of 1x1 cm and attached to the microscope slide as show in Figure 3.21 (a). Figure 3.21 (b) show the X-Ray Photoemission spectroscopy measurement system software. Figure 3.22 show X-Ray Photoemission spectroscopy at Synchrotron Light Research Institute.

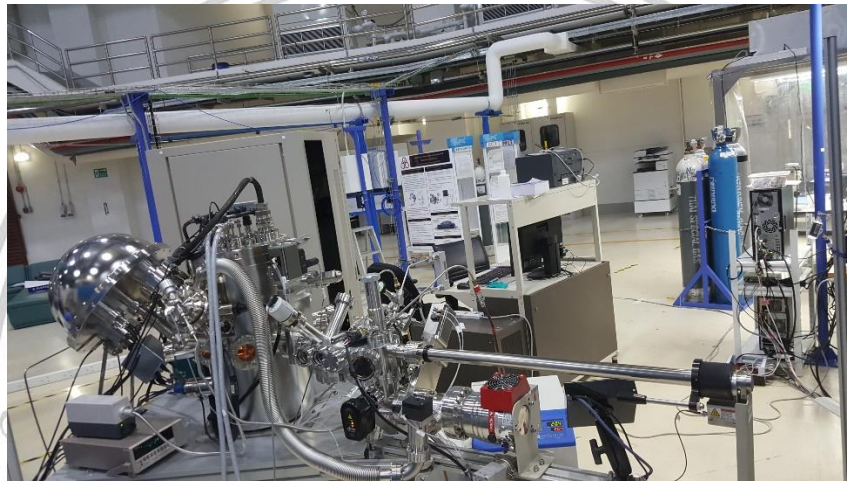


Figure 3.22 X-Ray Photoemission spectroscopy at Synchrotron Light Research Institute.

3.4.7 The measurement thermoelectric generator as functions of different temperature between hot and cold junctions.

The open circuit output voltage and output power of the thermoelectric generator as functions of different temperature between hot and cold junctions. The measurement was used heater (generate heat) and heat sink (cooling) to generate a temperature different and temperature between hot side and cold side was measured by using IR camera (FTIR E40) as show in Figure 3.23 Shot-circuit current (I_{sc}) and open circuit output voltage (V_{oc}) were measured by using digital multimeter (Keithley 2100).

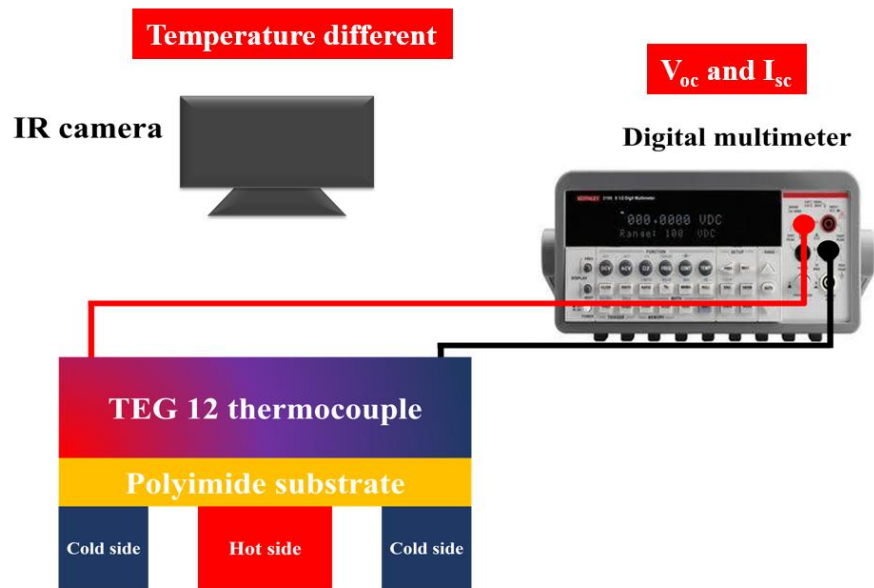
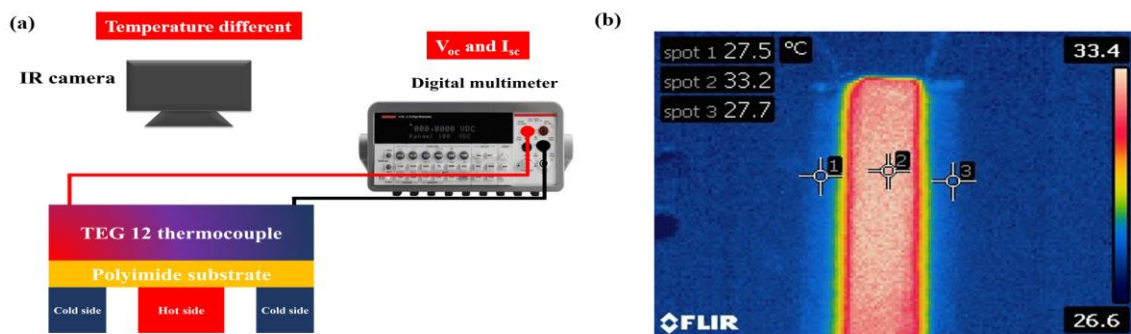


Figure 3.23 Schematic illustration of equipment for measuring open circuit output voltage and output power of the thermoelectric generator from TEG flexible thin films.

Figure 3.24 show the (a) schematic illustration of apparatus for measuring power output and (b) infrared top-view image of thermoelectric module taken during measurement. Infrared top-view image of thermoelectric module taken during measurement and Thermoelectric generator open circuit output voltage (V_{oc}) with body heat human as show in Figure 3.25(a) and 3.25(b).



This material is reserved for educational use only, not allowed for commercial use.

Forbidden to modify the content, and cite the document when use.

Figure 3.24 (a) Schematic illustration of apparatus for measuring power output and (b) Infrared top-view image of thermoelectric module taken during measurement.

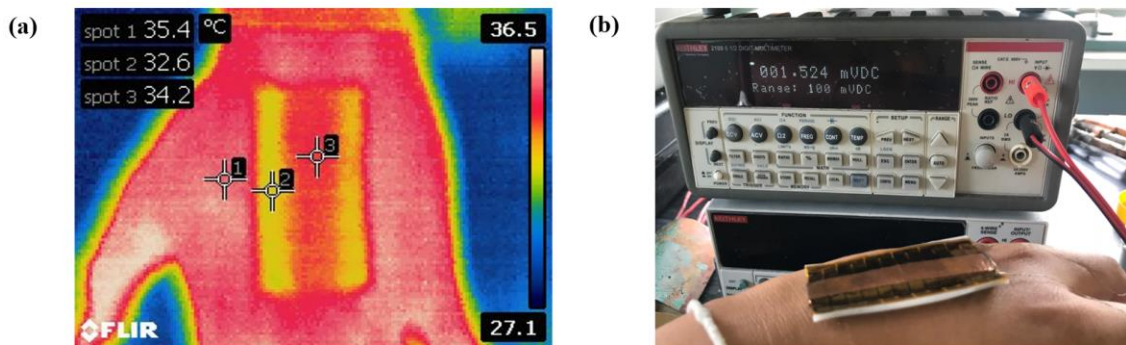


Figure 3.25 (a) Infrared top-view image of thermoelectric module taken during measurement and (b) Thermoelectric generator open circuit output voltage (V_{OC}) with body heat human.

Chapter 4

Result and discussion

4.1 Effect of annealing temperature on thermoelectric properties of bismuth telluride thick film deposited by DC magnetron sputtering.

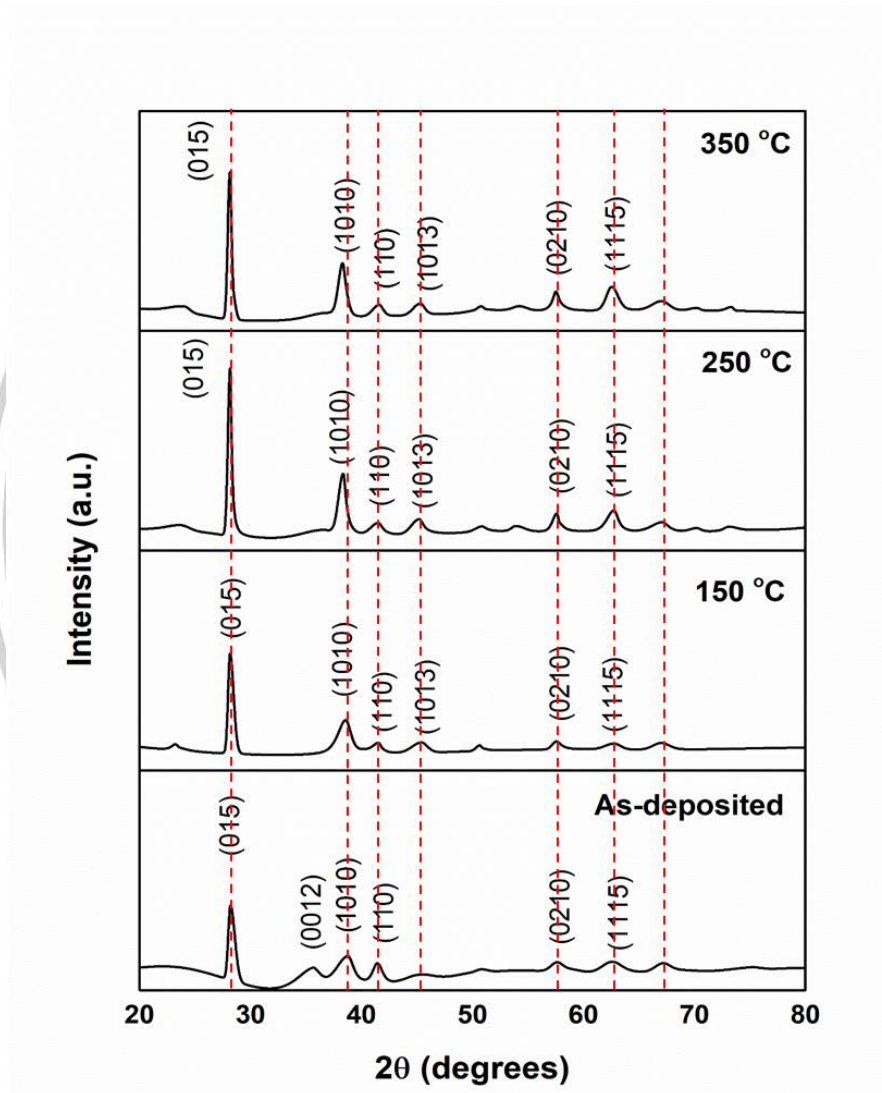


Fig. 4.1 X-ray diffraction patterns from thick Bi_2Te_3 films annealed for 30 minutes at various temperatures.

Figure 4.1 shows XRD patterns of thick Bi_2Te_3 films annealed for 30 minutes at various temperatures. The results reveal that the films are polycrystalline, with a prominent peak at the (015) and (1010) orientation for all samples. On post-annealing treatment, the relative intensity of the diffraction peak (110) slowly decreases, indicating a change in orientation of crystallites with annealing process. In addition, XRD spectra for annealing films at 150 °C, 250 °C and 350 °C, show peak shift towards a lower diffraction angle compared with the as-deposited film. The peak shift increases with higher annealing temperature. It means an expansion of lattice constant corresponding to the annealing temperature. A compressive stress is induced in the bismuth telluride thick films during the annealing treatment because of the different coefficient of thermal expansion between polyimide substrate and bismuth telluride. This result can be indicated by the apparent shift toward lower angle of the diffraction angle [40]. The average grain size of Bi_2Te_3 annealed at the various temperatures was calculated by using the Williamson-Hall formula [41]

$$\beta \cos \theta = \frac{K\lambda}{D} + 4\varepsilon \sin \theta, \quad (4.1)$$

where D is the average grain size, $\lambda = 0.154 \text{ nm}$ is the x-ray wavelength, β is the integral breadth of the diffraction peak, θ is the Bragg diffraction angle, and ε is the microscopic strain.

When the annealing temperature increased to 250 °C, the average grain size increases from 14.5 to 28.9 nm. However, the average grain size of the thick film decreased at 27.4 nm as annealing temperature increased from 350 °C.

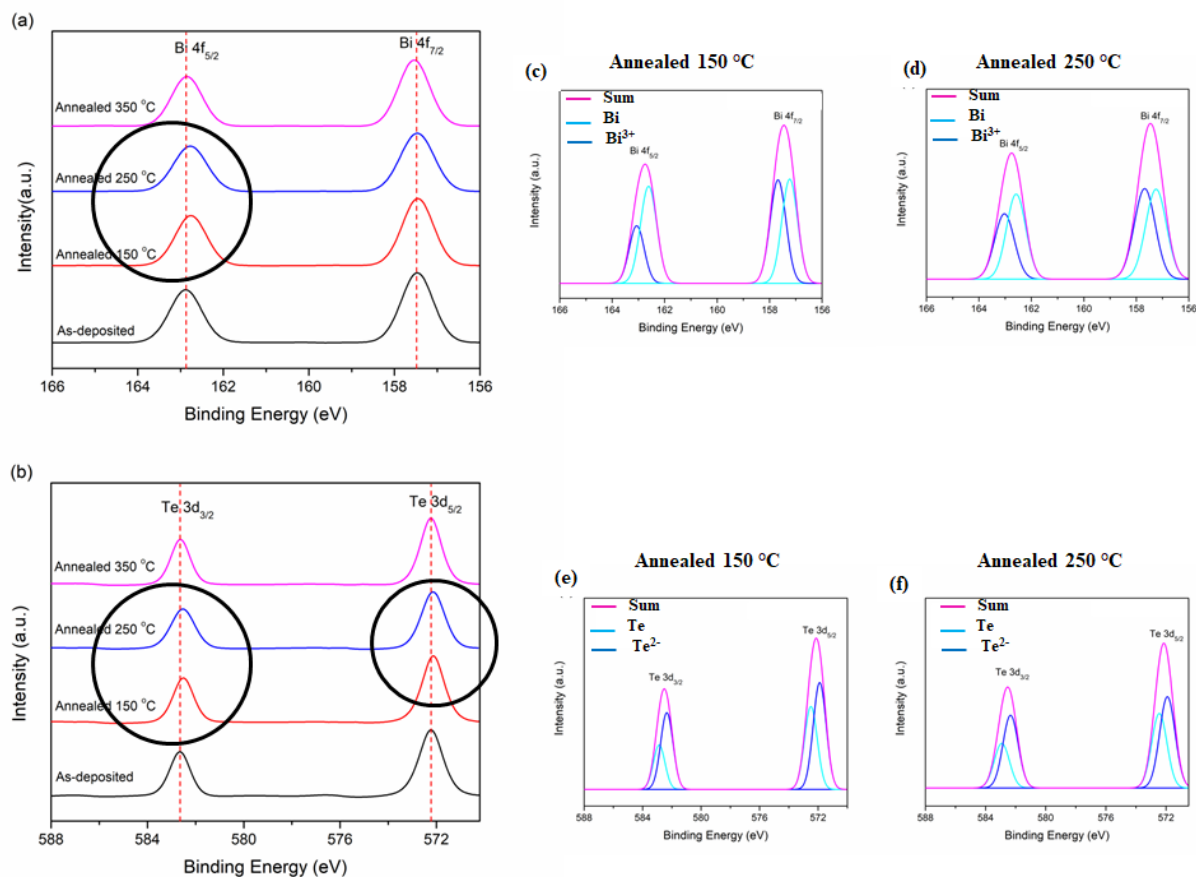


Fig. 4.2 XPS spectra of as-deposited and annealed bismuth telluride thick films. (a) Bi 4f core level with binding energies of 157.5 and 163 eV, corresponds to the states of Bi 4f_{7/2} and 4f_{5/2}. (b) Te 3d core level with binding energies of 572.5 and 583 eV, corresponds to the states of Te 3d_{5/2} and 3d_{3/2}. The inset shows peaks fitting XPS data of Bi 4f_{7/2} and 4f_{5/2} for unbound (Bi) and bound (Bi³⁺) chemical states of annealed films at 150 °C (c) and 250 °C (d), and peaks fitting XPS data of Te 3d_{5/2} and 3d_{3/2} for unbound (Te) and bound (Te²⁻) chemical states of annealed films at 150 °C (e) and 250 °C (f).

The surface chemical composition of the Bi₂Te thick films was analyzed by using x-ray photoelectron spectroscopy (XPS), which especially give information about chemical bonding state on the surface. Figure 4.2 shows the XPS spectra of Bi 4f and Te 3d from

the surface of the as-deposited and annealed Bi_2Te_3 thick films. It was found that Bi 4f core level with binding energies of 157.5 and 163.0 eV, corresponds to the states of Bi 4f_{7/2} and 4f_{5/2} as shown in Fig. 4.2(a). Fig. 4.2(b) shows Te 3d core level with binding energies of 572.5 and 583.0 eV, corresponds to the states of Te 3d_{5/2} and 3d_{3/2} [18]. However, a slightly peak shift is observed toward the lower binding energy side for the annealed films at 150 °C and 250 °C (in the circles). The XPS spectra are resolved into two chemical states of unbound (Bi) and bound (Bi^{3+}) (in the inset of Fig. 4.2(c) and 4.2(d)) and unbound (Te) and bound (Te^{2-}) (in the inset of Fig. 4.2(e) and 4.2(f)). The unbound states of bismuth and telluride peaks (light blue line) have a slight shift (0.2 eV) toward the lower and higher binding from the bound states of bismuth and telluride peaks (blue line), respectively [19]. In annealing processes, it takes energy to break the existing chemical bonds of Bi_2Te_3 . Bi ions (Bi^{3+}) and Te ions (Te^{2-}) resides at the surface with the metallic Bi and Te states. On the other hand, the XPS spectra of thick film annealed at 350 °C did not show significant difference between as-deposited film. We speculate that the metallic Bi and Te migrate from the surface due to high annealing temperature.

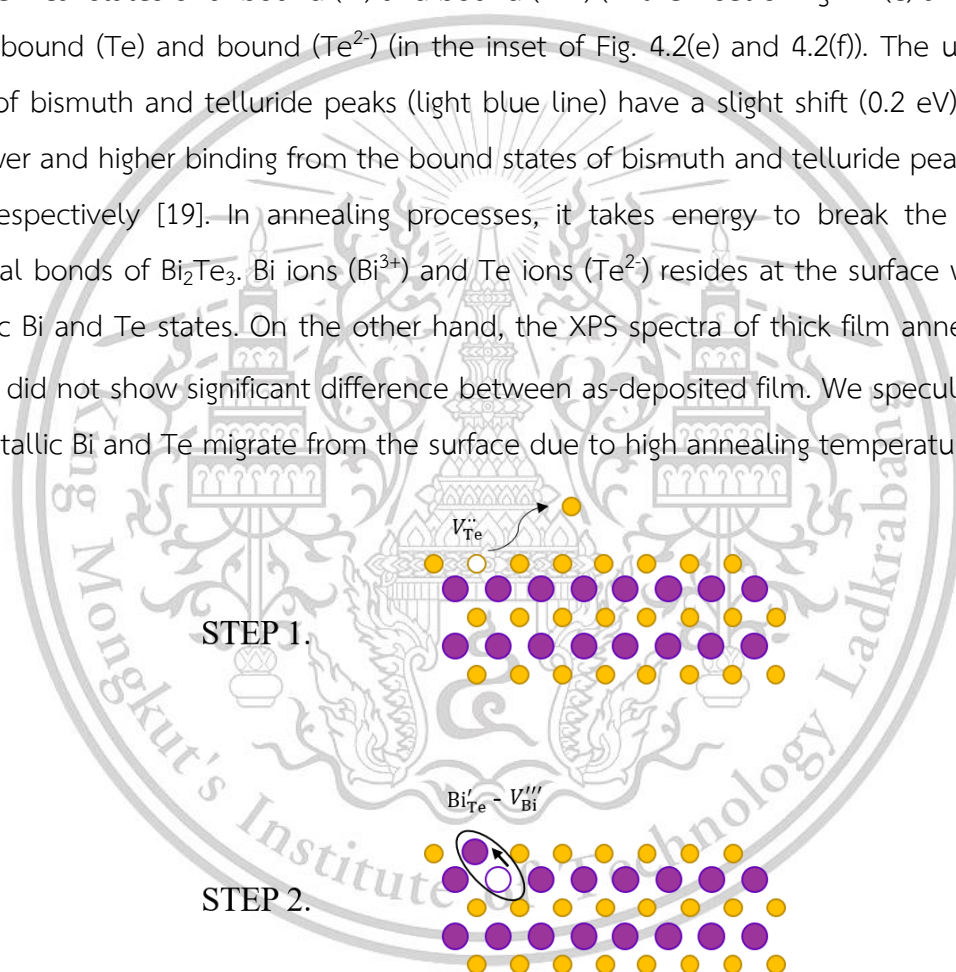
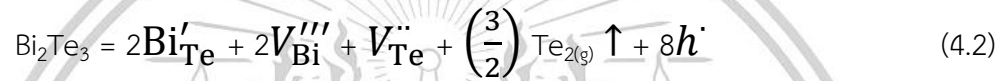


Fig. 4.3 Schematics of defect generation in Bi_2Te_3 atomic structure from the annealing process. In step 1, $V_{\text{Te}}^{\cdot\cdot}$ is formed by the volatile of tellurium atoms on surface. In step 2, a Bi_{Te}^i - $V_{\text{Bi}}^{\prime\prime\prime}$ pair is formed by the migration of bismuth atom from an adjacent Bi site.

The influence of annealing temperature on electronic structure could be explained by the volatile of tellurium atoms during the annealing process. Figure 4.3 shows the schematic model of defect generation in Bi_2Te_3 atomic structure from the annealing process. This model is developed from the J. Kim et. el. work [42]. At typical annealing temperature, the thermal energy that is absorbed to break the bonds in the Bi_2Te_3 structure and then cause the volatile of tellurium atom from surface (20). The volatile of tellurium generates the tellurium vacancies ($V_{\text{Te}}^{\cdot\cdot}$, step 1), where it can be occupied by adjacent bismuth atom. That leads to the generation of the pair of bismuth vacancy ($V_{\text{Bi}}^{\cdot\cdot\cdot}$) and antisite defect (Bi'_{Te}), step 2. This process can be described by equation (4.2) [43]



where h^{\cdot} is the resulting hole and \uparrow indicates the volatilization of tellurium. From Eq. (4.2) the volatile of tellurium generates hole, and the carrier concentration of n-type of Bi_2Te_3 films would be reduced by the compensation of holes. The atomic ratio of bismuth and tellurium may be estimated by using equation (4.3)

$$\frac{\rho_{\text{Te}}}{\rho_{\text{Bi}}} = \frac{I_{\text{Te}}/S_{\text{Te}}}{I_{\text{Bi}}/S_{\text{Bi}}} \quad (4.3)$$

where ρ , I , and S are the atom density, integrated intensity, and the atomic sensitivity factor, respectively. This incorporates the calculated Bi $4f_{7/2}$ and Te $3d_{5/2}$ areas with $S_{\text{Bi}}=2.9$ and $S_{\text{Te}}=4.9$ for surface atoms [44]. Table 4.1 lists the calculated Te content of thick Bi_2Te_3 films annealed at different temperatures. The tellurium content decreases from 59.02 to 57.38 as the annealing temperature increases from 150 to 350 °C. This result indicates that elemental tellurium evaporates during annealing. The evaporation is attributed to the inequivalent atomic bonds at the surface of the annealed films, which is essential for the evaporation of elemental tellurium [20].

Table 4.1 Calculated average grain size and Te content of thick Bi_2Te_3 films annealed at different temperatures.

Annealing temperature (°C)	$\beta\cos\theta$	Average grain size [D (nm)]	Te content (%)
As-deposited	0.0097	14.5	59.02
150	0.0083	23.8	58.79
250	0.0060	28.9	58.36
350	0.0063	27.4	57.38

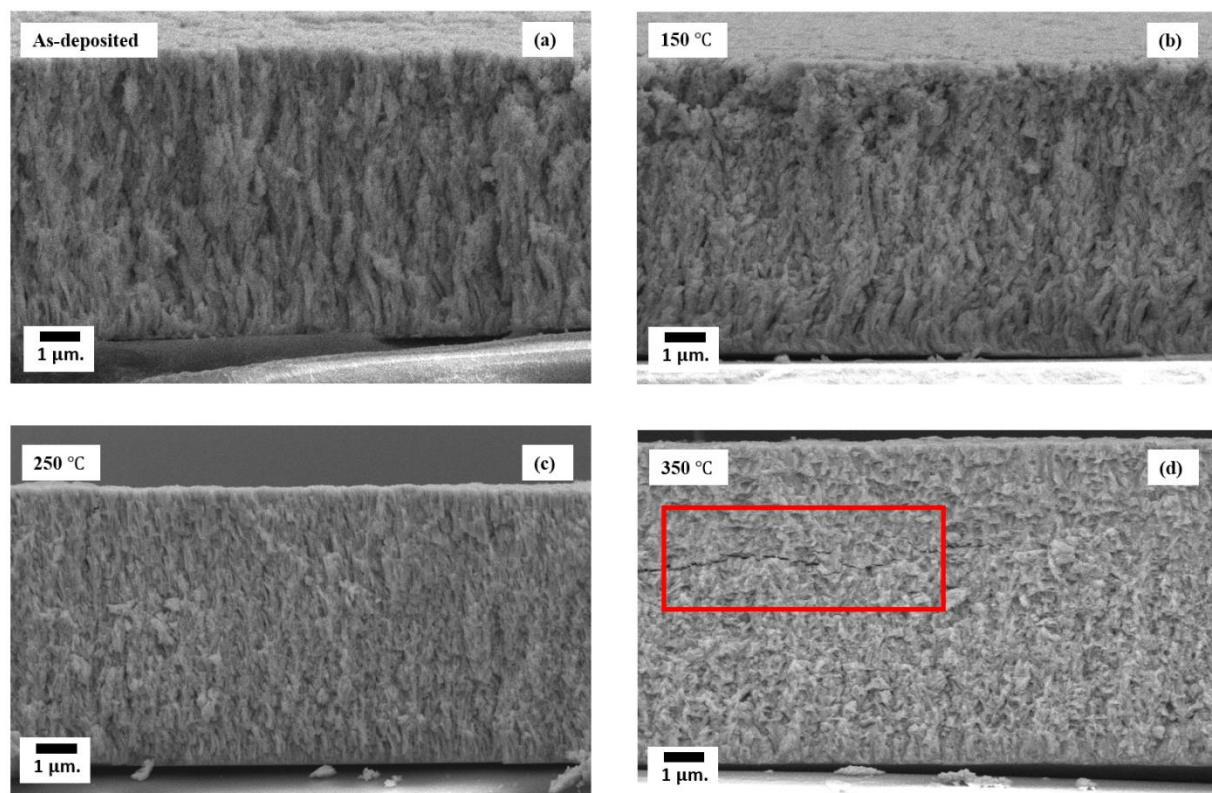


Fig. 4.4 Cross section of thick Bi_2Te_3 films (a) as-deposited and annealed at (b) 150 °C, (c) 250 °C, and (d) 350 °C.

Figure 4.4 shows a cross section of the as-deposited and annealed Bi_2Te_3 films. The film is about 10 μm thick and remains almost unchanged after annealing. As the annealing temperature increases from 150 to 250 $^\circ\text{C}$ [Figs. 4.4(b) and 4.4(c)], the crystallization and agglomeration of the thick films improve as the films begin to grow in from a column structure, confirming that the crystallization can be improved by annealing. However, Fig. 4.4 (d) reveals a crack in the columnar film after annealing at 350 $^\circ\text{C}$. The micro-cracks appeared at 350 $^\circ\text{C}$ is caused from the different coefficient of thermal expansion between polyimide substrate ($2.0 \times 10^{-5} \text{ K}^{-1}$) [45] and bismuth telluride ($5.08 \times 10^{-5} \text{ K}^{-1}$) [24]. A compressive stress is induced in the bismuth telluride thick films during the annealing treatment. This result can be indicated by the apparent shift toward lower angle of the diffraction angle. At typical annealing temperature (350 $^\circ\text{C}$), the compressive stress inside the film is large enough, which can initiate the micro-crack growth [16]. These results indicate that the film crack degrades the crystalline structure of the film, which is consistent with the XRD spectra (cf. Fig. 4.1; the peak decreases after annealing at 350 $^\circ\text{C}$). In addition, the average grain size (see Table 4.1) decreases from 28.9 to 27.4 nm.

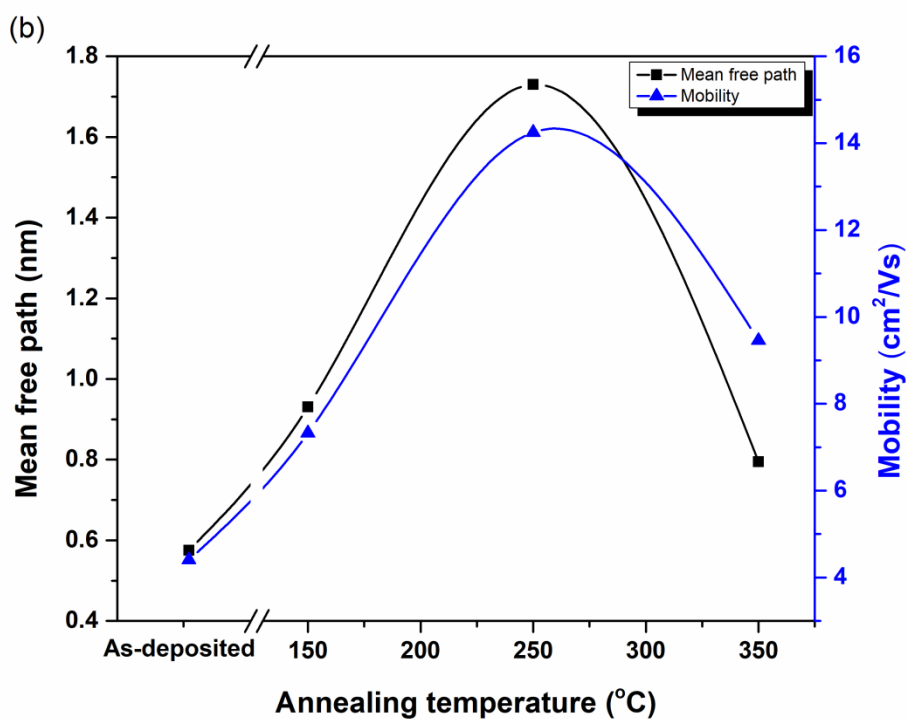
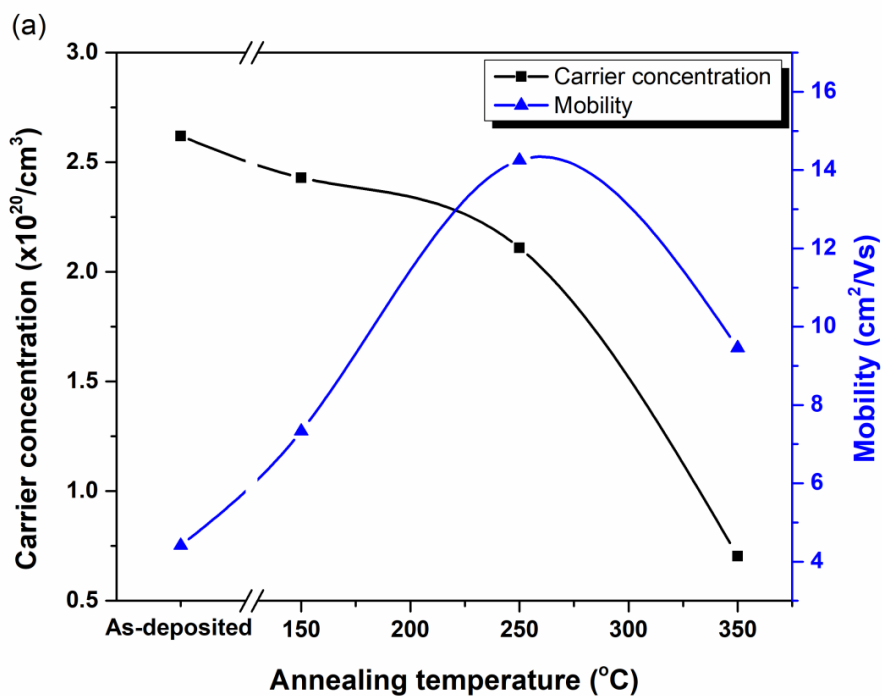


Fig. 4.5 (a) Carrier concentration and mobility; (b) mean free path and mobility of thick Bi_2Te_3 films annealed at different temperatures.

Figure 4.5(a) shows how annealing affects the room-temperature carrier concentration and mobility of the Bi_2Te_3 films. All films have a negative carrier concentration because they are n-type semiconductors; the carrier concentration of the film decreases from 2.62×10^{20} to $0.7 \times 10^{20} \text{ cm}^{-3}$ when annealing at $350 \text{ }^\circ\text{C}$. The decrease in carrier concentration with annealing temperature is attributed to the evaporation of tellurium, which creates tellurium vacancies ($V_{\text{Te}}^{\cdot\cdot}$). Next, the antisite defect (Bi'_{Te}) and the bismuth vacancy ($V_{\text{Bi}}^{\prime\prime\prime}$) become involved as bismuth enters the tellurium vacancies as shown in equation (4.2). In addition, the mobility increases from 4.4 to $14.2 \text{ cm}^2 \text{ V}^{-1} \text{ s}^{-1}$ as the annealing temperature increases to $250 \text{ }^\circ\text{C}$. The increase in average grain size (see Table 4.1) decreases the grain-boundary intensity and reduces carrier scattering at the grain boundaries. However, the mobility decreases to $9.46 \text{ cm}^2 \text{ V}^{-1} \text{ s}^{-1}$ upon increasing the annealing temperature to $350 \text{ }^\circ\text{C}$ because the crystallization is degraded by the crack in the film [see Fig. 4.4(d)]. Figure 4.5(b) shows the mean free path and mobility of the Bi_2Te_3 thick films. The carrier mean free path l can be calculated by using [25]

$$l = \frac{h}{2e} \left(\frac{3n}{\pi} \right)^{\frac{1}{3}} \mu \quad (4.4)$$

where h and $e > 0$ are Planck's constant and the fundamental charge, respectively. Equation (4.4) indicates that the mean free path is related to carrier concentration and mobility. The mean free path of thick films increases from 0.57 to 1.73 nm as the annealing temperature increases to $250 \text{ }^\circ\text{C}$ and decreases to 0.79 nm as the annealing temperature rises from 250 to $350 \text{ }^\circ\text{C}$. The transfer of carriers is involved by grain size and grain boundary preceding to increase of mobility. The decrease in the mean free path is confirmed by the crack in the film annealed at $350 \text{ }^\circ\text{C}$, which is due to resistance to carrier scattering.

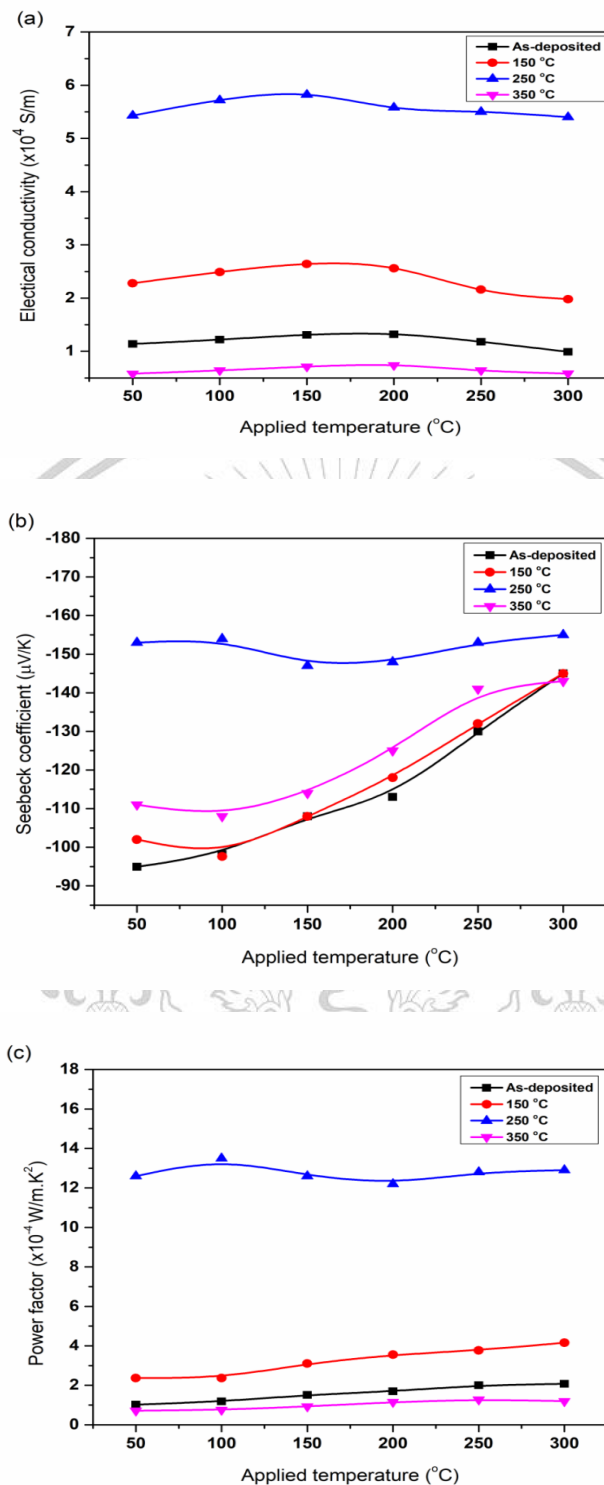


Fig. 4.6 (a) Electrical conductivity, (b) Seebeck coefficient, and (c) power factor as functions of applied temperature for thick Bi_2Te_3 films annealed at different temperatures.

Figures 4.6(a)–4.6(c) show the electrical conductivity, Seebeck coefficient, and power factor, respectively, as a function of temperature for thick Bi_2Te_3 films annealed at different temperatures. Figure 4.6(a) shows that, for all conditions, the electrical conductivity increases from 50 to 150 °C and then decreases with temperature. The electrical conductivity ranges from 0.99×10^4 to 1.32×10^4 S/m in as-deposited film and increases to 5.4×10^4 to 5.82×10^4 S/m in film annealed at 250 °C. The low electrical conductivity in as-deposited film is due to the low mobility and low crystallinity. Upon annealing the thick Bi_2Te_3 films, the crystallinity and mobility increases, which improves the electrical conductivity. However, the lowest electrical conductivity occurs in the film annealed at 350 °C (0.58×10^4 to 0.73×10^4 S/m), which may be attributed to low carrier concentration due to the volatilization of tellurium and the decreased mobility due to the cracked film annealed at 350 °C.

As shown in Fig. 4.6(b), the Seebeck coefficient of all Bi_2Te_3 films is negative, indicating that they are n-type semiconductors. The Seebeck coefficient ranges from -97 to -145 $\mu\text{V}/\text{K}$ in as-deposited film and increases to -147 to -155 $\mu\text{V}/\text{K}$ in film annealed at 250 °C, then decreases to -108 to -143 $\mu\text{V}/\text{K}$ in film annealed at 350 °C. Therefore, the thick Bi_2Te_3 film has a maximum Seebeck coefficient when annealed at 250 °C. The greater Seebeck coefficient in films annealed below 350 °C is due to the decrease in carrier concentration from 2.62×10^{20} to 2.11×10^{20} cm^{-3} [see Fig. 4.6(a)], which in turn is due to the reduced number of donor defects [26]. The Seebeck coefficient for a degenerate semiconductor is given by [15]

$$S = \frac{8\pi^2 k_B^2}{3eh^2} m^* T \left(\frac{\pi}{3n} \right)^{\frac{2}{3}} (1 + R) \quad (4.5)$$

where k_B is Boltzmann's constant, h is Planck's constant, m^* is the effective carrier mass, n is the carrier concentration, T is absolute temperature, and R is the scattering function. Equation (4.5) implies that the Seebeck coefficient is directly proportional to the measurement temperature and inversely proportional to carrier concentration. However, the Seebeck coefficient for a thick film annealed at 350 °C decreases because the carrier mean free path decreases [as shown in Fig. 4.5(b)], and the mean free path explains the

degree of carrier scattering at defects in a grain. The increase in scattering decreases the mean free path, which decreases the Seebeck coefficient [27].

The thermoelectric power factor of thick Bi_2Te_3 films annealed at different temperatures was calculated by using the Seebeck coefficient and the electrical conductivity ($S^2\sigma$), with the result shown in Fig. 4.6(c). These results indicate that the power factor increases with annealing temperature up to 250 °C, then decreases as the annealing temperature increases further. The maximum power factor is $13.5 \times 10^{-4} \text{ W K}^{-2} \text{ m}^{-1}$, which occurs at the annealing temperature of 250 °C.

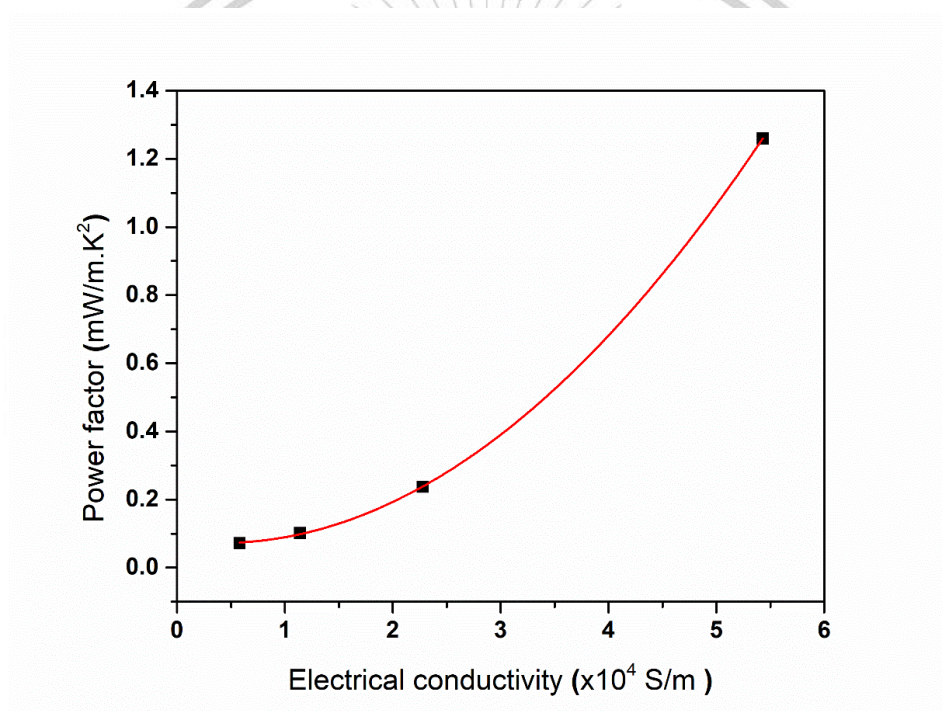


Fig. 4.7 Power factor as a function of electrical conductivity for thick Bi_2Te_3 films annealed at different temperatures.

Figure 4.7 shows the power factor as a function of electrical conductivity for thick Bi_2Te_3 films. The increased electrical conductivity is attributed mainly to the improved crystallinity and the increase in carrier mobility upon annealing. The maximum power factor occurs at the maximum electrical conductivity, which is obtained at the annealing temperature of 250 °C. Thus, the power factor of thick Bi_2Te_3 films improves significantly with respect to the electrical conductivity. Table 4.2 compares the thermoelectric

properties of thick Bi_2Te_3 films deposited by room-temperature DC magnetron sputtering with dispenser printing [28], co-evaporation [29], screen-printing [9], and thermally assisted sputtering [30]. The power factor for Bi_2Te_3 deposited by DC magnetron sputtering and annealed at $250\text{ }^\circ\text{C}$ is comparable to that obtained with various other deposition techniques for thick Bi_2Te_3 film.

Table 4.2 Room-temperature power factor of thick Bi_2Te_3 films deposited by various techniques.

Deposition technique	Electrical conductivity (S/cm)	Seebeck coefficient ($\mu\text{V}/\text{K}$)	Power factor ($\text{mW K}^{-2} \text{m}^{-1}$)	Treatment process
Dispenser printing [46]	22	-230	0.12	Curing treatment at $350\text{ }^\circ\text{C}$
Co-evaporation [47]	363	-202	1.5	Substrate temperature $250\text{ }^\circ\text{C}$
Screen-printing [48]			2.1	Annealing treatment at $250\text{ }^\circ\text{C}$ (Bi and Te powders ambient)
Thermally Assisted Sputtering Method [30]	500	-150	1.12	-
DC sputtering (this work)	502	-155	1.21	Annealing treatment at $250\text{ }^\circ\text{C}$ (argon atmosphere)

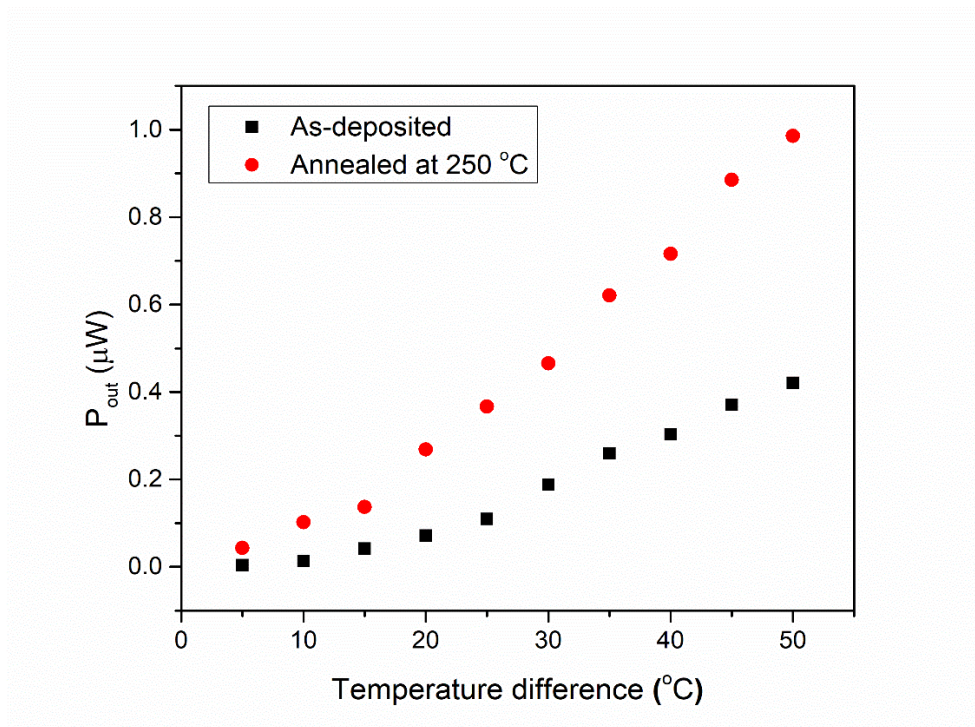


Fig. 4.8 Power output of single-leg, thick, thermoelectric Bi_2Te_3 film as a function of temperature difference for as-deposited film and film annealed at 250 °C.

Figure 4.8 shows the power output of single-leg, thick, thermoelectric Bi_2Te_3 film as a function of temperature difference ($\Delta T = 5\text{--}50\text{ }^\circ\text{C}$). The as-deposited film generates a power output of 3.78 nW at $\Delta T = 5\text{ }^\circ\text{C}$ and 0.42 μW at $\Delta T = 50\text{ }^\circ\text{C}$. The annealed film at 250 °C generates an output power of 43.24 nW at $\Delta T = 5\text{ }^\circ\text{C}$ and 0.98 μW at $\Delta T = 50\text{ }^\circ\text{C}$. This result indicates that annealing improves the output power of single-leg, thick, thermoelectric Bi_2Te_3 film.

4.2 Comparison of the thermoelectric properties of Bi_2Te_3 and Sb_2Te_3 films deposited via the DC magnetron sputtering technique.

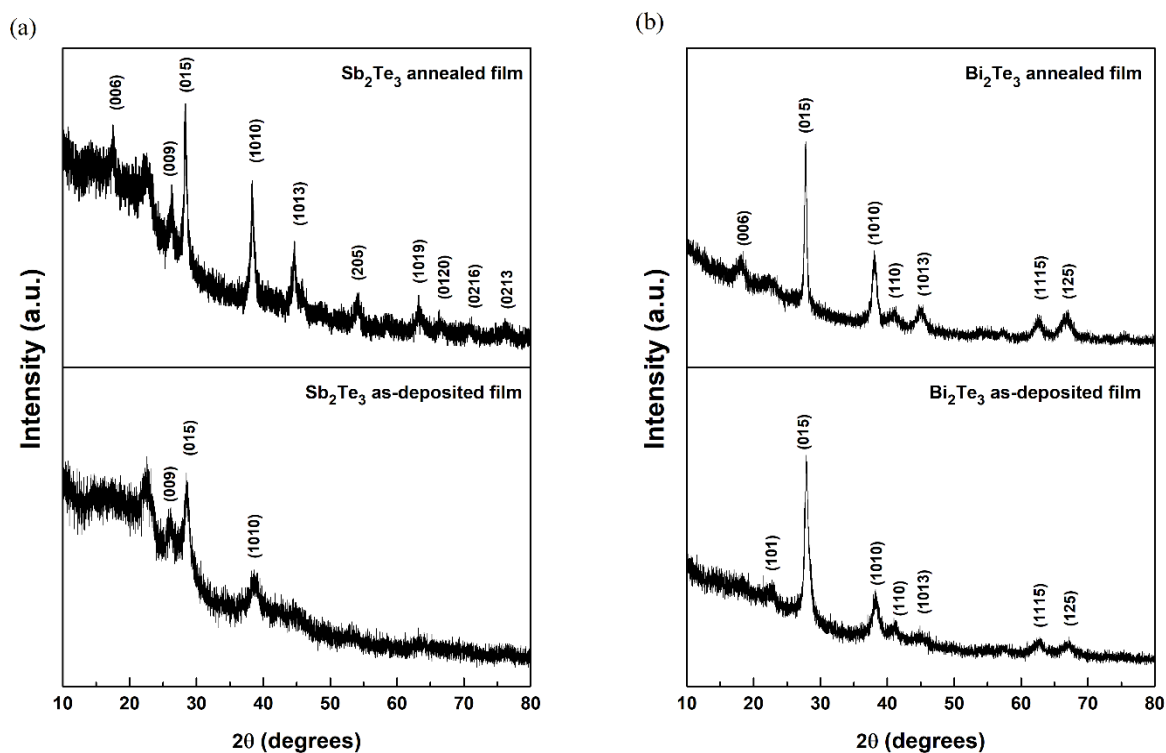


Fig. 4.9 X-ray diffraction spectra of the as-deposited (a) p- Sb_2Te_3 and (b) n- Bi_2Te_3 films annealed at 200 °C.

Figure 4.9 presents the X-ray diffraction spectra of the as-deposited and annealed films. All the peaks of the Sb_2Te_3 thin films corresponded to the antimony telluride crystalline structure (JCPDS card no. 15-0874). The as-deposited sample of Sb_2Te_3 showed low intensity peaks of the (015), (009) and (1010) planes. For the annealed sample, the intensity of (015) and (1010) peaks increased, which indicated that annealing improved the crystallinity of these thin films. All the peaks of the Bi_2Te_3 thin films corresponded to bismuth telluride crystalline structure (JCPDS card no. 15-0863). The XRD intensity of the (015) peak was the highest for all of the Bi_2Te_3 thin film samples. After annealing, the intensity of the (015) and (1010) peaks increased. Compared to the structure before annealing, the Bi_2Te_3 film had a higher crystallinity than Sb_2Te_3 , with identical deposition

parameters. The structure difference can be explained by thermodynamic properties of p-Sb₂Te₃ and n-Bi₂Te₃ [36], as shown in Eq. (4.6);

$$\Delta G = \Delta H - T(\Delta S) \quad (4.6)$$

where ΔG is the free energy, ΔH the enthalpy and ΔS the entropy. The free energy value for n-Bi₂Te₃ was -82.9 KJ/mole and for p-Sb₂Te₃ -62.4 KJ/mole [49, 50], the free energy are negative suggesting that the reaction was spontaneous. The free energy of the formation of n-Bi₂Te₃ is less than p-Sb₂Te₃. Therefore, the Bi₂Te₃ structure has a higher crystallinity than Sb₂Te₃, since the structure of n-Bi₂Te₃ is easier to form than that of p-Sb₂Te₃.

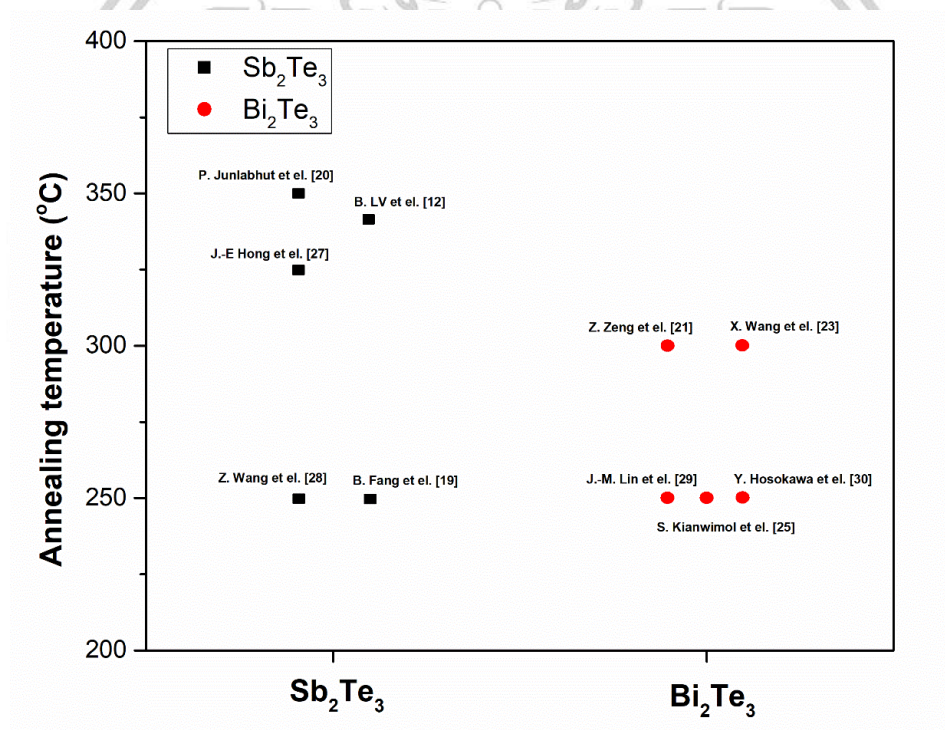


Fig. 4.10 Optimal annealing temperatures for improving the thermoelectric properties of p-Sb₂Te₃ and n-Bi₂Te₃ obtained from LV et. el.[12], Fang et. el.[19], Junlabhut et. el.[20], Zeng et. el.[21], Wang et. el.[23], Kianwimol et. el.[25], Hong et. el.[27], Wang et. el.[28], , Lin et. el.[29], and Hosokawa et. el.[30].

Figure 4.10 illustrates the optimal annealing temperatures for improving the thermoelectric properties of p-Sb₂Te₃ and n-Bi₂Te₃ previously [12, 19-21, 23,25, 27-30]. We can see that the optimal annealing temperatures for p-Sb₂Te₃ were higher than those of n-Bi₂Te₃ films. This indicated that improving the structure by annealing p-Sb₂Te₃ required a higher temperature than for n-Bi₂Te₃.

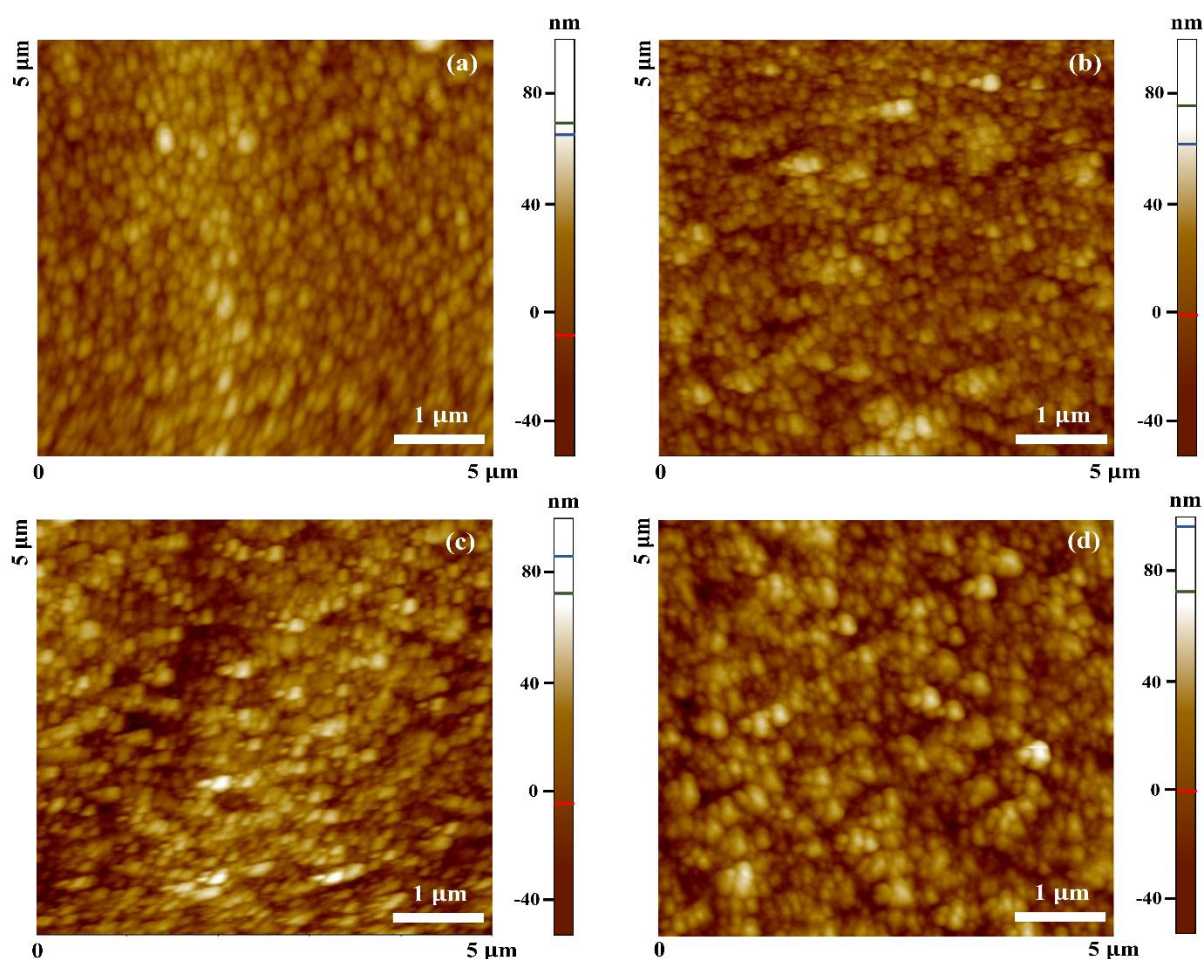


Fig. 4.11 Atomic force microscopy (2D) topography of as-deposited and annealed (a-b) p-Sb₂Te₃ and (c-d) n-Bi₂Te₃ films.

Figure 4.11 shows topography from atomic force microscopy (2D) of as-deposited and annealed films. The scan size for all films was fixed at 5x5 μm. Figs 4.11a and 4.11b illustrate that the both as-deposited films were smoother than the annealed films, because annealing caused the grains to grow and induced surface roughness.

Because of the low quality of XRD patterns, the average grain sizes of the thin films were estimated from atomic force images. The grain sizes and roughnesses are listed in Table 4.3. The average grain size of the Sb film increased from 116 to 135 nm, and for the Bi film from 143 to 156 nm, after annealing. In addition, the RMS roughness increased from 10.4 to 13.1 nm for the Sb films and from 15.9 to 17.5 nm for the Bi ones. The chemical compositions, measured by EDS, are shown in Table 1. The atomic fraction of Te atoms in the films decreased from 59.94 to 58.82 for p-Sb₂Te₃ and from 58.92 to 57.85 for n-Bi₂Te₃, after annealing. The Te content decrease was caused by evaporation of Te during annealing [7, 38].

Table 4.3 Chemical composition, RMS roughness and mean grain size from as-deposited and annealed films.

Sample	Sb (at%)	Bi (at%)	Te (at%)	RMS roughness (nm)	Mean grain size (nm)
p-Sb ₂ Te ₃ (as-deposited)	40.06	-	59.94	10.4	116
p-Sb ₂ Te ₃ (annealed)	41.18	-	58.82	13.1	135
n-Bi ₂ Te ₃ (as-deposited)	-	41.08	58.92	15.9	143
n-Bi ₂ Te ₃ (annealed)	-	42.15	57.85	17.5	156

Figure 4.12 shows FE-SEM images and cross-sectional morphology of as-deposited and annealed films. The surface morphology changed little with annealing. The thickness of both films slightly decreased after annealing, due to evaporation of Te atoms [20].

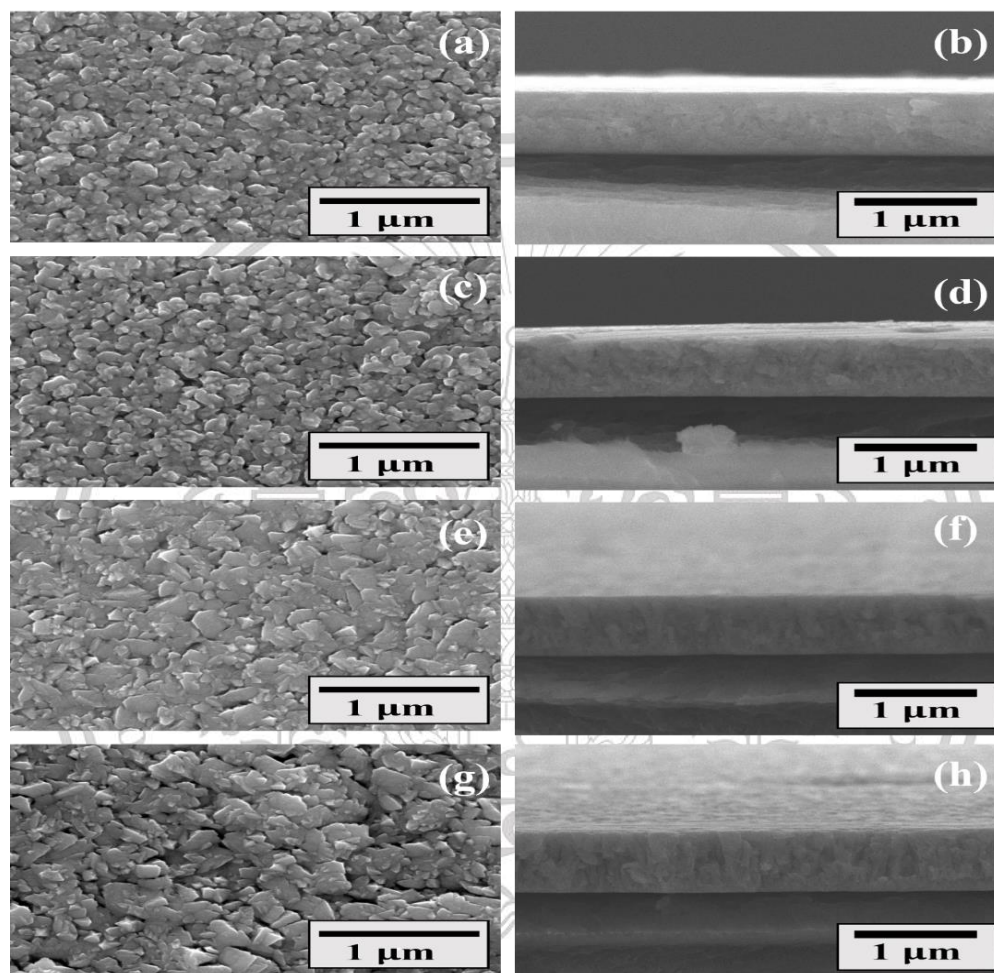
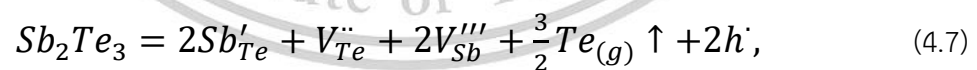


Fig. 4.12 FE-SEM images and cross-sections of the as-deposited (a-d) p-Sb₂Te₃ and (e-h) n-Bi₂Te₃ thin films annealed at 200 °C.

Table 4.4 Electrical properties of as-deposited and annealed films at room temperature.

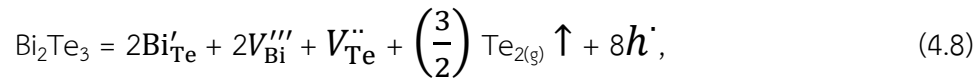
Sample	p-Sb ₂ Te ₃		n-Bi ₂ Te ₃	
	Carrier concentration (×10 ²⁶ m ⁻³)	Mobility (×10 ⁻⁴ m ² /Vs)	Carrier concentration (×10 ²⁶ m ⁻³)	Mobility (×10 ⁻⁴ m ² /Vs)
As-deposited	0.21	3.86	-7.22	1.02
Annealed	1.42	10.22	-5.98	2.21

The carrier concentration and mobility of all films was measured at room temperature by Hall effect, see Table 2. The carrier concentration of the p-Sb₂Te₃ film increased from 0.21×10²⁶ to 1.42×10²⁶ m⁻³ with annealing. The increase of carrier concentration was due to evaporation of Te atoms, which generated Te vacancies ($V_{Te}^{\cdot\cdot}$). Subsequently, Te antisite defects (Sb'_{Te}) were generated and lead to Sb vacancies (V_{Sb}'''). The interaction between Sb'_{Te} and V_{Sb}''' is explained by equation (4.7) [51]:



where h^{\cdot} and \uparrow denote the created hole and the evaporation, respectively, of Te. From equation (4.7), the evaporation of Te created holes, which enhanced the carrier concentration. The carrier concentration of as-deposited n-Bi₂Te₃ film, on the other hand was about -7.22×10²⁶ m⁻³ and decreased to -5.98×10²⁶ m⁻³ after annealing. The reduction in the carrier concentration resulted from the evaporation of Te atoms, which generated

$V_{Te}^{\bullet\bullet}$. Subsequently, Bi'_{Te} (bismuth antisite defects) and $V_{Bi}^{\bullet\bullet\bullet}$ (bismuth vacancies) become involved as Bi atoms entered the $V_{Te}^{\bullet\bullet}$, as explained by equation (4.8) [43]:



From equation (4.8), the evaporation of Te atoms created holes, and the carrier concentration of Bi_2Te_3 thin films was decreased filling in those holes.

From Table 4.4, we see that the carrier mobility of both films after annealing was higher than that of the as-deposited films. The carrier mobility of p- Sb_2Te_3 film increased from 3.86×10^{-4} to 10.22×10^{-4} m^2/Vs and for n- Bi_2Te_3 from 1.02×10^{-4} to 2.21×10^{-4} m^2/Vs , with annealing. The carrier mobility increase was due to larger film crystallites.

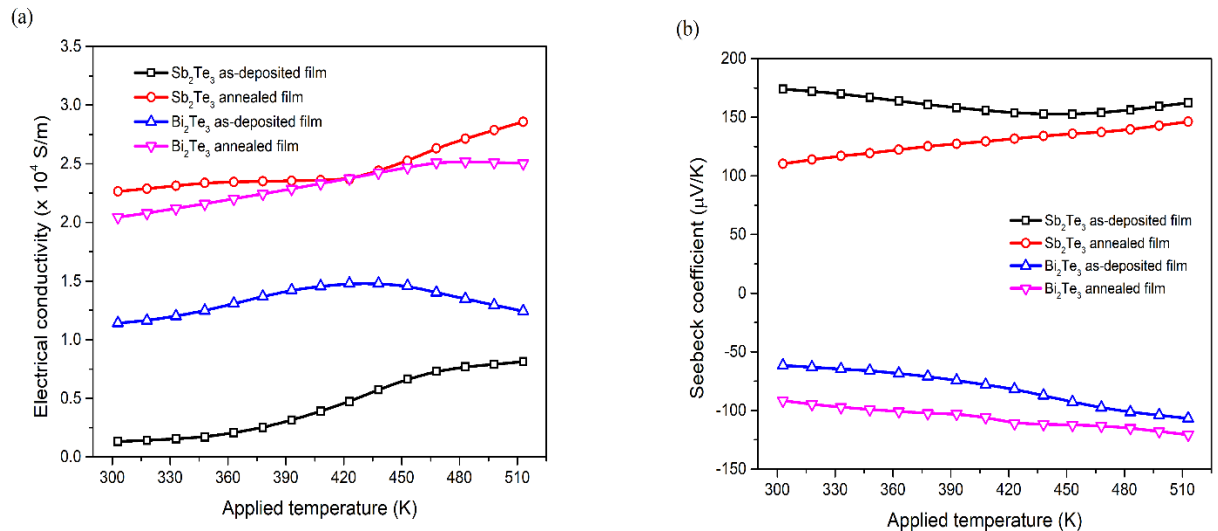
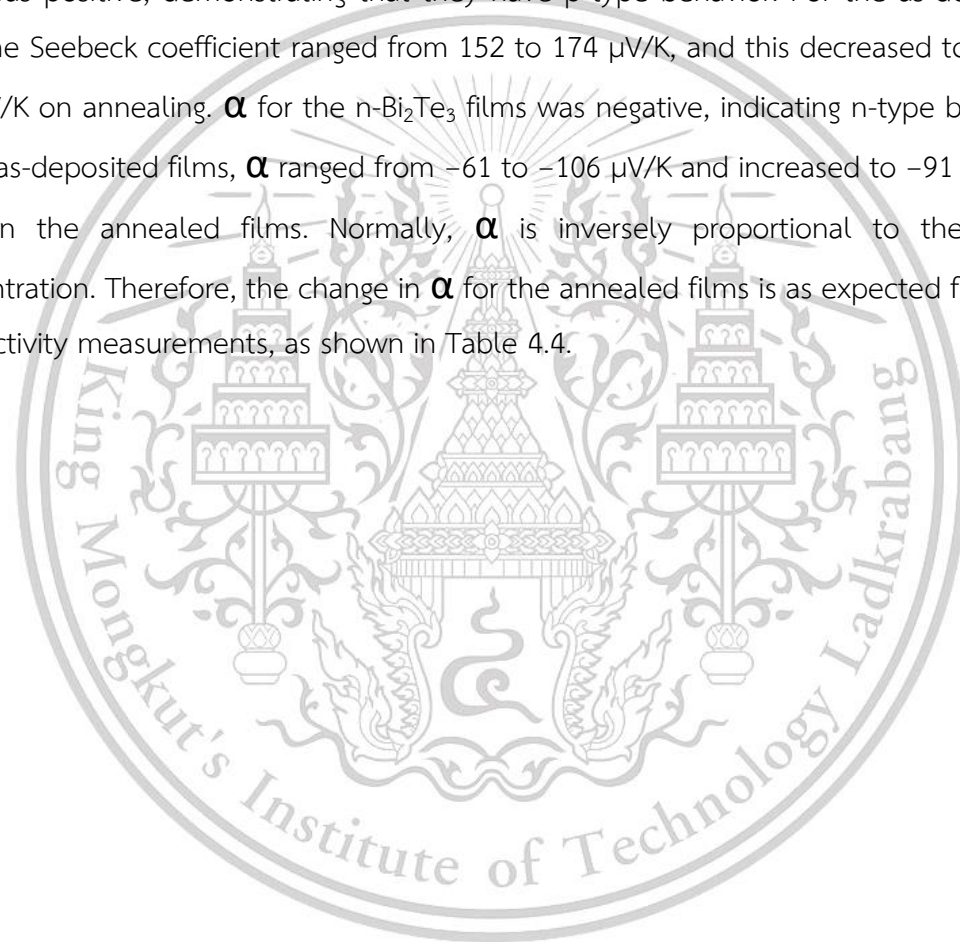


Fig. 4.13 (a) Electrical conductivity and (b) Seebeck coefficient vs applied temperature for as-deposited and annealed films.

The electrical conductivity (σ) of the as-deposited and annealed films versus the applied temperature is shown in Fig. 4.13a. The conductivity, σ , of the annealed p- Sb_2Te_3 film increased from 0.13×10^4 to 0.81×10^4 S/m to 2.26×10^4 to 2.85×10^4 S/m. Similarly, the conductivity of the n- Bi_2Te_3 film increased from 1.14×10^4 to 1.24×10^4 S/m to 2.04×10^4 to 2.52×10^4 S/m on annealing. The conductivity of the annealed p- Sb_2Te_3 films increased

more than that of the annealed n-Bi₂Te₃ films, owing to the changed mobility and carrier concentration (see Table 4.4). Evidently, the carrier concentration of the annealed p-Sb₂Te₃ films increased whereas that of the annealed n-Bi₂Te₃ decreases due to Te evaporation.

The Seebeck coefficient, α , of the as-deposited and annealed p-Sb₂Te₃ and n-Bi₂Te₃ films versus applied temperature is shown in Fig. 4.13b. The α for the p-Sb₂Te₃ thin films was positive, demonstrating that they have p-type behavior. For the as-deposited film, the Seebeck coefficient ranged from 152 to 174 $\mu\text{V/K}$, and this decreased to 110 to 146 $\mu\text{V/K}$ on annealing. α for the n-Bi₂Te₃ films was negative, indicating n-type behavior. In the as-deposited films, α ranged from -61 to -106 $\mu\text{V/K}$ and increased to -91 to -120 $\mu\text{V/K}$ in the annealed films. Normally, α is inversely proportional to the carrier concentration. Therefore, the change in α for the annealed films is as expected from the conductivity measurements, as shown in Table 4.4.



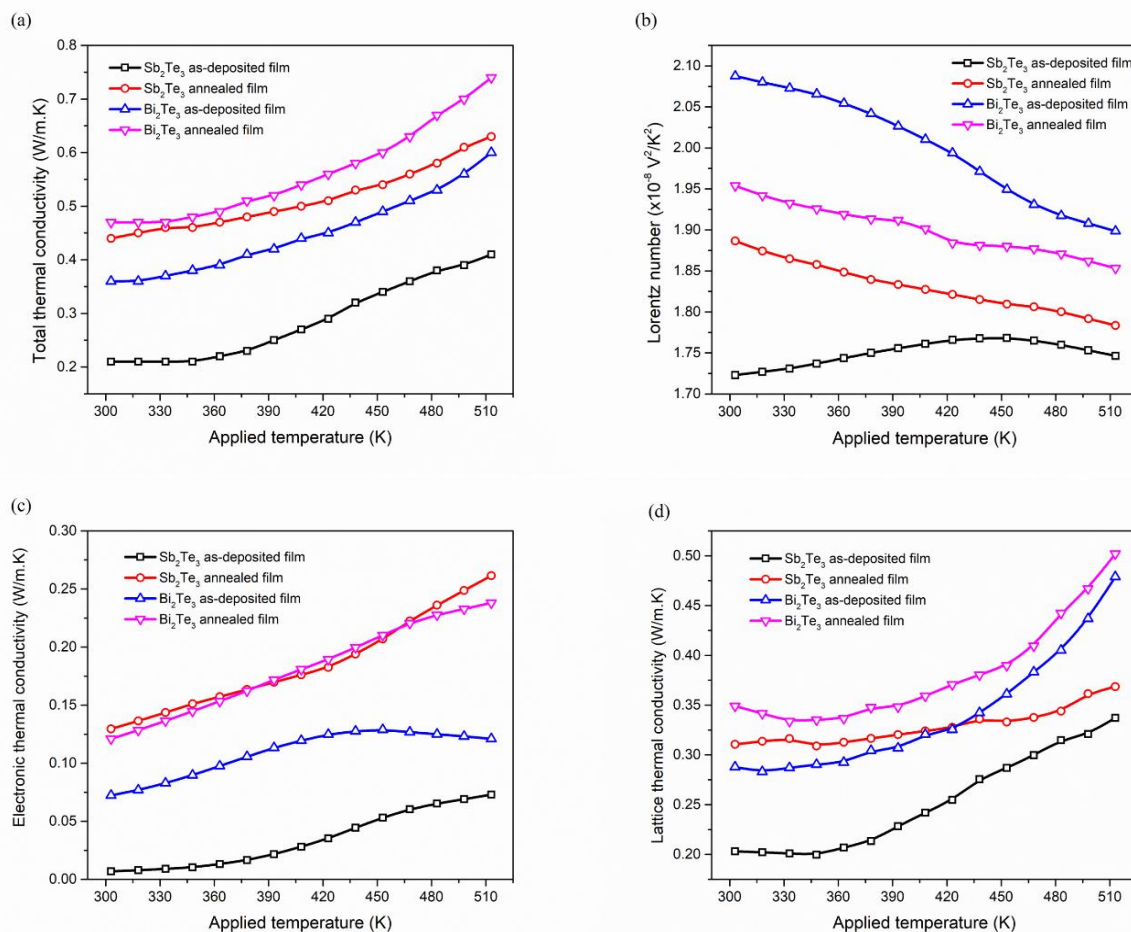


Fig. 4.14 Temperature dependent (a) total thermal conductivity, (b) calculated Lorentz numbers, (c) electronic thermal conductivity and (d) lattice thermal conductivity for as-deposited and annealed films.

The temperature dependence of total thermal conductivity, k_{tot} , of the as-deposited and annealed films is presented in Fig. 4.14(a). k_{tot} for both films increased with applied temperature, due to the carrier (electron or hole) concentrations beginning to play a dominant role at high temperatures [52]. In addition, k_{tot} for both annealed films was larger than that of the as-deposited films, attributed to improved crystallinities, as shown in Table 4.3. This is consistent with previous research on the influence of the nanostructure and decreased phonon scattering, at the grain boundaries, on thermal conductivity of annealed films [53-56]. We see k_{tot} of both films was lower than that of the bulk thermoelectric materials ($\sim 1.3 \text{ W}\cdot\text{m}^{-1}\cdot\text{K}^{-1}$) [57-61]. The electronic thermal

conductivity, k_{ele} , and lattice thermal conductivity, k_{lat} , can be expressed as total thermal conductivity: $k_{tot}=k_{lat}+k_{ele}$. Generally, the relationship between k_{ele} and σ can be calculated with the Wiedemann–Franz law, $k_{ele}=L\sigma T$, where L is the Lorenz number, calculated from Equation (4.9) and shown in Fig. 4.14(b) [62]:

$$L = 1.5 + \exp \left[-\frac{|\alpha|}{116} \right] \quad (4.9)$$

Figure 4.14(b) shows the temperature dependence of L for the as-deposited and annealed films. L for the annealed p-Sb₂Te₃ film is larger than that of the as-deposited film, because of the reduction in α after annealing. Conversely, L value for the annealed n-Bi₂Te₃ films was smaller than that of the as-deposited films, because α increased with annealing. k_{ele} for both films is shown in Fig. 4.14(c). k_{ele} of the annealed films increased with annealing. In Fig 4.14 (d), k_{lat} can be estimated as $k_{lat}=k_{total}-k_{ele}$. k_{lat} for both films increased with applied temperature. The increase in k_{lat} at high temperature was attributed to the bipolar effect [52,53]. The bipolar effect is observed in small band gap materials, since these materials have a mixture of carriers (electrons and holes) in each band [54]. k_{lat} for the annealed films was larger than that of the as-deposited films, due to the crystal growth on annealing. Crystal growth decreases grain boundaries, which reduces phonon scattering at the boundaries and, in turn, increased k_{lat} . A similar result for thin films was also reported by Masayuki et al. [54] and Park et al. [63]. Masayuki et al. reported that k_{lat} increased from 0.29 to 0.39 W.m⁻¹.K⁻¹ with a grain size increase from 38 to 93 nm; Park et al. reported k_{lat} increased from 0.61 to 1.08 W.m⁻¹.K⁻¹ with a grain size increase from 88 to 129 nm.

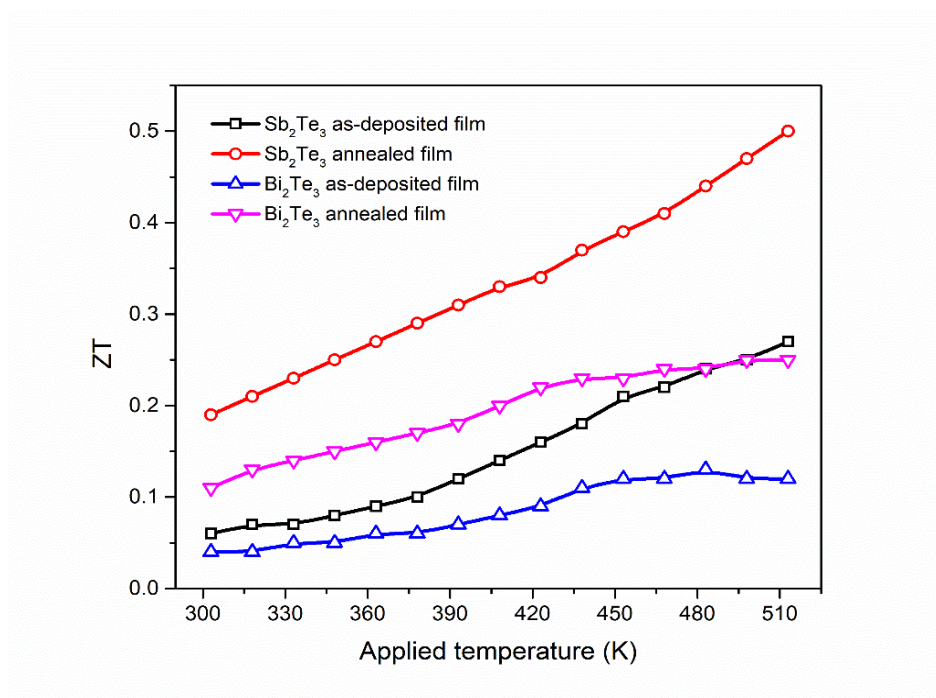


Fig. 4.15 Dimensionless figure of merit vs applied temperature for as-deposited and annealed films.

The ZT value versus applied temperature for all films is in Fig. 4.15. ZT increased with temperature. ZT of the annealed films was enhanced by the annealing. In our work, the maximum ZT of the annealed films was about 0.5 for p- Sb_2Te_3 and 0.25 for n- Bi_2Te_3 at an applied temperature of 513 K.

Table 4.5 Different deposited conditions and thermoelectric properties of p-Sb₂Te₃ and n-Bi₂Te₃ films deposited by DC magnetron sputtering at 513 K.

Materials	Sputtering time (min)	Substate	Annealing temperature (°C)	Electrical conductivity ($\times 10^4$ S.m ⁻¹)	Seebeck coefficient (μ V.K ⁻¹)	Thermal conductivity (W.m ⁻¹ .K ⁻¹)	ZT
p-Sb ₂ Te ₃ [18]	60	polyimide sheet	300	5.2	160	-	-
p-Sb ₂ Te ₃ [20]	60	polyimide sheet	350	2.5	225	-	-
n-Bi ₂ Te ₃ [25]	75	polyimide sheet	250	5.5	-155	-	-
p-Sb ₂ Te ₃ [This work]	5	silicon wafer	200	2.8	146	0.63	0.5
n-Bi ₂ Te ₃ [This work]	5	silicon wafer	200	2.5	-120	0.74	0.25

Different deposition conditions and thermoelectric properties of p-Sb₂Te₃ and n-Bi₂Te₃ films deposited by sputtering with our previous work is presented in Table 3. Compared with our previous work [18,20,25], this work p-Sb₂Te₃ and n-Bi₂Te₃ were deposited with different sputtering time, substrate and annealing temperature. This indicated that factor for improve thermoelectric properties depend on sputtering time, substrate and annealing temperature. Therefore, enhanced thermoelectric properties depend on optimize deposition conditions. However, the result of electrical conductivity and Seebeck coefficient insufficient for thermoelectric properties report. Thermoelectric properties should be reported electrical conductivity, Seebeck coefficient and thermal conductivity as reported in this work.

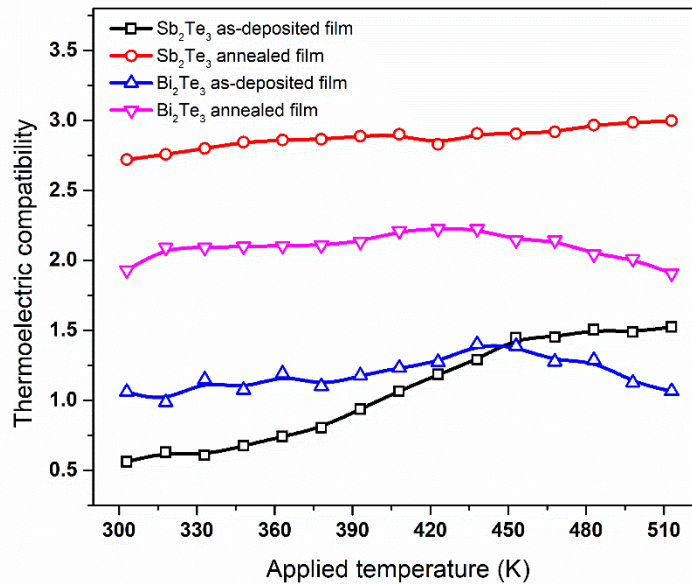


Fig. 4.16 Thermoelectric compatibility factor, S , of as-deposited and annealed p-Sb₂Te₃ and n-Bi₂Te₃ films.

For thermoelectric module fabrication, ZT values and also the compatibility factor, S , must be taken into account. The S factor is a thermodynamic property essential for designing an efficient segmented thermoelectric nodule. The S factor is defined:

$$S = \frac{\sqrt{1+ZT}-1}{\alpha T} \quad (4.10)$$

Thus, the goal is to select high ZT values that have similar S factors. If the S factors differ by a factor of 2 or less, both the thermoelectric materials and segmentation will be efficient [64]. Thus, the S factors of the films were calculated and compared, as shown in Fig. 4.16, which shows that both annealed n-Bi₂Te₃ and p-Sb₂Te₃ had appropriate S values, differing by a factor < 2 . However, we can reduce the difference in the S values by improving the ZT value of n-Bi₂Te₃.

We can see that n-Bi₂Te₃ had a higher thermal conductivity than p-Sb₂Te₃, indicating that annealing was not sufficient to improve the thermoelectric properties or ZT value of n-Bi₂Te₃. Therefore, the n-Bi₂Te₃ film should improve σ and reduce k_{lat} . In previous work on

n-Bi₂Te₃, σ was increased and k_{lat} reduced by doping. Table 4.6 shows σ and k_{lat} for n-Bi₂Te₃ at room temperature with Cu [65], Sn, Cul, Cul-Sn [66] and Cul-Pb [67] doping.

Table 4.6 Electrical conductivity and lattice thermal conductivity of n-Bi₂Te₃ at room temperature with various dopants.

Reference	Doping type	Electrical conductivity (S/cm)		Lattice thermal conductivity (W/m.K)	
		un-doped	doped	un-doped	doped
Han [65]	Cu	500	700	1.15	0.65
Han [66]	Sn	300	500	1.45	0.7
Han [66]	Cul	300	2,000	1.45	0.45
Han [66]	Cul-Sn	300	2,200	1.45	0.25
Han [67]	Cul-Pb	300	3,700	1.45	0.1

4.3 Fabricate and measuring power output from thermoelectric generator.

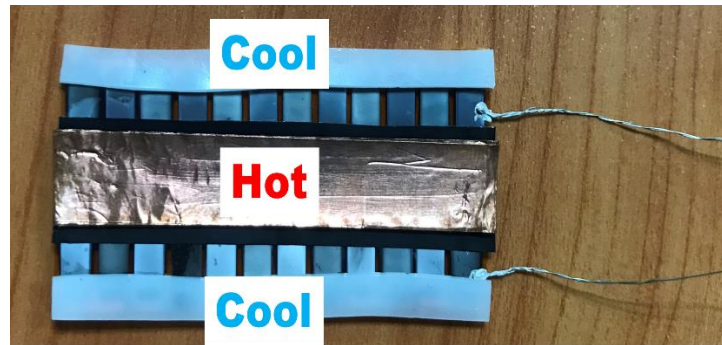


Fig. 4.17 Prototype flexible thermoelectric module.

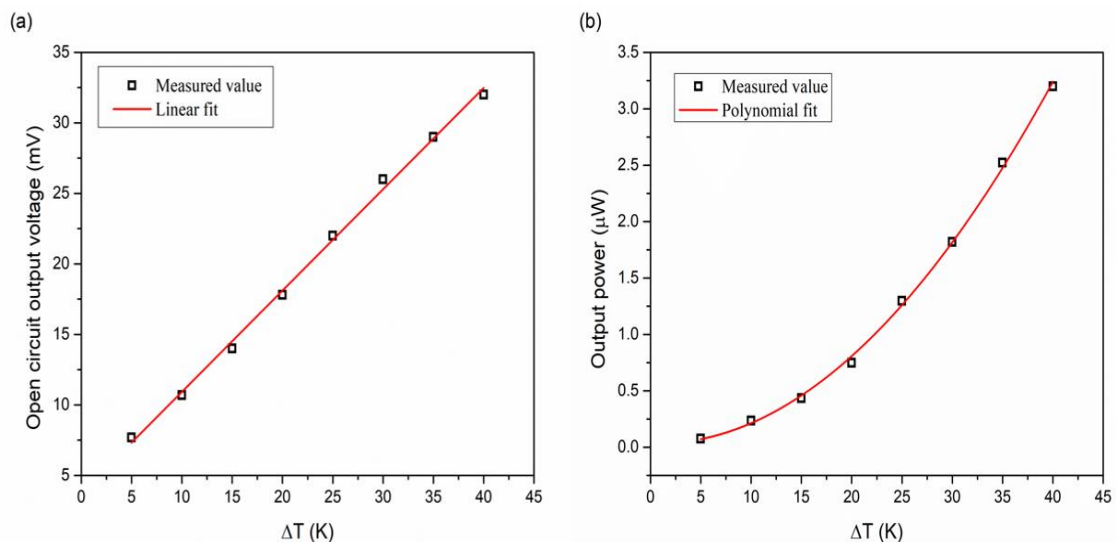


Fig. 4.18 (a) Thermoelectric generator open circuit output voltage (V_{OC}) and output power (P_{out}) of the generator as functions of different temperature gradients.

Fig.4.18a-4.18b illustrate the experimental differentiation of the open circuit output voltage and output power of the thermoelectric generator as functions of different temperature between hot and cold junctions ($\Delta T = 5 - 40$ K). The open circuit output voltage at 40 K different temperature was generated about 32 mV, with an output power of generator up to 3.2 μW .

Table 4.7 compares output power of thermoelectric generator device was deposited by DC sputtering on Kapton substrate with light weight method; self-rolled thin film as TE leg [34], co-sputtering; Thick Kapton [15], Screen printing; Kapton [10], Sputtering; Standard paper [35], Dispenser printing; PDMS [9] and RF-sputtering; Glass [36]. The output power of thermocouple of antimony telluride (p-type) and bismuth telluride (n-type) thin films prepared by DC magnetron sputtering and annealed at 200 °C is comparable to that obtained with different method and substrate for flexible thermoelectric generator.

Table 4.7 A comparable maximum output power of TEG device with different method and substrate.

Method and substrate	Materials		Different temperature (ΔT , K)	Open circuit output voltage (OCV, mV)	Maximum output power (P_{max} , μW)
	P-type	N-type			
Light weight; self-rolled thin film as TE leg [34]	Sb ₂ Te ₃	Bi ₂ Te ₃	60	-	5.0
Co-sputtering; Thick Kapton [15]	Sb ₂ Te ₃	Bi ₂ Te ₃	40	430	0.032
Screen printing; Kapton [10]	Sb ₂ Te ₃	Bi ₂ Te ₃	20	-	0.195
Sputtering; Standard paper [35]	Sb ₂ Te ₃	Bi ₂ Te ₃	75	190.7	0.024
Dispenser printing; PDMS [9]	Bi ₂ Te ₃	Bi ₂ Te ₃	19	7	2.1
RF sputtering; Glass [1]	Sb ₂ Te ₃	Bi ₂ Te ₃	28	32	0.15
DC sputtering; Kapton [This research]	Sb ₂ Te ₃	Bi ₂ Te ₃	40	32	3.2

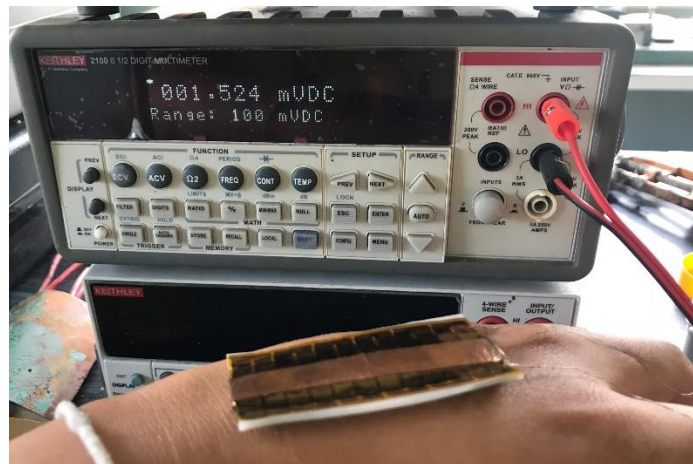


Fig. 4.19 Thermoelectric generator open circuit output voltage (V_{oc}) with body heat human.

Thermoelectric generator open circuit output voltage (V_{oc}) with body heat human as show in Fig. 4.19. The open circuit output voltage with heat from human body was generated about 1.52 mV.

Chapter 5

Conclusion

5.1 Effect of annealing temperature on thermoelectric properties of bismuth telluride thick film deposited by DC magnetron sputtering

In summary, we investigated in this work how annealing affects the structural and thermoelectric properties of thick Bi_2Te_3 films deposited by DC magnetron sputtering. The XRD patterns show that the films have a hexagonal structure. After annealing, the crystallinity of the films increases. The XPS spectra show that the surface chemical composition of the films decreases with increasing annealing temperature. The maximum electrical conductivity of 5.84 S/m is obtained by annealing at 250 °C. The Seebeck coefficient ranges from 97 to 145 $\mu\text{V}/\text{K}$ in as-deposited film and increases to 147 to 155 $\mu\text{V}/\text{K}$ upon annealing at 250 °C. The maximum power factor of 1.21 $\text{mW K}^{-2} \text{m}^{-1}$ is obtained by annealing at 250 °C. The maximum power output of 0.98 μW at a temperature difference of 50 °C for thick, thermoelectric Bi_2Te_3 film is obtained by annealing at 250 °C.

5.2 Comparison of the thermoelectric properties of Bi_2Te_3 and Sb_2Te_3 films deposited via the DC magnetron sputtering technique.

In summary, deposited p- Sb_2Te_3 and n- Bi_2Te_3 thin films were produced by direct current magnetron sputtering. The formation of the structure of the as-deposited and annealed n- Bi_2Te_3 was easier than that of the p- Sb_2Te_3 films, confirmed from XRD. The electrical conductivity of the annealed p- Sb_2Te_3 increases more than that of the annealed n- Bi_2Te_3 , owing to changes in mobility and carrier concentration. Evidently, the carrier concentration of the annealed p- Sb_2Te_3 increased, whereas that of the annealed n- Bi_2Te_3 decreased, owing to Te evaporation. The changing of the Seebeck coefficient of p- Sb_2Te_3 and n- Bi_2Te_3 was inversely proportional to the carrier concentration. The crystalline growth had more noticeable effects on the increase in the total thermal conductivity of the annealed n- Bi_2Te_3 film than on the p- Sb_2Te_3 film, because of the easier crystal growth in

n-Bi₂Te₃, and therefore the lattice thermal conductivity of n-Bi₂Te₃ was higher. In our work, the maximum ZT value of the annealed p-Sb₂Te₃ was 0.5 and for n-Bi₂Te₃ was 0.25, at 513 K. The annealed n-Bi₂Te₃ and annealed p-Sb₂Te₃ films had appropriate S values, i.e. differing by a factor < 2 .

5.3 Fabricate and measuring power output from thermoelectric generator.

In summary, designed thermoelectric generator from the thermoelectric properties of annealed p-Sb₂Te₃ and n-Bi₂Te₃ film. The open circuit output voltage and output power of the thermoelectric generator increase with increasing different temperature (hot and cold junctions), the maximum of open circuit output voltage about 32 mV and maximum output power about 3.2 μ W at 40 K different temperature. The open circuit output voltage with heat from human body was generated about 1.52 mV. In the future, the open circuit output voltage and output power of the thermoelectric generator can be further improved if higher ZT values.

Reference

- [1] L. Francioso, C. D. Pascali, I. Farell, C. Martucci, P. Creti, P. Siciliano, A. Perrone, Flexible thermoelectric generator for ambient assisted living wearable biometric sensors, *J. Power Sources* 196 (2011) 3239–3243.
- [2] S. Beeby, N. White, Energy Harvesting for Autonomous Systems, MA : Artech House, Norwood, 2010.
- [3] W. Glatz, E. Schwyter, L. Durrer, C. Hierold, S. Member, Bi₂Te₃-based flexible micro thermoelectric generator with optimized design, *J. Microelectromech. Syst.* 18 (2009) 763-772.
- [4] T. C. Harman, P. J. Taylor, M. P. Walsh, B. E. LaForge, Quantum dot superlattice thermoelectric materials and devices, *Science* 297 (2002) 2229-2232.
- [5] T. Khumtong, A. Sakulalavek, R. Sakdanuphab, Empirical modelling and optimization of pre-heat temperature and Ar flow rate using response surface methodology for stoichiometric Sb₂Te₃ thin films prepared by RF magnetron sputtering, *J. Alloy. Compd.* 715 (2017) 65-72.
- [6] J. P. Heremans, Low-Dimensional Thermoelectricity, *Acta Phys. Pol. A* 108 (2005) 609-634.
- [7] L.M. Goncalves, C. Couto, P. Alpuim, A.G. Rolob, F. Völklein, J.H. Correia, Optimization of thermoelectric properties on Bi₂Te₃ thin films deposited by thermal co-evaporation, *Thin Solid Films* 518 (2010) 2816–2821.
- [8] A. Giani, A. Boulouz, F. Pascal-Delannoy, A. Foucaran, E. Charles, A. Boyer, Growth of Bi₂Te₃ and Sb₂Te₃ thin films by MOCVD, *Mater. Sci. Eng. B* 64 (1999)19-24.
- [9] N. Peranio, O. Eibl, J. Nurnus, Structural and thermoelectric properties of epitaxially grown Bi₂Te₃ thin films and superlattices, *J. Appl. Phys.* 100 (2006) 114306.
- [10] S. E. Jo, M. K. Kim, M. S. Kim, Y. J. Kim, Flexible thermoelectric generator for human body heat energy harvesting, *Electron. Lett.* 48 (2012) 1015-1017.

Reference (continue)

- [11] J.-H. Kim, J.-Y. Choi, J.-M. Bae, M.-Y. Kim, T.-S. Oh, Thermoelectric characteristics of n-type Bi_2Te_3 and p-type Sb_2Te_3 thin films prepared by co-evaporation and annealing for thermopile sensor applications, *Mater. Trans.* 54 (2013) 618-625.
- [12] B. Lv, S. Hu, W. Li, X. Di, L. Feng, J. Zhang, L. Wu, Y. Cai, B. Li, Z. Lei, Preparation and characterization of Sb_2Te_3 thin Films by co-evaporation, *Int. J. Photoenergy* 2010 (2010) 476589.
- [13] Z. Cao, E. Koukharenko, M. J. Tudor, R. N. Torah, S.P. Beeby, Screen printed flexible Bi_2Te_3 - Sb_2Te_3 based thermoelectric generator, *J. Phys. Conf. Ser.* 476 (2013) 012031.
- [14] R. Roth, R. Rostek, K. Cobry, C. Kohler, M. Grohand, P. Woias, Design and characterization of micro thermoelectric cross-plane generators with electroplated Bi_2Te_3 , Sb_xTe_y , and reflow soldering, *J. Microelectromech. Syst.* 23 (2014) 961-971.
- [15] E. Mu, G. Yang, X. Fu, F. Wang, Z. Hu, Fabrication and characterization of ultrathin thermoelectric device for energy conversion, *J. Power Sources* 394 (2018) 17-25.
- [16] H.-J. Lee, H. S. Park, S. Han, J. Y. Kim, Thermoelectric properties of n-type Bi-Te thin films with deposition conditions using RF magnetron co-sputtering, *Thermochim.* 452 (2012) 57-61.
- [17] H. Huang, W.-L. Luan, S.-T. Tu, Influence of annealing on thermoelectric properties of bismuth telluride films grown via radio frequency magnetron sputtering, *Thin Solid Films* 517 (2009) 3731-3734.
- [18] P. Fan, Z.-H. Zheng, G.-X. Liang, D.-P. Zhang, X.-M. Cai, Thermoelectric characterization of ion beam sputtered Sb_2Te_3 thin films, *J. Alloys Compd.* 505 (2010) 278-280.
- [19] B. Fang, Z. Zeng, X. Yan, Z. Hu, Effects of annealing on thermoelectric properties of Sb_2Te_3 thin films prepared by radio frequency magnetron sputtering, *J. Mater. Sci. Mater. Electron.* 24 (2013) 1105-1111.

Reference (continue)

- [20] P. Junlabhut, P. Nuthongkumb, A. Sakulkalaveka, A. Harnwunggmoung, P. Limsuwana, R. Sakdanuphab, Enhancing the thermoelectric properties of sputtered Sb_2Te_3 thick films via post-annealing treatment, *Surf. Coat. Technol.* 387 (2020) 125510.
- [21] Z.-H. Zheng, P. Fan, G.-X. Liang, D-P Zhang, X.-M. Cai, T.-B. Chen, Annealing temperature influence on electrical properties of ion beams sputtered Bi_2Te_3 thin films, *J. Phys. Chem. Solids* 71 (2010) 1713-1716.
- [22] D.-H. Kim, G.-H. Lee, Effect of rapid thermal annealing on thermoelectric properties of bismuth telluride films grown by co-sputtering, *Mater. Sci. Eng. B* 131 (2006) 106-110.
- [23] X. Wanga, H. Hea, N. Wanga, L. Miao, Effects of annealing temperature on thermoelectric properties of Bi_2Te_3 films prepared by co-sputtering, *Appl. Surf. Sci.* 276 (2013) 539-542.
- [24] Z. Zeng, P. Yanga, Z. Hu, Temperature and size effects on electrical properties and thermoelectric power of Bismuth Telluride thin films deposited by co-sputtering, *Appl. Surf. Sci.* 268 (2013) 472-476.
- [25] S. Kianwimol, R. Sakdanuphab, N. Chanlek, A. Harnwunggmoung, A. Sakulkalavek, Effect of annealing temperature on thermoelectric properties of bismuth telluride thick film deposited by DC magnetron sputtering, *Surf. Coat. Technol.* 393 (2020) 125808.
- [26] D. M. Rowe, Thermoelectrics, an environmentally-friendly source of electrical power, *Renew. Energy* 16 (1999) 1251-1256.
- [27] J.-E. Hong, S.-K. Lee, S.-G. Yoon, Enhanced thermoelectric properties of thermal treated Sb_2Te_3 thin films, *J. Alloys Compd.* 583 (2014) 111-115.
- [28] Z. Wang, Y. Hu, W. Li, G. Zeng, L. Feng, J. Zhang, L. Wu, J. Gao, Effect of annealing on the properties of antimony telluride thin films and their applications in CdTe solar cells, *Int. J. Photoenergy* 2014 (2014) 341518.

Reference (continue)

- [29] J-M. Lin, Y.-C. Chen, C-P. Lin, Annealing effect on the thermoelectric properties of Bi_2Te_3 thin Films prepared by thermal evaporation method, *J. Nanomater.* 2013 (2013) 201017.
- [30] Y. Hosokawa, K. Wada, M. Tanaka, K. Tomita, M. Takashiri, Thermal annealing effect on structural and thermoelectric properties of hexagonal Bi_2Te_3 nanoplate thin films by drop-casting technique, *Jpn. J. Appl. Phys.* 57 (2018) 02CC02.
- [31] Idtechex. 2012. The Seebeck or Peltier effects. [online]. Available : <http://www.idtechex.com/research/articles/thermoelectric-generators-a-750-million-market-by-2022-00004631.asp>
- [32] Laird. 2016. Thermoelectric modules. [online]. Available : <http://www.lairdtech.com/product-categories/thermal-management/thermoelectric-modules>
- [33] TEGway. 2017. Flexible Thermoelectric. [online]. Available : <https://www.roadtovr.com/tegway-thermoreal-thermoelectric-skin-thermal-haptics-vr>
- [34] D.M. Rowe, CRC Handbook of Thermoelectrics, first ed., FL : CRC Press, Boca Raton, 1995.
- [35] D.M. Rowe, C.M. Bhandari, Modern Thermoelectrics, Va. : Reston Pub. Co., Reston, 1983.
- [36] D.G. Cahill, W.K. Ford, K.E. Goodson, G.D. Mahan, A. Majumdar, H.J. Maris, R. Merlin, S.R. Phillpot, Nanoscale thermal transport, *J. Appl. Phys.* 93 (2003) 793-818.
- [37] S.J. Kim, J.H. We, G.S. Kim, B.J. Cho, Thermoelectric properties of P-type Sb_2Te_3 thick film processed by a screen-printing technique and a subsequent annealing process, *J. Alloys Compd.* 582 (2014) 177-180.
- [37] V.D. Mote, Y. Purushotham, B.N. Dole, Williamson-Hall analysis in estimation of lattice strain in nanometer-sized ZnO particles, *J. Theor. App. Mech-Pol.* 8 (2012) 2251-7235.

Reference (continue)

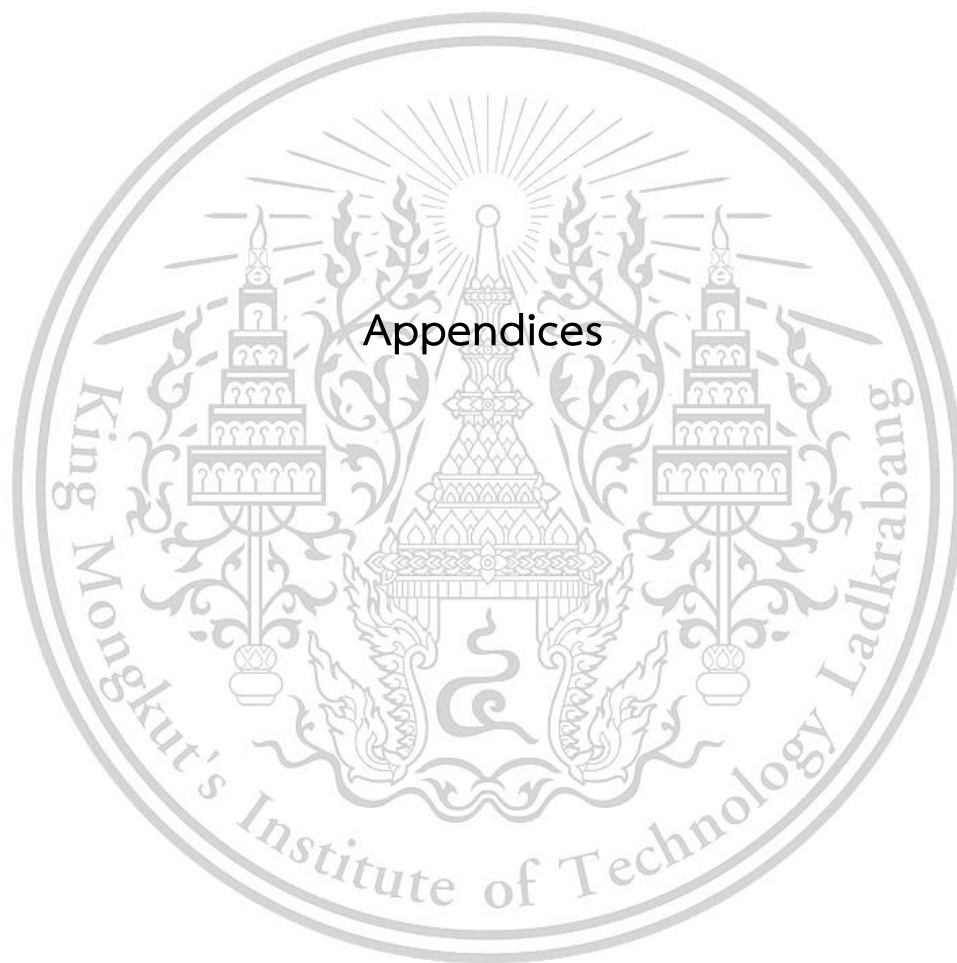
- [38] F. Völklein, Thermal conductivity and diffusivity of a thin film $\text{SiO}_2\text{-Si}_3\text{N}_4$ sandwich system, *Thin Solid Films* 188 (1990) 27-33.
- [39] N. Somdock, S. Kianwimol, A. Harnwungmoung, A. Sakulalavek, R. Sakdanuphab, Simultaneous stoichiometric composition and highly (00l) orientation of flexible Bi_2Te_3 thin films via optimising the DC magnetron sputter-deposition process, *J. Alloys Compd.* 773 (2019) 78-85.
- [40] S. Liu, N. Peng, Y. Bai, D. Ma, F. Ma, K. Xu, Self-formation of thickness tunable Bi_2Te_3 nanoplates on thin films with enhanced thermoelectric performance, *RSC Adv.* 6 (2016) 31668-31674.
- [41] V.D. Mote, Y. Purushotham, B.N. Dole, Williamson-Hall analysis in estimation of lattice strain in nanometer-sized ZnO particles, *J Theor App Mech-Pol.* 8 (2012) 2251-7235.
- [42] J. Kim, E.H. Shin, M.K. Sharma, K. Ihm, O. Dugerjav, C. Hwang, H. Lee, K.T. Ko, J.H. Park, M. Kim, H. Kim, M.H. Jung, Observation of Restored Topological Surface States in Magnetically Doped Topological Insulator, *Sci. Rep.* 9 (2019) 1331.
- [43] Z. Starý, J. Horák, M. Stordeur, M. Stölzer, Antisite defects in $\text{Sb}_{2-x}\text{Bi}_x\text{Te}_3$ mixed crystals, *J. Phys. Chem. Solids* 49 (1988) 29-34.
- [44] C.D. Wagner, Sensitivity factors for XPS analysis of surface atoms, *J. Electron. Spectrosc. Relat. Phenom.* 32 (1983) 99-102.
- [45] T. Yoo, K. Kim, W. Jang, The effect of the ring opening polymerization and chain spacing on the coefficient of thermal expansion and modulus of polyimide, *J. Appl. Polym. Sci.* 42607 (2015) 1-9.
- [46] D. Madan, A. Chen, P.K. Wright, J.W. Evans, Dispenser printed composite thermoelectric thick films for thermoelectric generator applications, *J. Appl. Phys.* 109 (2011) 034904.
- [47] H. Shen, S. Lee, J. Kang, T. Eom, H. Lee, C. Kang, S. Han, Thickness effects on the microstructure and electrical/thermoelectric properties of co-evaporated Bi-Te thin films, *J Alloy Compd.* 767 (2018) 522 -527.

Reference (continue)

- [48] J.H. We, S.J. Kim, G.S. Kim, B.J. Cho, Improvement of thermoelectric properties of screen-printed Bi_2Te_3 thick film by optimization of the annealing process, *J. Alloys Compd.* 552 (2013) 107-110.
- [49] S. A. Semenkovich, B. T. Melekh, Thermodynamic Properties of Bi_2Te_3 , Bi_2Se_3 , Sb_2Te_3 , and Sb_2Se_3 , *Chem. Bonds in Solids* (1972) 159-162.
- [50] D. Music, K. Chang, P. Schmidt, F. N. Braun, M. Heller, S. Hermsen, P. J. Pöllmann, T. Schulzendorff, C. Wagner, On atomic mechanisms governing the oxidation of Bi_2Te_3 , *J. Condens. Matter Phys.* 29 (2017) 485705.
- [51] H. C. Kima, T. S. Oha, D.-B. Hyun, Thermoelectric properties of the p-type Bi_2Te_3 - Sb_2Te_3 - Sb_2Se_3 alloys fabricated by mechanical alloying and hot pressing, *J. Phys. Chem. Solids* 61 (2000) 743-749.
- [52] I. Bejenari, V. Kantser, Thermoelectric properties of bismuth telluride nanowires in the constant relaxation-time approximation, *Phys. Rev. B* 78 (2008) 115322.
- [53] M. Takashiri, S. Tanaka, H. Hagino, K. Miyazaki, Strain and grain size effects on thermal transport in highly-oriented nanocrystalline bismuth antimony telluride thin films. *Int. J. Heat Mass Tran.* 76 (2014) 376-384.
- [54] M. Akashiri, S. Tanaka, K. Miyazaki, H. Tsukamoto. Cross-plane thermal conductivity of highly oriented nanocrystalline bismuth antimony telluride thin films. *J Alloy Compd.* 490 (2010) L44-L47.
- [55] M. S. Dresselhaus, G. Chen, M. Y. Tang, R. G. Yang, H. Lee, D. Z. Wang, Z. F. Ren, J.-P. Fleurial, P. Gogna, New directions for low-dimensional thermoelectric materials. *Adv. Mater.* 19 (2007) 1043-1053.
- [56] C. J. Vineis, A. Shakouri, A. Majumdar, M. G. Kanatzidi, Nanostructured thermoelectrics: big efficiency gains from small features, *Adv. Mater.* 22 (2010) 3970-3990.
- [57] X. B. Zhao, X. H. Ji, Y. H. Zhang, T. J. Zhu, J. P. Tu, X. B. Zhang, Bismuth telluride nanotubes and the effects on the thermoelectric properties of nanotube-containing nanocomposites, *Appl. Phys. Lett.* 86 (2005) 062111.

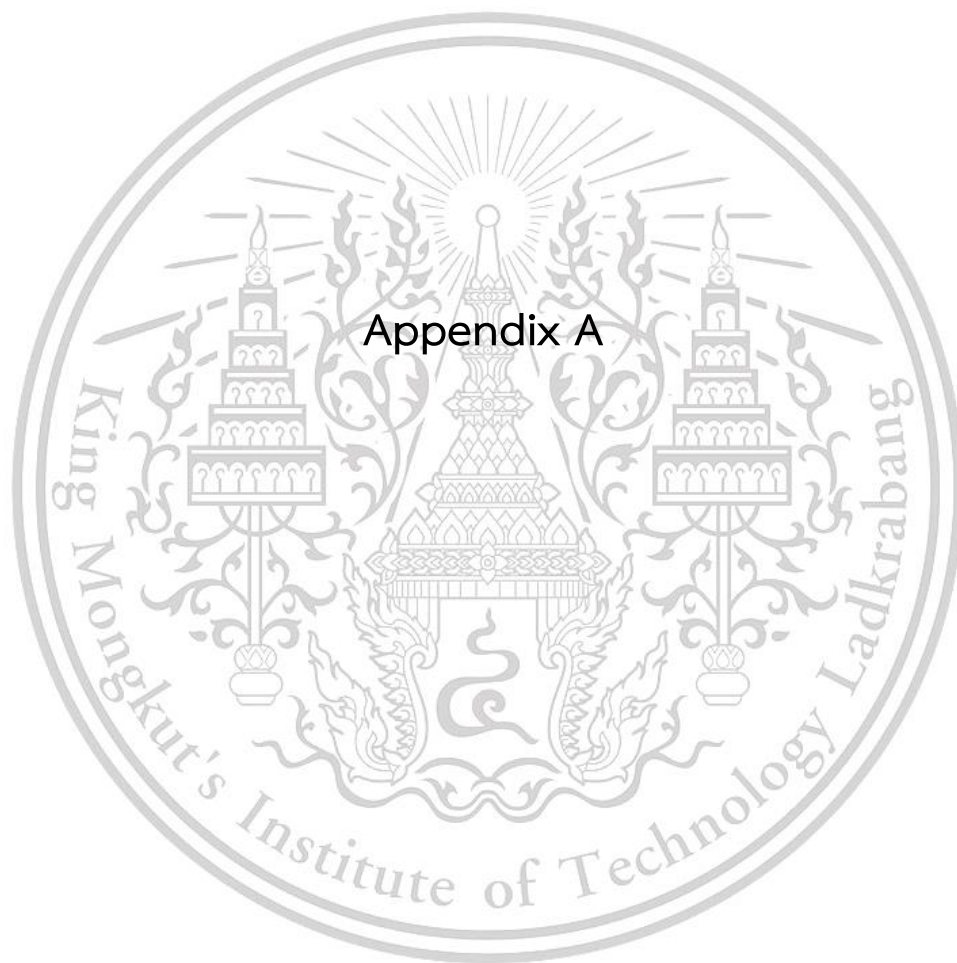
Reference (continue)

- [58] W. Xie, X. Tang, Y. Yan, Q. Zhang, T. M. Tritt, Unique nanostructures and enhanced thermoelectric performance of melt-spun BiSbTe alloys, *Appl. Phys. Lett.* 94 (2009) 102111.
- [59] J.-J. Shen, T.-J. Zhu, X.-B. Zhao, S.-N. Zhang, S.-H. Yang, Z.-Z. Yin, Recrystallization induced in situ nanostructures in bulk bismuth antimony tellurides: a simple top down route and improved thermoelectric, *Energy Environ. Sci.* 3 (2010) 1519-1523.
- [60] L. Hu, H. Wu, T. Zhu, C. Fu, J. He, P. Ying, X. Zhao, Tuning multiscale microstructures to enhance thermoelectric performance of n-type bismuth-telluride-based solid solutions. *Adv. Energy Mater.* 5 (2015) 1500411.
- [61] P. Fan, P.-C. Zhang, G.-X. Liang, F. Li, Y.-X. Chen, J.-T. Luo, X.-H. Zhang, S. Chen, Z.-H. Zheng, High-performance bismuth telluride thermoelectric thin films fabricated by using the two-step single-source thermal evaporation, *J. Alloys Compd.* 819 (2020) 153027.
- [62] H.-S. Kim, Z. M. Gibbs, Y. Tang, H. Wang, G. J. Snyder, Characterization of Lorenz number with Seebeck coefficient measurement, *Appl. Mater.* 3 (2015) 041506.
- [63] N.-W. Park, W.-Y. Lee, J.-E. Hong, T.-H. Park, S.-G. Yoon, H. Im, H. S. Kim, S.-K. Lee, Effect of grain size on thermal transport in post-annealed antimony telluride thin films, 10 (2015) PMC4384892.
- [64] G. -J. Snyder, Application of the compatibility factor to the design of segmented and cascaded thermoelectric generators, *Appl. Phys. Lett.*, 84 (2004) 2436-2438.
- [65] M.-K. Han, B.-G. Yu, Y. Jin, S.-J. Kim, A synergistic effect of metal iodide doping on the thermoelectric properties of Bi₂Te₃, *Inorg. Chem. Front.* 4 (2017) 881-888.
- [66] M.-K. Han, J. Hwang, S.-J. Kim, Improved thermoelectric properties of n-type Bi₂Te₃ alloy deriving from two-phased heterostructure by the reduction of CuI with Sn, *J. Mater. Sci. Mater. Electron.* 30 (2018) 1282–1291.
- [67] M.-K. Han, Y. Jin, D.-H. Lee, S.-J. Kim, Thermoelectric Properties of Bi₂Te₃: CuI and the effect of its doping with Pb atoms, *Materials*, 10 (2017) 1235.



This material is reserved for educational use only, not allowed for commercial use.

Forbidden to modify the content, and cite the document when use.




This material is reserved for educational use only, not allowed for commercial use.

Forbidden to modify the content, and cite the document when use.



Experimental Study on Flexible Bismuth Telluride Thin Films Deposited by DC Sputtering at Different Powers

SUPASAK KIANWIMOL,¹ PORNSIRI WANARATTIKAN,²
RACHSAK SAKDANUPHAB,^{3,4} PRAYOONSAK PLUENGPHON,²
THITI BOVORNANARAKS,⁵ and APARPORN SAKULKALAVEK ^{1,4,6}

1.—Department of Physics, Faculty of Science, King Mongkut's Institute of Technology Ladkrabang, Bangkok 10520, Thailand. 2.—Division of Physical Science, Faculty of Science and Technology, Huachiew Chalermprakiet University, Samutprakarn 10540, Thailand. 3.—College of Advanced Manufacturing Innovation, King Mongkut's Institute of Technology Ladkrabang, Bangkok 10520, Thailand. 4.—Thailand Center of Excellence in Physics, Commission on Higher Education, 328 Si-Ayuttaya Road, Bangkok 10400, Thailand. 5.—Extreme Conditions Physics Research Laboratory, Physics of Energy Materials Research Unit, Department of Physics, Faculty of Science, Chulalongkorn University, Bangkok 10330, Thailand. 6.—e-mail: Aparporn.sa@kmitl.ac.th

Bismuth telluride (Bi_2Te_3) thin films have been deposited onto polyimide sheet substrates by direct-current (DC) magnetron sputtering at different powers and their microstructure, composition, and electrical and thermoelectrical properties studied. The experimental results indicated that the sputtering power was the key parameter determining their thermoelectric properties. X-ray diffraction analysis confirmed the highly (015) preferred orientation of the films. The Te content and grain size depended on the sputtering power. The power factor of Bi_2Te_3 deposited by DC sputtering at power of 60 W was comparable to that obtained for highly (001) Bi_2Te_3 thin film.

Key words: Flexible bismuth telluride, thermoelectric thin film, DC sputtering, sputtering power

INTRODUCTION

Thin-film thermoelectric materials have potential for use in wearable devices. Bi_2Te_3 thin film is one of the best thermoelectric materials for room-temperature applications because of its relatively high figure of merit, defined as $ZT = S^2\sigma T/k$, where S is the Seebeck coefficient (V/K), σ is the electrical conductivity (S/m), k is the thermal conductivity (W/m K), and T is absolute temperature (K). Low-dimensional structures, particularly thin-film structures, have been proposed to achieve low thermal conductivity and high ZT . Physical vapor deposition and chemical vapor deposition techniques have been used for deposition of Bi_2Te_3 thin films, including thermal evaporation,¹ metal-organic chemical

vapor deposition (MOCVD),² pulsed laser deposition (PLD),³ and radiofrequency (RF) magnetron sputtering.^{4–13} RF magnetron sputtering is one of the most effective methods for obtaining thermoelectric thin films with good performance via further optimization of deposition parameters such as the sputtering pressure⁹ and power,¹⁰ annealing temperature,¹¹ and substrate temperature.¹⁴

In the work presented herein, DC magnetron sputtering was employed to deposit Bi_2Te_3 films using a Bi_2Te_3 ceramic target, due to the sufficiently conductive target and the lower cost and complexity of this technique compared with RF magnetron sputtering. In addition, DC magnetron sputtering is the technique most widely used in industry. The chemical composition, microstructure, and electrical and thermoelectric properties of the Bi_2Te_3 films deposited using different sputtering powers were investigated for the first time.

(Received September 17, 2018; accepted February 27, 2019)

This material is reserved for educational use only, not allowed for commercial use.

Published online: 07 March 2019

Forbidden to modify the content, and cite the document when use.

EXPERIMENTAL PROCEDURES

Bismuth telluride films were sputtered onto polymer sheet substrates (DuPont™ Kapton® polyimide films) using different DC sputtering powers. First, the polyimide substrates were cleaned in an ultrasonic bath with methanol followed by deionized water, then dried with N₂. The substrates were then loaded into the vacuum chamber. A Bi₂Te₃ sputtering target with diameter of 3 inches and purity of 99.9% was used for the sputtering process. The base pressure in the vacuum chamber before the deposition process was 2.5×10^{-5} mbar; presputtering was performed at 40 W for 4 min to clean the target surface, followed by preheating of the substrate at 400°C for 15 min. The DC sputtering power was varied from 50 W to 70 W, while the sputtering time was fixed at 6 min. Cross-sectional images and the chemical composition of the Bi₂Te₃ films were obtained by field-emission scanning electron microscopy (FE-SEM, JEOL-JSM-7001F) and energy-dispersive spectrometry (EDS, Oxford X-MAX 50 mm²), respectively. The x-ray diffraction (XRD) technique was used to analyze the crystalline structure of the Bi₂Te₃ films (PANalytical-EMPYR-EAN). The carrier mobility and carrier concentration of the bismuth telluride thin films were determined by Hall-effect measurements (Ecopia, HMS3000) at room temperature. The Seebeck coefficient and electrical conductivity were measured using a ZEM-3 instrument (ULVAC-RIKO) in the temperature range between 50°C and 300°C.

RESULTS AND DISCUSSION

Effect of Sputtering Power on Composition

The Te content of the Bi₂Te₃ films deposited under different sputtering powers was obtained by EDS analysis in several different areas of the film to investigate the effect of the sputtering power on their composition. EDS spectra showed only Bi and Te peaks, without impurities, with different Bi:Te

ratios as shown in Fig. 1. As the sputtering power was increased from 50 W to 70 W, the average %Te of the sputtered films changed to 59.28 at.%, 57.26 at.%, and 56.72 at.%, respectively, indicating a decrease in the Te content with increasing sputtering power. As the sputtering power is increased, the argon ions become more energetic and hence could release more energy to target atoms during sputtering, thereby affecting the ion energy (E_i) and sputtering yield (Y)¹⁵ given by Eq. 1:

$$Y(E_i) = \frac{3.56}{U_0} \frac{Z_t Z_p}{(Z_t^2 + Z_p^2)^{\frac{1}{2}}} \frac{M_p}{M_t + M_p} \alpha \left(\frac{M_t}{M_p} \right) S_n(\varepsilon), \quad (1)$$

where U_0 is the surface binding energy per atom. The surface binding energies of Bi and Te are 2.163 eV and 2.171 eV, respectively.¹⁶ (Z , M)_{t,p} are the target and projectile atomic number and mass, respectively. α is the sputtering efficiency¹⁶ given by Eq. 2:

$$\alpha = 0.08 + 0.164 \left(\frac{M_t}{M_p} \right)^{0.4} + 0.0145 \left(\frac{M_t}{M_p} \right)^{1.29}, \quad (2)$$

where $S_n(\varepsilon)$ is the nuclear stopping power per atom, given by Eq. 3:¹⁷

$$S_n(\varepsilon) = \frac{0.5 \ln(1 + \varepsilon)}{\varepsilon + 0.14\varepsilon^{0.42}}, \quad (3)$$

where the reduced energy ε is given by Eq. 4:

$$\varepsilon = \frac{0.03255}{Z_t Z_p (Z_t^2 + Z_p^2)^{\frac{1}{2}}} \frac{M_t}{M_t + M_p} E_i. \quad (4)$$

Using Eq. 1, one can calculate the sputtering yield ratio of Te/Bi with high-energy argon particles (as shown in Fig. 2). The sputtering yield ratio decreases with increasing argon energy. The trend in the sputtering yield ratio is consistent with our experimental data.

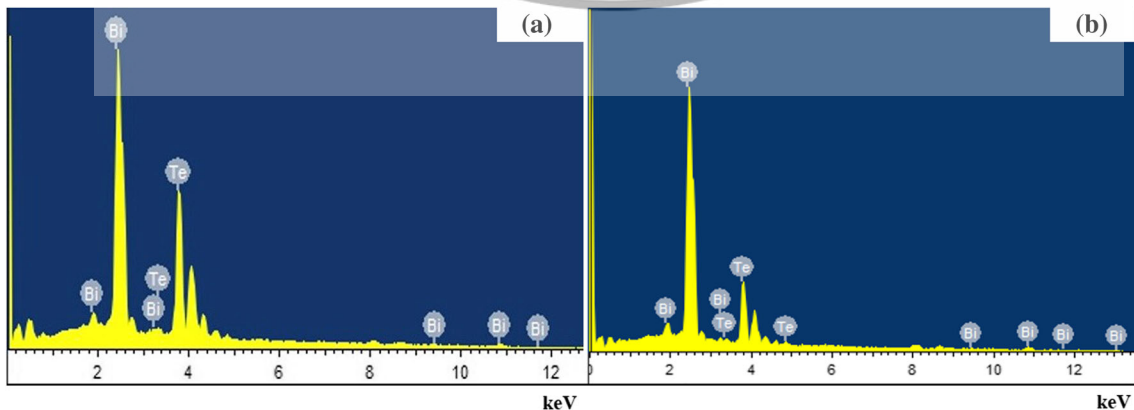


Fig. 1. EDS spectra of Bi₂Te₃ thin films deposited at sputtering power of (a) 50 W and (b) 70 W.

This material is reserved for educational use only, not allowed for commercial use.

Forbidden to modify the content, and cite the document when use.

Effect of Sputtering Power on Structural and Electrical Properties at Room Temperature

Figure 3 show the XRD spectra of the Bi_2Te_3 films prepared under different sputtering powers, revealing that (015) peak was the main diffraction peak for all samples. In addition, the intensity of (015) orientation increased as the sputtering power was increased from 50 W to 60 W, but decreased on further increase to 70 W.

Figure 4 show cross-sectional FE-SEM images of the Bi_2Te_3 films prepared using different sputtering powers, revealing an increase in film thickness with increasing sputtering power. The thickness of the Bi_2Te_3 films lay in the range of $1.35 \mu\text{m}$ to $1.51 \mu\text{m}$. In addition, the sputtering power strongly influenced the surface structure and cross-section of these films deposited on a flexible substrate. Up to applied sputtering power of 60 W, the film showed dense columnar grain structure. Above sputtering

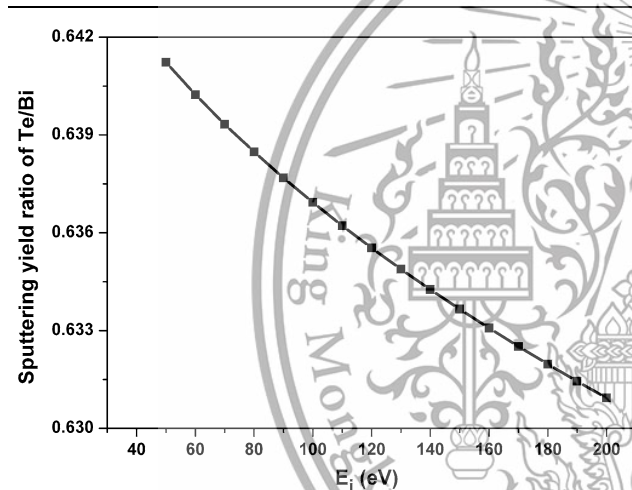


Fig. 2. Sputtering ratio between Te/Bi according to ion energy.

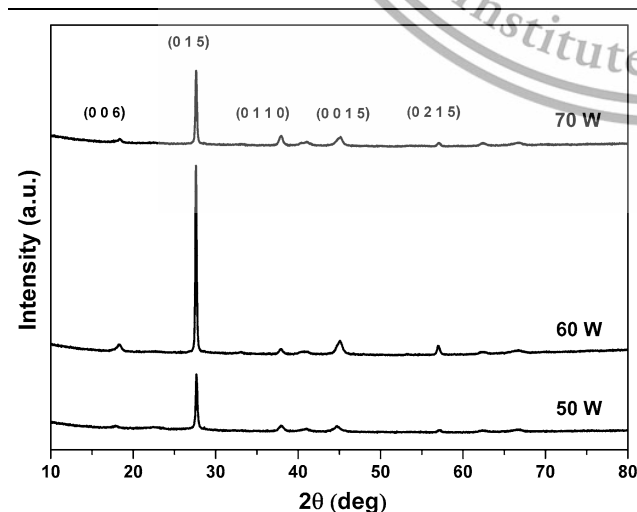


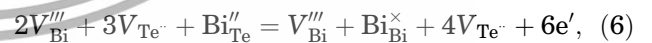
Fig. 3. XRD patterns of Bi_2Te_3 films prepared under different sputtering powers.

power of 60 W, the denseness of the structure began to decrease. By increasing the sputtering power applied, more atoms are sputtered from the target, and their higher energy contributes to the film growth. The crystallinity could be enhanced when increasing the sputtering power. It was found that the optimum sputtering power of 60 W produced the highest crystal quality.

According to Scherrer's formula (Eq. 5), the crystalline size (D) of Bi_2Te_3 obtained using different sputtering powers was calculated as

$$D = \frac{k\lambda}{\beta \cos \theta}, \quad (5)$$

where k is the Scherrer constant (typically 0.94), λ is the wavelength of the x-ray radiation (0.154056 nm), β is the full-width at half-maximum (FWHM) of the peak, and θ is the diffraction angle. The crystalline size increased from 30.5 nm to 38.9 nm when the sputtering power was increased to 60 W, but decreased with further increase of the sputtering power. These results show that the grain size in the films was larger than that in Bi_2Te_3 thin film deposited on polyamine substrate by RF sputtering (16.13 nm to 20.08 nm⁹), indicating that DC magnetron sputtering enhances the grain size compared with the RF magnetron sputtering technique. The carrier concentration, mobility, and electrical conductivity of the films obtained by sputtering at different powers were measured at room temperature, and the obtained data are summarized in Table I. The variation in the carrier concentration can be explained by the lattice defects in and chemical composition of the Bi_2Te_3 thin films. Based on a theoretical model, antisite defects Bi'_{Te} can form easily because Bi atoms can be substituted at Te vacancies (V_{Te}) due to the small difference in electronegativity ($\Delta\chi = 0.3$) between bismuth (Bi) and tellurium (Te).¹⁸ Then, antisite defects (Bi'_{Te}) lead to formation of vacancy defects (V'''_{Bi}).¹⁹ The following relation for the interaction between vacancies and antisites has been proposed²⁰:



where e' is the electron generated from the interaction, resulting in an increase in the electron concentration in the Bi_2Te_3 films. It can be seen that a decrease in the at.% of Te will lead to an increase in the electron density. This result indicates that the carrier concentration in the Bi_2Te_3 films was increased by Te vacancies. Therefore, stoichiometric composition plays a vital role in reducing the carrier concentration of Bi_2Te_3 films.²¹ In this work, a carrier concentration of $1.17 \times 10^{21} \text{ cm}^{-3}$ was achieved at 59.28 at.% Te content, close to results obtained on sputtered films by Huang et al.¹²

The carrier mobility was approximately $15.82 \text{ cm}^2/\text{Vs}$ with grain size of 38.9 nm when

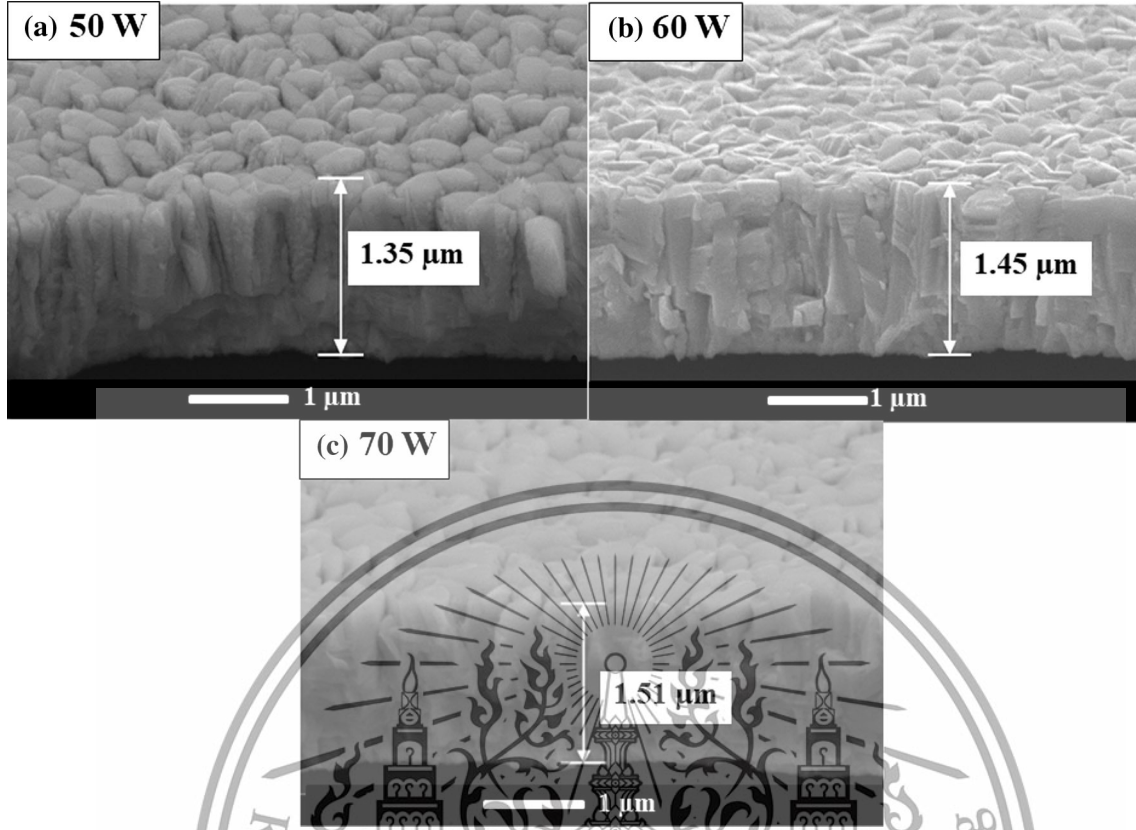


Fig. 4. Surface structure and cross-sectional FE-SEM images of Bi_2Te_3 films obtained by sputtering at power of (a) 50 W, (b) 60 W, and (c) 70 W.

Table I. Crystalline size and electrical properties of Bi_2Te_3 thin films deposited at various sputtering powers

Sputtering Power (W)	Crystalline Size (nm)	Carrier Concentration ($\times 10^{21}/\text{cm}^3$)	Mobility (cm^2/Vs)	Conductivity ($\times 10^3/\Omega \text{ cm}$)
50	30.5	1.17	8.04	1.50
60	38.9	1.41	15.82	3.57
70	34.2	1.66	10.04	2.67

sputtering at power of 60 W, but decreased to $10.04 \text{ cm}^2/\text{Vs}$ when the sputtering power was increased to 70 W with grain size of 34.2 nm. The effect of carrier scattering in-grain and at grain boundaries on the carrier mobility is normally determined by the corresponding mechanisms.^{22,23} Based on the FE-SEM results, the number of grain boundaries in the cross-section of the Bi_2Te_3 thin films directly affected the carrier mobility. Grain boundaries act as barriers to carrier motion, reducing their mobility in the Bi_2Te_3 thin films. According to these data, the carrier mobility of the Bi_2Te_3 thin films depended on the grain size and grain boundaries.

Effect of Sputtering Power on Thermoelectric Properties

Figure 5a, b, and c show the variation in the electrical conductivity, Seebeck coefficient, and

power factor, respectively, measured on Bi_2Te_3 films in the temperature range of 50°C to 300°C .

As shown in Fig. 5a, for all the samples, the conductivity first increased then decreased with increasing temperature. The maximum value of electrical conductivity ($\sim 4.5 \times 10^5 \text{ S/m}$) was achieved in the Bi_2Te_3 film sputtered at 60 W, due to the significantly increased mobility and high carrier concentration ($\sim 10^{21} \text{ cm}^{-3}$) in this sample. The Seebeck coefficient (S) of the Bi_2Te_3 thin films measured as a function of temperature is shown in Fig. 5b. The results show that all the films exhibited n -type semiconducting behavior, since their S values are negative, a result confirmed by the Hall-effect measurements. The S value for a degenerate semiconductor can be expressed as

$$S = \frac{2k_B^2 T m^*}{3eh^2} \left(\frac{\pi}{3n} \right)^{2/3} \left(\frac{3}{2} + \gamma \right), \quad (7)$$

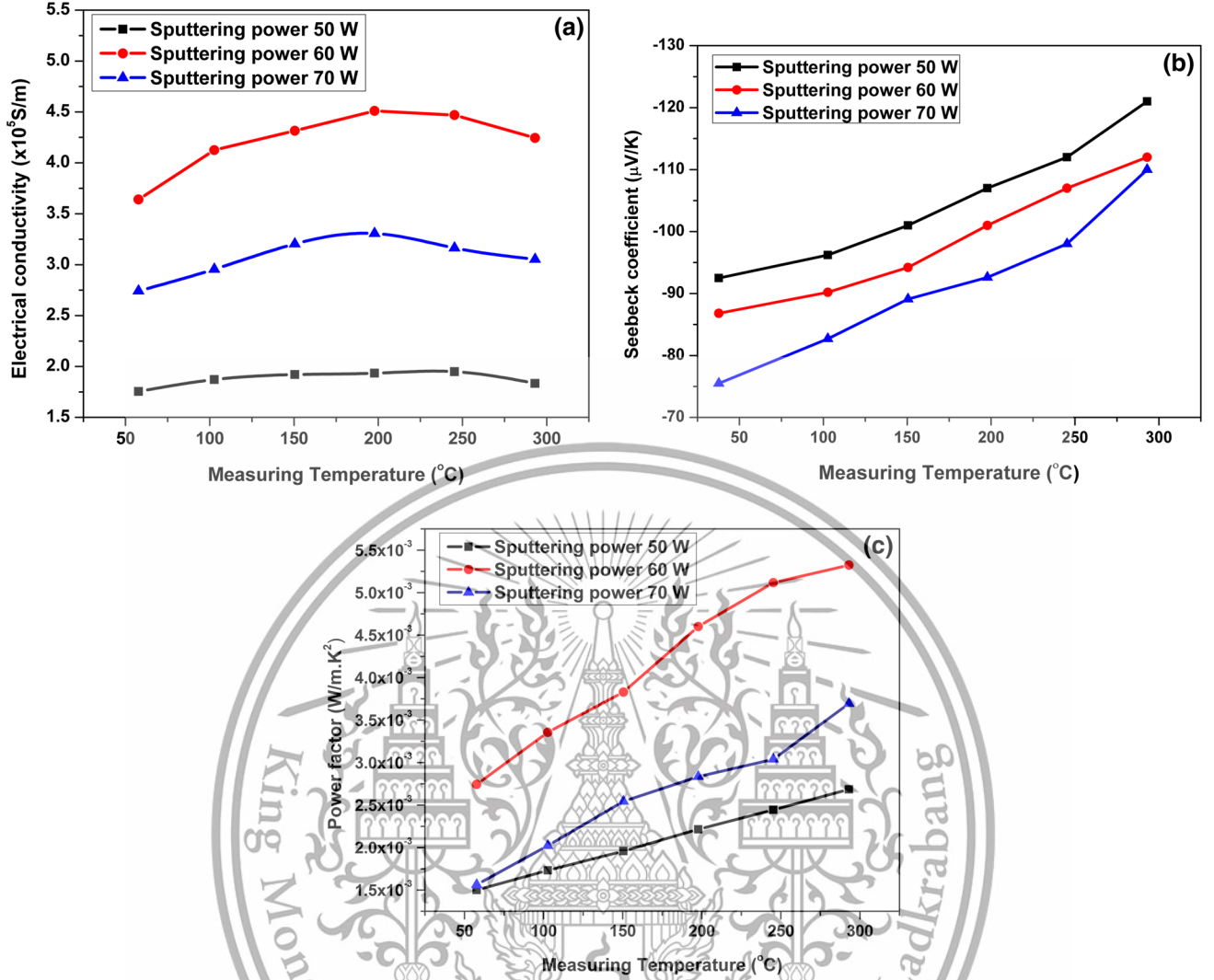


Fig. 5. Temperature dependence of (a) electrical conductivity, (b) Seebeck coefficient, and (c) power factor of Bi₂Te₃ films obtained by sputtering at different powers.

where k_B is the Boltzmann constant, h is the reduced Planck constant, and γ is the scattering factor. Equation 7 indicates that S is directly proportional to the measurement temperature (T) but inversely proportional to the carrier concentration n . Figure 5b shows that S increases with increasing temperature and a higher carrier concentration will decrease the S value. These results are consistent with Eq. 7. In addition, the effect of the film thickness on the S value is expressed in Eq. 8,

$$S_F = S_B \left[1 - \frac{3(1-p)}{8} \frac{U}{1+U} \frac{\lambda_B}{t} \right], \quad (8)$$

where S_B , p , and λ_B are the Seebeck coefficient, the specularly parameter, and the mean free path of carriers, respectively.^{13,24} $U = \partial \ln \lambda_B / \partial \ln E$ is the exponent of the energy term for the mean free path of the form $\lambda_B = \lambda_0 E^p$. The exponent is 3/2, -1/2, and 0 for impurity ion scattering, lattice acoustic

scattering, and optical phonon scattering, respectively; t is the thickness of the thin film. According to Eq. 8, the S value of the films should be directly proportional to their thickness. According to Fig. 5b, the highest Seebeck coefficient (S) was obtained for the film sample deposited at 50 W (with thickness of 1.35 μm), and the S value remained in the range of 90 $\mu\text{V/K}$ to 125 $\mu\text{V/K}$. However, the sample deposited at 70 W (with thickness of 1.51 μm) showed the smallest S value of approximately 75 $\mu\text{V/K}$ to 100 $\mu\text{V/K}$. This result indicates that the carrier concentration has a dominant effect on the S value.

The thermoelectric power factor (PF) is used to evaluate the performance of thermoelectric materials. The PF of the Bi₂Te₃ films (Fig. 5c) increased with increasing temperature. The maximum PF value of $5.4 \times 10^{-3} \text{ W/m K}^2$ was obtained at temperature of 300°C for the film sputtered at 60 W. Table II compares the room-temperature thermoelectric properties of Bi₂Te₃ thin films deposited by

Table II. Comparison of room-temperature thermoelectric properties of Bi₂Te₃ thin films deposited by RF and DC magnetron sputtering methods

Deposition Parameter		Bi ₂ Te ₃ Thin Film Type	σ ($\times 10^4$ S/m)	S (μ V/K)	PF ($\times 10^{-3}$ W/m K ²)
DC/RF	Power (W)				
RF	200 ($\phi_{\text{target}} = 12.7$ cm)	Highly (00l)	10.41	126	1.7 ¹¹
DC	18 ($\phi_{\text{target}} = 7.5$ cm)	Highly (00l)	9.12	92.42	0.71 ¹⁴
DC	18 ($\phi_{\text{target}} = 7.5$ cm)	Highly (00l)	18.4	145.6	3.91 ²⁵
DC	60 ($\phi_{\text{target}} = 7.6$ cm)	Highly (015)	35.8	85.6	2.5 (this work)

Deposition Condition
 Two-step treatment; electron-beam irradiation at 1.07 MGy and thermal annealing at 300°C
 Deposition temperature 400°C
 Induced by MgO substrates
 Preheating temperature 400°C

the RF and DC magnetron sputtering methods. The PF of the Bi₂Te₃ film deposited by DC sputtering power at 60 W in this work is comparable to that obtained for highly (00l) Bi₂Te₃ thin film.^{11,14,25}

CONCLUSIONS

Bi₂Te₃ thin films were deposited on flexible substrate by DC magnetron sputtering at different powers and their composition, microstructure, and electrical and thermoelectric properties studied. XRD analysis confirmed that all the films exhibited highly (015) preferred orientation. The Te content decreased as the sputtering power was increased. The power factor of Bi₂Te₃ deposited by DC sputtering at power of 60 W was comparable to that obtained for highly (00l) oriented Bi₂Te₃ thin film. These results suggest that DC sputtering at appropriate conditions represents another good approach for enhancing the thermoelectric properties.

ACKNOWLEDGMENTS

This research was financially supported by Thailand Research Fund (TRF) ID Code RSA6180013.

REFERENCES

1. L.M. Goncalves, C. Couto, P. Alpuim, A.G. Rolo, F. Volklein, and J.H. Correia, *Thin Solid Films* 518, 2816 (2010).
2. A. Giani, A. Boulouz, F. Pascal-Delannoy, A. Foucaran, E. Charles, and A. Boyer, *Mater. Sci. Eng. B* 64, 19 (1999).
3. A. Bailini, F. Dnnati, M. Zamboni, V. Russo, M. Passoni, C.S. Casari, A. Li Bassi, and C.E. Bottani, *Appl. Surf. Sci.* 254, 1249 (2007).
4. S.J. Jeon, M. Oh, H. Jeon, S. Hyun, and H.J. Lee, *Microelectron. Eng.* 88, 541 (2011).
5. H.J. Lee, H.S. Park, S. Han, and J.Y. Kim, *Thermochim. Acta* 542, 57 (2012).
6. K. Agarwal and B.R. Mehta, *J. Appl. Phys.* 116, 083518 (2014).
7. M. Takashiri, K. Takano, and J. Hamada, *Thin Solid Films* 664, 100 (2018).
8. J.W. Park, S.T. Nguyen, Y. Luan, and J.S. Noh, *Mater. Des.* 110, 449 (2016).
9. P. Nuthongkum, R. Sakdanuphab, M. Horprathum, and A. Sakulkalavek, *J. Electron. Mater.* 46, 6444 (2017).
10. M. Goto, M. Sasaki, Y. Xu, T. Zhan, Y. Isoda, and Y. Shinohara, *Appl. Surf. Sci.* 407, 405 (2017).
11. K. Yamauchi and M. Takashiri, *J. Alloys Compd.* 698, 977 (2017).
12. H. Hung, W.L. Luan, and S.T. Tu, *Thin Solid Films* 517, 3731 (2009).
13. Z. Zeng, P. Yang, and Z. Hu, *Appl. Surf. Sci.* 268, 472 (2013).
14. H. Shang, H. Gu, Y. Zhong, F. Ding, G. Li, F. Qu, H. Zhang, Z. Dong, H. Zhang, and W. Zhou, *J. Alloys Compd.* 690, 851 (2017).
15. Z. Yu, C. Yan, T. Huang, W. Huang, Y. Yan, Y. Zhang, L. Liu, Y. Zhang, and Y. Zhao, *Appl. Surf. Sci.* 258, 5222 (2012).
16. M.P. Seah, C.A. Clifford, F.M. Green, and I.S. Gilmore, *Surf. Interface Anal.* 37, 444 (2005).
17. W.D. Wilson, L.G. Haggmark, and J.P. Biersack, *Phys. Rev. B* 15, 2458 (1977).
18. J. Horak, K. Cermák, and L. Koudelka, *J. Phys. Chem. Solids* 47, 805 (1986).
19. Z. Sary, J. Horák, M. Stordeur, and M. Stölzer, *J. Phys. Chem. Solids* 49, 29 (1988).
20. G.R. Miller and C.Y. Li, *J. Phys. Chem. Solids* 26, 173 (1965).

Experimental Study on Flexible Bismuth Telluride Thin Films Deposited by DC Sputtering at Different Powers

21. B. Fang, Z. Zeng, X. Yan, and Z. Hu, *J. Mater. Sci. Mater. Electron.* 24, 1105 (2013).
22. F.H. Hsu, N.F. Wang, Y.Z. Tsai, M.C. Chuang, Y.S. Cheng, and M.P. Hounng, *Appl. Surf. Sci.* 280, 104 (2013).
23. H. Yue, A. Wu, Y. Feng, X. Zhang, and T. Li, *Thin Solid Films* 519, 5577 (2011).
24. V.D. Das and P.G. Ganesan, *Mater. Chem. Phys.* 57, 57 (1998).
25. H. Shang, F. Ding, G. Li, L. Wang, F. Qu, H. Zhang, Z. Dong, H. Zhang, Z. Gao, W. Zhou, and H. Gu, *J. Alloys Compd.* 726, 532 (2017).

Publisher's Note Springer Nature remains neutral with regard to jurisdictional claims in published maps and institutional affiliations.





This material is reserved for educational use only, not allowed for commercial use.

Forbidden to modify the content, and cite the document when use.



ELSEVIER

Contents lists available at ScienceDirect

Surface & Coatings Technology

journal homepage: www.elsevier.com/locate/surfcoat

Effect of annealing temperature on thermoelectric properties of bismuth telluride thick film deposited by DC magnetron sputtering

Supasak Kianwimol^a, Rachsak Sakdanuphab^{b,c,d}, Narong Chanlek^e, Adul Harnwungmoung^f, Aparporn Sakulkalavek^{a,b,c,*}

^a Faculty of Science, King Mongkut's Institute of Technology Ladkrabang, Bangkok 10520, Thailand

^b College of Advanced Manufacturing Innovation, King Mongkut's Institute of Technology Ladkrabang, Bangkok 10520, Thailand

^c Thailand Center of Excellence in Physics, Commission on Higher Education, 328 Si-Ayuttaya Road, Bangkok 10400, Thailand

^d Electronic and Optoelectronic Device Research Unit, Faculty of Science, King Mongkut's Institute of Technology Ladkrabang, Bangkok 10520, Thailand

^e Synchrotron Light Research Institute (Public Organization), 111 University Avenue, Muang District, Nakhon Ratchasima 30000, Thailand

^f Faculty of Science and Technology, Rajamangala University of Technology Suvarnabhumi, Nonthaburi 11000, Thailand

ARTICLE INFO

Keywords:

Bismuth telluride
Thick films
Annealing treatment
Single-leg thermoelectric
DC sputtering

ABSTRACT

We report the thermoelectric properties of thick bismuth-telluride (Bi_2Te_3) films deposited on polyimide substrates by DC magnetron sputtering and annealed at various temperatures (150–350 °C). The influence of annealing temperature on the microstructure and electronic structure of thick Bi_2Te_3 films is discussed. In this work, the annealed film at 250 °C has the best thermoelectric property due to highest electrical conductivity and Seebeck coefficient. The main effect of annealing temperature was really helpful to improve crystalline structure and enhance carrier mobility, whereas the carrier concentration was reduced due to the volatile of tellurium atom during annealing. Chemical states of bound and unbound atoms (Bi , Bi^{3+} , Te , and Te^{2-}) on the surface play an important role in electrical properties. The exceed temperature caused the micro-crack formation and affect carrier transport by the scattering. The power factor of Bi_2Te_3 deposited by DC magnetron sputtering and annealed at 250 °C is comparable to the power factors of thick Bi_2Te_3 film deposited by various deposition techniques. The output power of single-leg, thick, thermoelectric Bi_2Te_3 film annealed at 250 °C as a function temperature generated a power of 0.98 μW at a temperature difference of 50 °C.

1. Introduction

The technology of thermoelectric power generation converts thermal energy directly into electricity and is used in several applications, such as mini-power-generation systems and powering wireless autonomous sensors [1–3]. Bismuth telluride (Bi_2Te_3) is one of best thermoelectric materials and has a high figure of merit near room temperature ($ZT = S^2\sigma T/K$, where S , σ , T , and K are the Seebeck coefficient, electrical conductivity, absolute temperature, and thermal conductivity, respectively) [4]. To increase power density, several studies of thermoelectric devices have used thin films, on the submicron or micron scale [5–7]. However, in applications, thermoelectric thin films still face challenges: for horizontal use, the problem involves the difference in the temperature between the hot and cold side and, for the vertical use, the problem is insufficient heat flowing into the thermoelectric material [8,9]. To solve these problems, we prepare thick Bi_2Te_3 films. In most studies, thick Bi_2Te_3 films are prepared by screen printing

[9,10] and electrochemical deposition [8,11–13]. However, these techniques lead to weak adhesion between the film and the supporting material, which can result in the release or breaking of the film. Thus, we used the sputtering technique to obtain good adhesion between material and substrate, and because it is a simple technique that requires less time than other techniques [14,15]. In addition, we use a substrate for flexible thermoelectrics to increase the efficiency of use with a variety of heat sources, such as car exhausts, the human body, etc.

In this work, thick, flexible Bi_2Te_3 films were deposited by DC magnetron sputtering, following which the thermoelectric properties were improved by annealing. The structure, composition, and thermoelectric properties of the Bi_2Te_3 films were then investigated. Finally, the output power was measured at various temperature differences.

* Corresponding author at: Faculty of Science, King Mongkut's Institute of Technology Ladkrabang, Bangkok 10520, Thailand.

E-mail address: Aparporn.sa@kmitl.ac.th (A. Sakulkalavek).

<https://doi.org/10.1016/j.surfcoat.2020.125808>

Received 10 December 2019; Received in revised form 30 March 2020; Accepted 16 April 2020

Available online 19 April 2020

0257-8972/ © 2020 Elsevier B.V. All rights reserved.

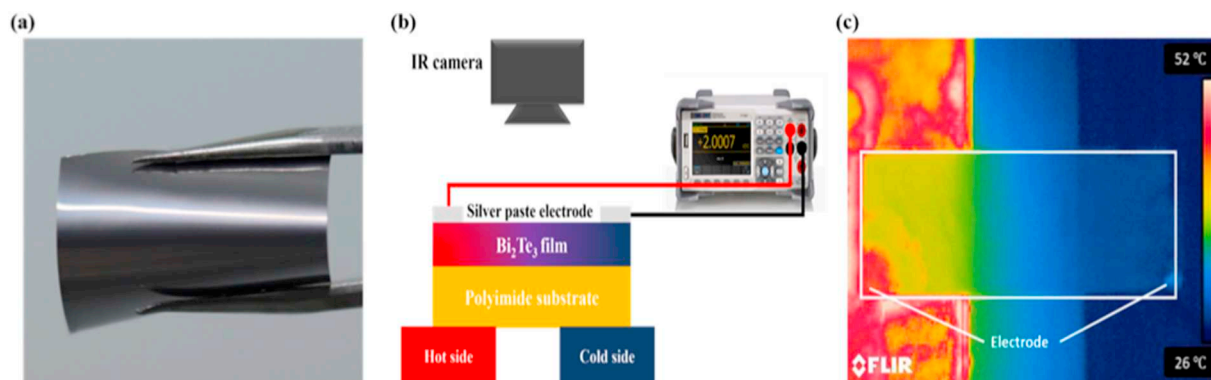


Fig. 1. (a) Photograph of thick bismuth telluride film deposited by DC magnetron sputtering on a flexible substrate. (b) Schematic illustration of apparatus for measuring power output from thick, single-leg Bi_2Te_3 film. (c) Infrared top-view image of Bi_2Te_3 film taken during measurement.

2. Experiment

Thick Bi_2Te_3 films were deposited on a polyimide-film substrate by using DC magnetron sputtering from a three-inch-diameter Bi_2Te_3 alloy target of 99.9% impurity. Before sputtering, the polyimide substrates were ultrasonicated in methanol, acetone, and deionized water for 15 minutes and then dried with nitrogen gas. Before deposition, the base pressure in the deposition chamber was 2.5×10^{-5} mbar, and pre-sputtering was done for 5 minutes to remove contamination from the target surface. Before deposition, the substrate was pre-heated to 350°C for 15 minutes. The DC sputtering power and pressure were maintained at 45 W and 1.8×10^{-2} mbar, respectively, and the sputtering time was fixed at 75 minutes. The films were annealed at 150, 250, and 350°C under an ambient argon atmosphere for 30 minutes.

Fig. 1(a) shows a photograph of a thick Bi_2Te_3 film, which can be flexed without cracking. The cross-sectional morphologies of the thick Bi_2Te_3 films were analyzed by using field emission scanning electron microscope (JEOL-JSM-7001F). The crystalline structure of thick Bi_2Te_3 films was analyzed by using x-ray diffraction (XRD, PANalytical-EMERYAN) with $\text{CuK}\alpha$ radiation ($\lambda = 0.154$ nm). The films were scanned over a 2θ range from 10° to 80° . The room-temperature carrier concentration and mobility of the thick Bi_2Te_3 films were investigated through Hall-effect measurements (Ecopia, HMS3000). All samples were investigated for the chemical state and chemical composition of surface using X-ray photoelectron spectroscopy (XPS) techniques at Beamline 5.3 (BL5.3) of SLRI. The electrical conductivity and Seebeck coefficient were measured by using a ZEM-3 (ULVAC-Riko) at 50 – 300°C . The thermoelectric power output of thick single-leg Bi_2Te_3 film was measured by using a heater and heat sink to create a temperature gradient and measuring the temperature difference with an infrared camera (FLIR E40) [see Fig. 1(b) and 1(c)]. The current and voltage produced between two silver-paste electrodes were measured by using a digital multimeter. The output voltage, current, and power produced by the thick single-leg Bi_2Te_3 film were measured at several temperature differences.

3. Results and Discussion

Fig. 2 shows XRD patterns of thick Bi_2Te_3 films annealed for 30 minutes at various temperatures. The results reveal that the films are polycrystalline, with a prominent peak at the (015, 1010) orientation for all samples. For post-annealing treatment, the relative intensity of the diffraction peak (110) slightly decreased, indicating a change in orientation of the Bi_2Te_3 structure. In addition, XRD spectra of annealed films at 150°C , 250°C and 350°C , show peak shift towards a lower diffraction angle compared with the as-deposited film. It means an expansion of lattice constant with respect to its equilibrium lattice constant. The peak shift increases with higher annealing temperature as

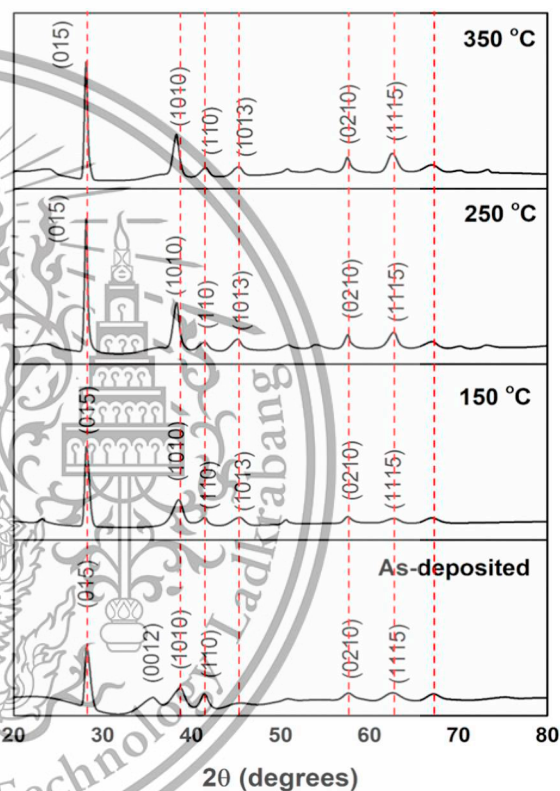


Fig. 2. X-ray diffraction patterns from thick Bi_2Te_3 films annealed for 30 minutes at various temperatures.

seen clearly from (1010) peak in Fig. 1. This result indicated that a tensile stress is induced in the thick Bi_2Te_3 films during the annealing treatment [16]. The average crystalline size (D) of Bi_2Te_3 annealed at the various temperatures was calculated by using the Williamson-Hall formula [17]

$$\beta \cos \theta = \frac{K\lambda}{D} + 4\epsilon \sin \theta, \quad (1)$$

where λ and β are the x-ray wavelength and integral breadth of the diffraction peak, respectively, θ is the Bragg diffraction angle, and ϵ is the microscopic strain. The average crystallite size of as-deposited film was calculated to be 14.5 nm, and increases from 23.8 to 28.9 nm as annealing temperature increased from 150 to 250°C (Table 1). However, the crystallite size slightly decreased from 28.9 to 27.4 nm with annealing temperature increasing from 250 to 350°C . This result suggested that the crystallite size is related to the annealing temperature.

The surface chemical composition of the thick Bi_2Te films was

Table 1
Calculated average grain size and Te content of thick Bi₂Te₃ films annealed at different temperatures.

Annealing temperature (°C)	βcosθ	Average grain size [D (nm)]	Te content (%)
As-deposited	0.0097	14.5	59.02
150	0.0083	23.8	58.79
250	0.0060	28.9	58.36
350	0.0063	27.4	57.38

analyzed by using x-ray photoelectron spectroscopy (XPS), which especially give information about chemical bonding state on the surface. Fig. 3 shows the XPS spectra of Bi 4f and Te 3d from the surface of the as-deposited and annealed Bi₂Te₃ thick films. It was found that Bi 4f core level with binding energies of 157.5 and 163.0 eV, corresponds to the states of Bi 4f_{7/2} and 4f_{5/2} as shown in Fig. 3(a). Fig. 3(b) shows Te 3d core level with binding energies of 572.5 and 583.0 eV, corresponds to the states of Te 3d_{5/2} and 3d_{3/2} [18]. However, a slightly peak shift is observed toward the lower binding energy side for the annealed films at 150 °C and 250 °C (in the circles). The XPS spectra are resolved into two chemical states of unbound (Bi) and bound (Bi³⁺) (in the inset of Fig. 3(c) and 3(d)) and unbound (Te) and bound (Te²⁻) (in the inset of Fig. 3(e) and 3(f)). The unbound states of bismuth and

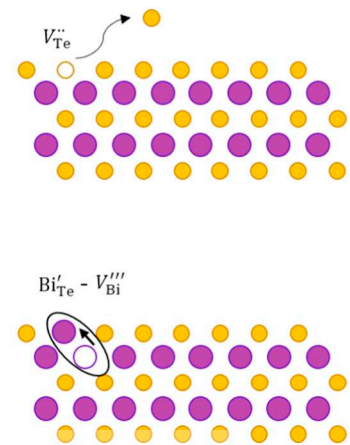


Fig. 4. Schematics of defect generation in Bi₂Te₃ atomic structure from the annealing process. In step 1, V_{Te}^{••} is formed by the volatile of tellurium atoms on surface. In step 2, a Bi_{Te}[']-V_{Bi}^{'''} pair is formed by the migration of bismuth atom from an adjacent Bi site.

telluride peaks (light blue line) have a slight shift (0.2 eV) toward the lower and higher binding from the bound states of bismuth and telluride peaks (blue line), respectively [19]. In annealing treatment, it

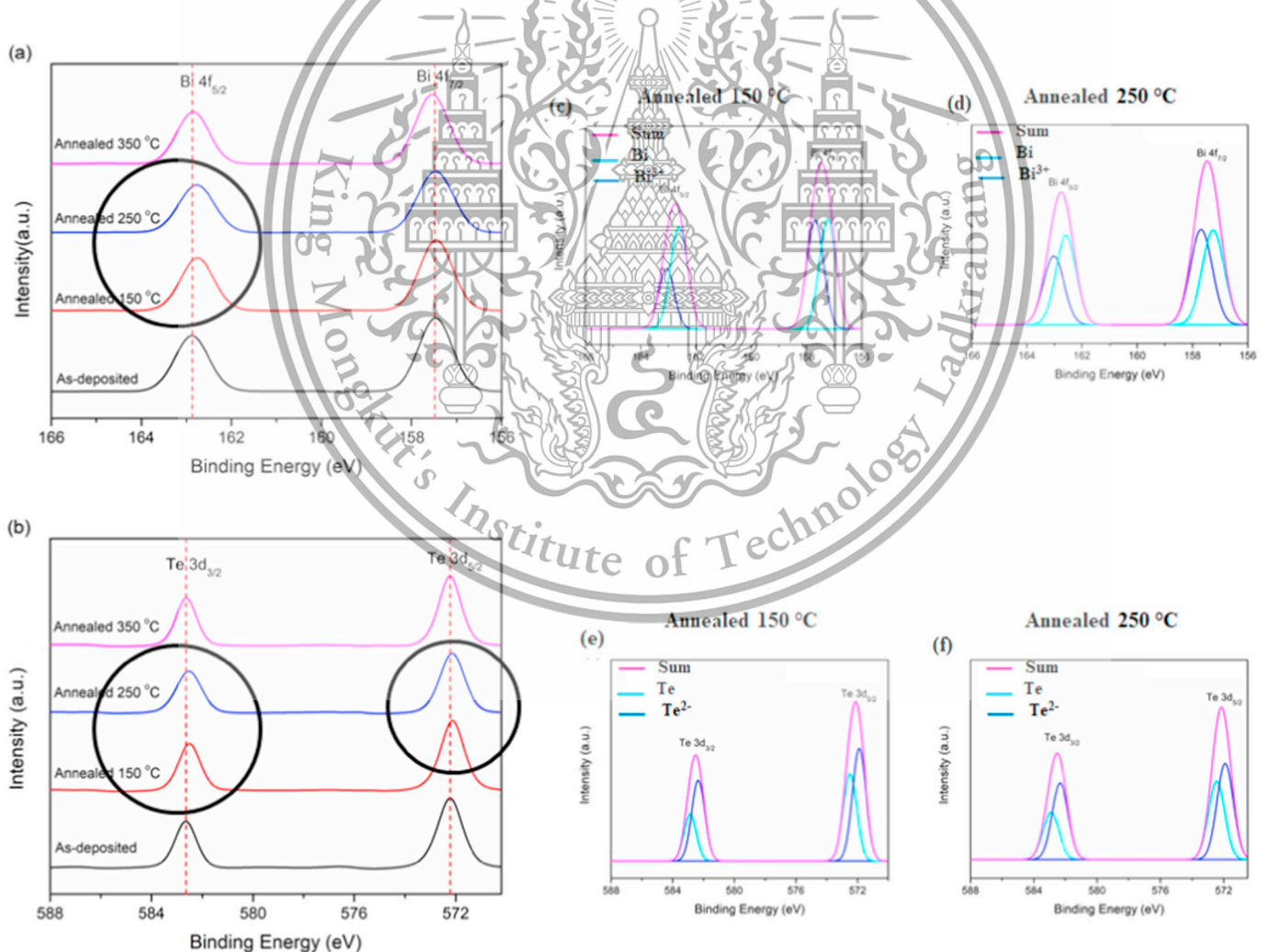


Fig. 3. XPS spectra of as-deposited and annealed thick Bi₂Te₃ films. (a) Bi 4f core level with binding energies of 157.5 and 163 eV, corresponds to the states of Bi 4f_{7/2} and 4f_{5/2}. (b) Te 3d core level with binding energies of 572.5 and 583 eV, corresponds to the states of Te 3d_{5/2} and 3d_{3/2}. The inset shows peaks fitting XPS data of Bi 4f_{7/2} and 4f_{5/2} for unbound (Bi) and bound (Bi³⁺) chemical states of annealed films at 150 °C (c) and 250 °C (d), and peaks fitting XPS data of Te 3d_{5/2} and 3d_{3/2} for unbound (Te) and bound (Te²⁻) chemical states of annealed films at 150 °C (e) and 250 °C (f). allowed for commercial use.

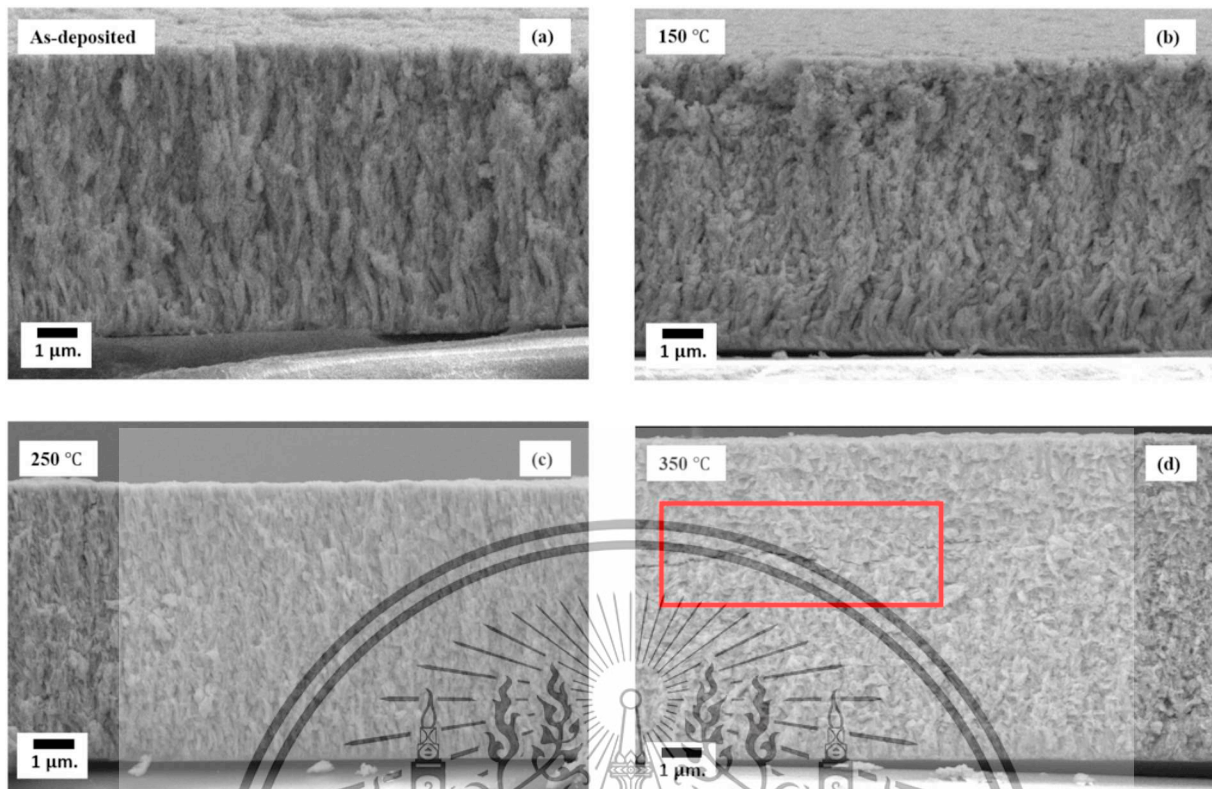
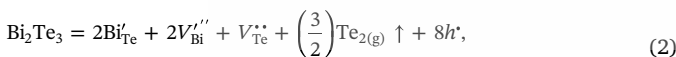


Fig. 5. Cross section of thick Bi_2Te_3 films (a) as-deposited and annealed at (b) 150 °C, (c) 250 °C, and (d) 350 °C.

takes energy to break the existing chemical bonds of Bi_2Te_3 . Bi ions (Bi^{3+}) and Te ions (Te^{2-}) resides at the surface with the metallic Bi and Te states. On the other hand, the XPS spectra of annealed thick film at 350 °C did not show significant difference from the as-deposited film. We speculate that the metallic Bi and Te migrate from the surface due to higher annealing temperature.

The influence of annealing temperature on electronic structure could be explained by the volatile of tellurium atoms during the annealing treatment. Fig. 4 shows the schematic model of defect generation in Bi_2Te_3 atomic structure from the annealing process. This model is developed from the J. Kim et. al. work [19]. At typical annealing temperature, the thermal energy that is absorbed to break the bonds in the Bi_2Te_3 structure and then cause the volatile of tellurium atom from surface [20]. The volatile of tellurium generates the tellurium vacancies ($V_{\text{Te}}^{\bullet\bullet}$, step 1), where it can be occupied by adjacent bismuth atom. That leads to the generation of the pair of bismuth vacancy ($V_{\text{Bi}}^{\bullet\bullet}$) and antisite defect ($\text{Bi}_{\text{Te}}^{\bullet}$), step 2. This process can be described by Equation (2) [21]



where h^{\bullet} is the resulting hole and \uparrow indicates the volatilization of tellurium. From Eq. (2) the volatile of tellurium generates hole, and the carrier concentration of n-type of Bi_2Te_3 films would be reduced by the compensation of holes. The atomic ratio of bismuth and tellurium may be estimated by using Equation (3)

$$\frac{\rho_{\text{Te}}}{\rho_{\text{Bi}}} = \frac{I_{\text{Te}}/S_{\text{Te}}}{I_{\text{Bi}}/S_{\text{Bi}}} \quad (3)$$

where ρ , I , and S are the atom density, integrated intensity, and the atomic sensitivity factor, respectively. This incorporates the calculated Bi $4f_{7/2}$ and Te $3d_{5/2}$ areas with $S_{\text{Bi}} = 2.9$ and $S_{\text{Te}} = 4.9$ for surface atoms [22]. Table 1 lists the calculated Te content of thick Bi_2Te_3 films annealed at different temperatures. The tellurium content decreases from

59.02 to 57.38 as the annealing temperature increases from 150 to 350 °C. This result indicates that elemental tellurium evaporates during annealing. The evaporation is attributed to the inequivalent atomic bonds at the surface of the annealed films, which is essential for the evaporation of elemental tellurium [20].

Fig. 5 shows a cross section of the as-deposited and annealed Bi_2Te_3 films. The film is about 10 μm thick and remains almost unchanged after annealing. As the annealing temperature increases from 150 to 250 °C [Fig. 5(b) and 5(c)], the crystallization and agglomeration of the thick films improve as the films begin to grow in from a columnar structure, confirming that the crystallization can be improved by annealing. However, Fig. 5(d) reveals a crack in the columnar film after annealing at 350 °C. The micro-cracks appeared at 350 °C is caused from the different coefficient of thermal expansion between polyimide substrate ($2.0 \times 10^{-5} \text{K}^{-1}$) [23] and bismuth telluride ($5.08 \times 10^{-5} \text{K}^{-1}$) [24]. At typical annealing temperature (350 °C), the thermal stress inside the film is large enough, which can initiate the micro-crack growth. These results indicate that the film crack degrades the crystalline structure of the film, which is consistent with the XRD spectra (cf. Fig. 2; the peak decreases after annealing at 350 °C). In addition, the average grain size (see Table 1) decreases from 28.9 to 27.4 nm.

Fig. 6(a) shows how annealing affects the room-temperature carrier concentration and mobility of the Bi_2Te_3 films. All films have a negative carrier concentration because they are n-type semiconductors; the Hall carrier concentration of the film decreases from 2.62×10^{20} to $0.7 \times 10^{20} \text{cm}^{-3}$ when annealing at 350 °C. The decrease in carrier concentration with annealing temperature is attributed to the evaporation of tellurium, which creates tellurium vacancies ($V_{\text{Te}}^{\bullet\bullet}$). Next, the antisite defect ($\text{Bi}_{\text{Te}}^{\bullet}$) and the bismuth vacancy ($V_{\text{Bi}}^{\bullet\bullet}$) become involved as bismuth enters the tellurium vacancies as shown in Equation (2). In addition, the mobility increases from 4.4 to 14.2 $\text{cm}^2 \text{V}^{-1} \text{s}^{-1}$ as the annealing temperature increases to 250 °C. The increase in average grain size (see Table 1) decreases the grain-boundary intensity and reduces carrier scattering at the grain boundaries. However, the

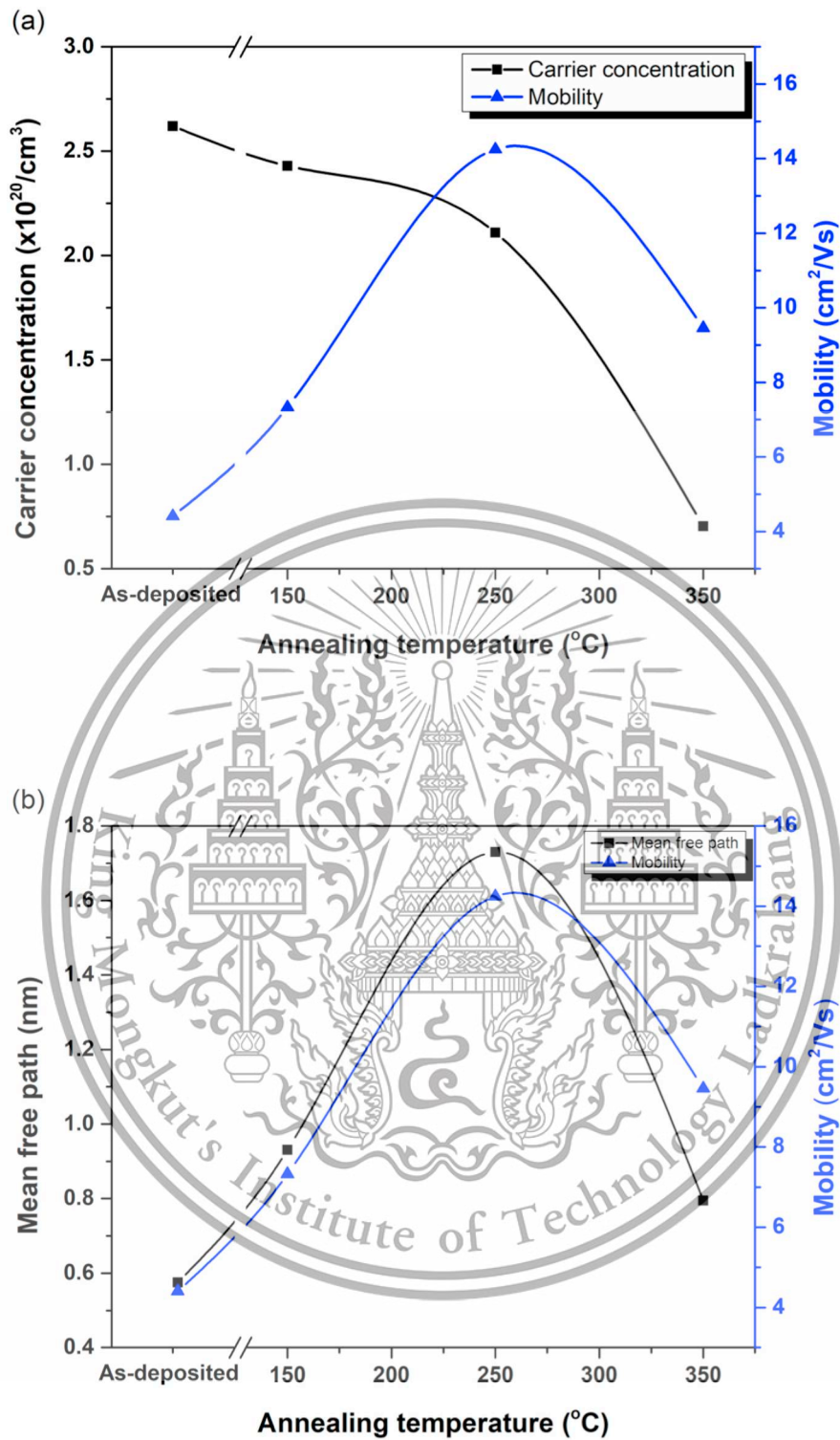


Fig. 6. Room temperature (a) Hall carrier concentration and carrier mobility; (b) mean free path and carrier mobility of thick Bi₂Te₃ films annealed at different temperatures.

mobility decreases to 9.46 cm² V⁻¹ s⁻¹ upon increasing the annealing temperature to 350 °C because the crystallization is degraded by the crack in the film [see Fig. 5(d)]. Fig. 6(b) shows the mean free path and mobility of the Bi₂Te₃ thick films. The carrier mean free path *l* can be calculated by using [25]

$$l = \frac{h}{2e} \left(\frac{3n}{\pi} \right)^{\frac{1}{3}} \mu, \quad (4)$$

where *h* and *e* > 0 are Planck's constant and the fundamental charge, respectively. Equation (4) indicates that the mean free path is related to carrier concentration and mobility. The *l* value of thick films increases from 0.57 to 1.73 nm as the annealing temperature increases to 250 °C and decreases to 0.79 nm as the annealing temperature rises from 250 to 350 °C. The transfer of carriers is involved by grain size and grain boundary preceding to increase of mobility. The decrease in the mean free path is confirmed by the crack in the film annealed at 350 °C,

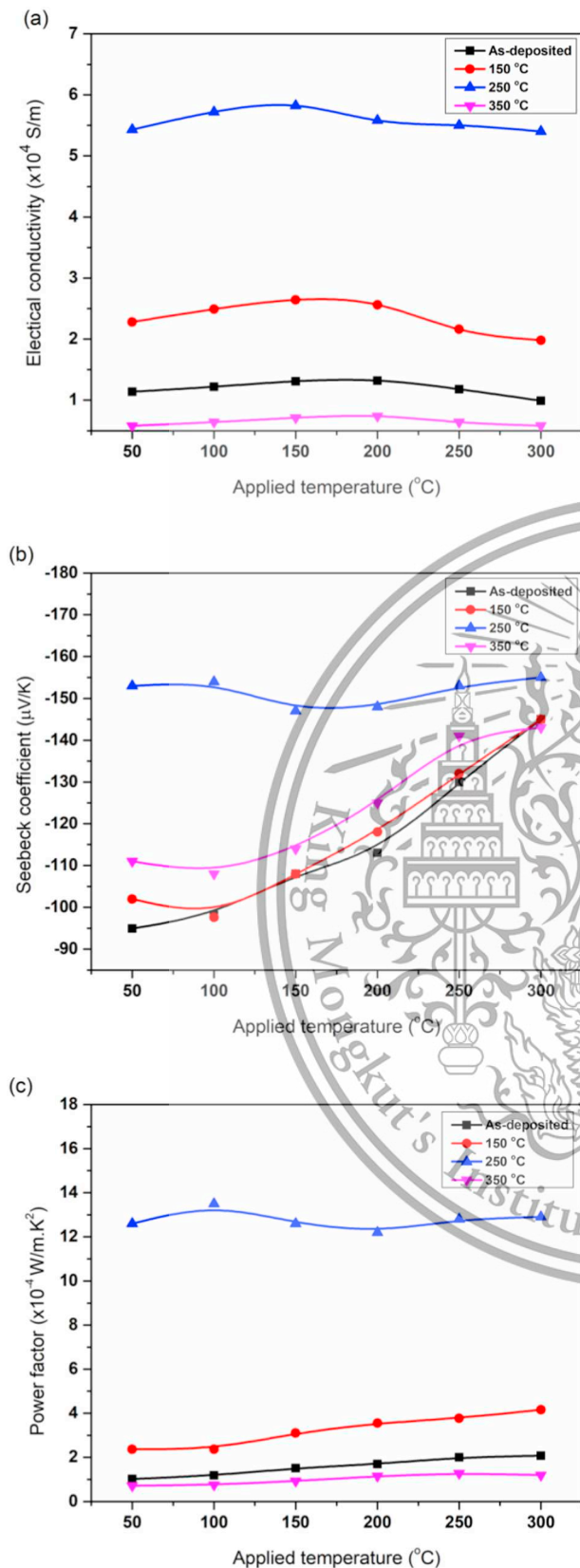


Fig. 7. Temperature dependent (a) electrical conductivity σ , (b) Seebeck coefficient S , and (c) power factor $S^2\sigma$ as functions of applied temperature for thick Bi₂Te₃ films annealed at different temperatures.

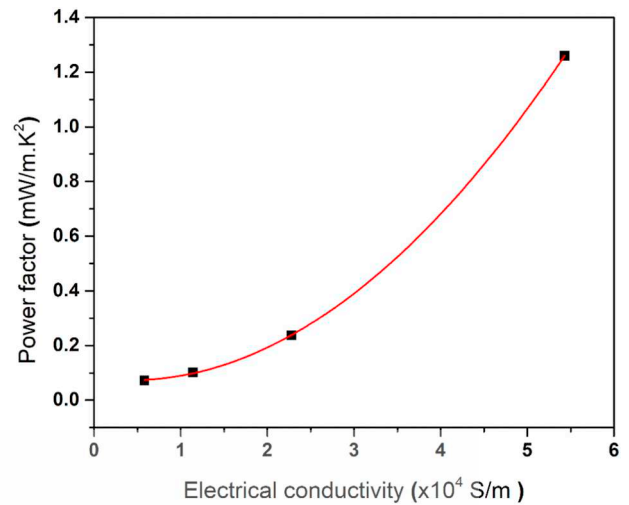


Fig. 8. Power factor as a function of electrical conductivity for thick Bi₂Te₃ films annealed at different temperatures.

which is due to resistance to carrier scattering.

Fig. 7(a)–7(c) show the electrical conductivity, Seebeck coefficient, and power factor, respectively, as a function of temperature for thick Bi₂Te₃ films annealed at different temperatures. Fig. 7(a) shows that, for all conditions, the electrical conductivity increases from 50 to 150 °C and then decreases with temperature. The electrical conductivity ranges from 0.99×10^4 to 1.32×10^4 S/m in as-deposited film and increases to 5.4×10^4 to 5.82×10^4 S/m in film annealed at 250 °C. The low electrical conductivity in as-deposited film is due to the low mobility and low crystallinity. Upon annealing the thick Bi₂Te₃ films, the crystallinity and mobility increases, which improves the electrical conductivity. However, the lowest electrical conductivity occurs in the film annealed at 350 °C (0.58×10^4 to 0.73×10^4 S/m), which may be attributed to low carrier concentration due to the volatilization of tellurium and the decreased mobility due to the cracked film annealed at 350 °C.

As shown in Fig. 7(b), the Seebeck coefficient of all Bi₂Te₃ films is negative, indicating that they are n-type semiconductors. The Seebeck coefficient ranges from -97 to -145 $\mu\text{V/K}$ in as-deposited film and increases to -147 to -155 $\mu\text{V/K}$ in film annealed at 250 °C, then decreases to -108 to -143 $\mu\text{V/K}$ in film annealed at 350 °C. Therefore, the thick Bi₂Te₃ film has a maximum Seebeck coefficient when annealed at 250 °C. The greater Seebeck coefficient in films annealed below 350 °C is due to the decrease in carrier concentration from 2.62×10^{20} to 2.11×10^{20} cm^{-3} [see Fig. 6(a)], which in turn is due to the reduced number of donor defects [26]. The Seebeck coefficient for a degenerate semiconductor is given by [15]

$$S = \frac{8\pi^2 k_B^2}{3eh^2} m^* T \left(\frac{\pi}{3n} \right)^{\frac{2}{3}} (1 + R), \quad (5)$$

where k_B is Boltzmann's constant, h is Planck's constant, m^* is the effective carrier mass, n is the carrier concentration, T is absolute temperature, and R is the scattering function. Equation (5) implies that the Seebeck coefficient is directly proportional to the measurement temperature and inversely proportional to carrier concentration. However, the Seebeck coefficient for a thick film annealed at 350 °C decreases because the carrier mean free path decreases [as shown in Fig. 6(b)], and the mean free path explains the degree of carrier scattering at defects in a grain. The increase in scattering decreases the mean free path, which decreases the Seebeck coefficient [27].

The thermoelectric power factor of thick Bi₂Te₃ films annealed at different temperatures was calculated by using the Seebeck coefficient and the electrical conductivity ($S^2\sigma$), with the result shown in Fig. 7(c). These results indicate that the power factor increases with annealing

Table 2
Room-temperature power factor of thick Bi_2Te_3 films deposited by various techniques.

Deposition technique	Electrical conductivity (S/cm)	Seebeck coefficient ($\mu\text{V}/\text{K}$)	Power factor ($\text{mW K}^{-2} \text{m}^{-1}$)	Treatment process
Dispenser printing [28]	22	-230	0.12	Curing treatment at 350 °C
Co-evaporation [29]	363	-202	1.5	Substrate temperature 250 °C
Screen-printing [9]			2.1	Annealing treatment at 250 °C (Bi and Te powders ambient)
Thermally assisted sputtering method [30]	500	-150	1.12	
DC sputtering (this work)	502	-155	1.21	Annealing treatment at 250 °C (argon atmosphere)

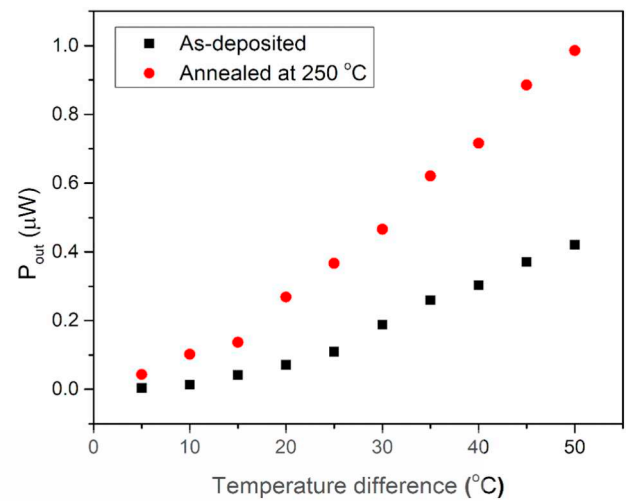


Fig. 9. Power output of single-leg, thick, thermoelectric Bi_2Te_3 film as a function of temperature difference for as-deposited film and film annealed at 250 °C.

temperature up to 250 °C, then decreases as the annealing temperature increases further. The maximum power factor is $13.5 \times 10^{-4} \text{ W K}^{-2} \text{ m}^{-1}$, which occurs at the annealing temperature of 250 °C.

Fig. 8 shows the power factor as a function of electrical conductivity for thick Bi_2Te_3 films. The increased electrical conductivity is attributed mainly to the improved crystallinity and the increase in carrier mobility upon annealing. The maximum power factor occurs at the maximum electrical conductivity, which is obtained at the annealing temperature of 250 °C. Thus, the power factor of thick Bi_2Te_3 films improves significantly with respect to the electrical conductivity. Table 2 compares the thermoelectric properties of thick Bi_2Te_3 films deposited by room-temperature DC magnetron sputtering with dispenser printing [28], co-evaporation [29], screen-printing [9], and thermally assisted sputtering [30]. The power factor for Bi_2Te_3 deposited by DC magnetron sputtering and annealed at 250 °C is comparable to that obtained with various other deposition techniques for thick Bi_2Te_3 film.

Fig. 9 shows the power output of single-leg, thick, thermoelectric Bi_2Te_3 film as a function of temperature difference ($\Delta T = 5\text{--}50$ °C). The as-deposited film generates a power output of 3.78 nW at $\Delta T = 5$ °C and 0.42 μW at $\Delta T = 50$ °C. The annealed film at 250 °C generates an output power of 43.24 nW at $\Delta T = 5$ °C and 0.98 μW at $\Delta T = 50$ °C. This result indicates that annealing improves the output power of single-leg, thick, thermoelectric Bi_2Te_3 film.

4. Conclusion

In summary, we investigated in this work how annealing affects the structural and thermoelectric properties of thick Bi_2Te_3 films deposited by DC magnetron sputtering. The XRD patterns show that the films have a hexagonal structure. After annealing, the volatile of tellurium atom occur with the formation of the pair of bismuth vacancy (V_{Bi}) and antisite defect (Bi_{Te}). The micro-cracks appeared at 350 °C is caused from the different coefficient of thermal expansion between polyimide substrate and bismuth telluride. The maximum electrical conductivity of 5.84 S/m is obtained by annealing at 250 °C. The Seebeck coefficient ranges from 97 to 145 $\mu\text{V}/\text{K}$ in as-deposited film and increases to 147 to 155 $\mu\text{V}/\text{K}$ upon annealing at 250 °C. The maximum power factor of 1.21 $\text{mW K}^{-2} \text{ m}^{-1}$ is obtained by annealing at 250 °C. The maximum power output of 0.98 μW at a temperature difference of 50 °C for thick, thermoelectric Bi_2Te_3 film is obtained by annealing at 250 °C.

CRediT authorship contribution statement

Supasak Kianwimol: Conceptualization, Methodology. **Rachsak Sakdanuphab:** Formal analysis. **Narong Chanlek:** Formal analysis. **Adul Harnwungmoung:** Validation. **Aparporn Sakulka-lavek:** Writing - review & editing.

Declaration of competing interest

The authors declare that they have no known competing financial interests or personal relationships that could have appeared to influence the work reported in this paper.

Acknowledgments

This research was financially supported by Thailand Research Fund (TRF) ID code RSA6180013. The authors thank King Mongkut's Institute of Technology, Ladkrabang, Thailand for student fund support.

References

- [1] D.M. Rowe, CRC Handbook of Thermoelectrics, first ed., FL : CRC Press, Boca Raton, 1995.
- [2] D.M. Rowe, C.M. Bhandari, Modern Thermoelectrics, Va. : Reston Pub. Co, Reston, 1983.
- [3] S. Beeby, N. White, Energy Harvesting for Autonomous Systems, MA : Artech House, Norwood, 2010.
- [4] H.J. Goldsmid, Thermoelectric Refrigeration, Plenum, New York, 1964.
- [5] D.G. Cahill, W.K. Ford, K.E. Goodson, G.D. Mahan, A. Majumdar, H.J. Maris, R. Merlin, S.R. Phillpot, Nanoscale thermal transport, J. Appl. Phys. 93 (2003) 793–818, <https://doi.org/10.1063/1.1524305>.
- [6] L.D. Hicks, M.S. Dresselhaus, Effect of quantum-well structures on the thermoelectric figure of merit, Phys. Rev. B 47 (1993) 12727–12731, <https://doi.org/10.1103/PhysRevB.47.12727>.
- [7] R. Venkatasubramanian, Lattice thermal conductivity reduction and phonon localization like behavior in superlattice structures, Phys. Rev. B 61 (2000) 3091–3097, <https://doi.org/10.1103/PhysRevB.61.3091>.
- [8] J.-P. Fleurial, A. Borshchevsky, M.A. Ryan, W.M. Phillips, J.G. Snyder, T. Caillat, E.A. Kolawa, J.A. Herman, P. Mueller, M. Nicolet, Development of Thick-Film Thermoelectric Microcoolers Using Electrochemical Deposition, Mater. Res. Soc. Symp. Proc. 545 (1999) 493–500, <https://doi.org/10.1557/PROC-545-493>.
- [9] J.H. We, S.J. Kim, G.S. Kim, B.J. Cho, Improvement of thermoelectric properties of screen-printed Bi₂Te₃ thick film by optimization of the annealing process, J. Alloys Compd. 552 (2013) 107–110, <https://doi.org/10.1016/j.jallcom.2012.10.085>.
- [10] S.J. Kim, J.H. We, G.S. Kim, B.J. Cho, Thermoelectric properties of P-type Sb₂Te₃ thick film processed by a screen-printing technique and a subsequent annealing process, J. Alloys Compd. 582 (2014) 177–180, <https://doi.org/10.1016/j.jallcom.2013.07.195>.
- [11] S. Li, H.M.A. Soliman, J. Zhou, M.S. Toprak, M. Muhammed, D. Platzek, P. Ziolkowski, E. Müller, Effects of Annealing and Doping on Nanostructured Bismuth Telluride Thick Films, Chem. Mater. 20 (2008) 4403–4410, <https://doi.org/10.1021/cm800696h>.
- [12] S. Li, M.S. Toprak, H.M.A. Soliman, J. Zhou, M. Muhammed, D. Platzek, E. Müller, Fabrication of Nanostructured Thermoelectric Bismuth Telluride Thick Films by Electrochemical Deposition, Chem. Mater. 18 (2006) 3627–3633, <https://doi.org/10.1021/cm060171o>.
- [13] N.H. Trung, K. Sakamoto, N.V. Toan, T. Ono, Synthesis and Evaluation of Thick Films of Electrochemically Deposited Bi₂Te₃ and Sb₂Te₃ Thermoelectric Materials, Materials 10 (2017) 154, <https://doi.org/10.3390/ma10020154>.
- [14] H. Huang, W.-L. Luan, S.-T. Tu, Influence of annealing on thermoelectric properties of bismuth telluride films grown via radio frequency magnetron sputtering, Thin Solid Films 517 (2009) 3731–3734, <https://doi.org/10.1016/j.tsf.2009.01.015>.
- [15] K. Singkaselit, A. Sakulka-lavek, R. Sakdanuphab, Effects of annealing temperature on the structural, mechanical and electrical properties of flexible bismuth telluride thin films prepared by high-pressure RF magnetron sputtering, Adv. Nat. Sci.: Nanosci. Nanotechnol. 8 (2017) 035002, <https://doi.org/10.1088/2043-6254/aa7222>.
- [16] S. Liu, N. Peng, Y. Bai, D. Ma, F. Ma, K. Xu, Self-formation of thickness tunable Bi₂Te₃ nanoplates on thin films with enhanced thermoelectric performance, RSC Adv 6 (2016) 31668–31674, <https://doi.org/10.1039/C5RA26835D>.
- [17] V.D. Mote, Y. Purushotham, B.N. Dole, Williamson-Hall analysis in estimation of lattice strain in nanometer-sized ZnO particles, J. Theor. App. Mech-Pol 8 (2012) 2251–2235, <https://doi.org/10.1186/2251-7235-6-6>.
- [18] J.F. Moulder, W.F. Stickle, P.E. Sobol, K.D. Bomben, Handbook of X-ray Photoelectron Spectroscopy, Perkin-Elmer, Eden Prairie, Minnesota, USA, 1992.
- [19] J. Kim, E.H. Shin, M.K. Sharma, K. Ihm, O. Dugerjav, C. Hwang, H. Lee, K.T. Ko, J.H. Park, M. Kim, H. Kim, M.H. Jung, Observation of Restored Topological Surface States in Magnetically Doped Topological Insulator, Sci. Rep. 9 (2019) 1331, <https://doi.org/10.1038/s41598-018-37663-8>.
- [20] X. Duan, Y. Jiang, Annealing effects on the structural and electrical transport properties of n-type Bi₂Te_{2.7}Se_{0.3} thin films deposited by flash evaporation, Appl. Surf. Sci. 256 (2010) 7365–7370, <https://doi.org/10.1016/j.apsusc.2010.05.069>.
- [21] Z. Starý, J. Horák, M. Stordeur, M. Stölzer, Antisite defects in Sb_{2-x}Bi_xTe₃ mixed crystals, J. Phys. Chem. Solids 49 (1988) 29–34, [https://doi.org/10.1016/0022-3697\(88\)90130-8](https://doi.org/10.1016/0022-3697(88)90130-8).
- [22] C.D. Wagner, Sensitivity factors for XPS analysis of surface atoms, J. Electron. Spectrosc. Relat. Phenom. 32 (1983) 99–102, [https://doi.org/10.1016/0368-2048\(83\)85087-7](https://doi.org/10.1016/0368-2048(83)85087-7).
- [23] T. Yoo, K. Kim, W. Jang, The effect of the ring opening polymerization and chain spacing on the coefficient of thermal expansion and modulus of polyimide, J. Appl. Polym. Sci. 42607 (2015) 1–9, <https://doi.org/10.1002/app.42607>.
- [24] Z. Xiong, X. An, Z. Li, Phase transition, electronic, elastic and thermodynamic properties of Bi₂Te₃ under high pressure, J. Alloys Compd. 586 (2014) 392–398, <https://doi.org/10.1016/j.jallcom.2013.10.062>.
- [25] S. Shena, W. Zhua, Y. Deng, H. Zhaob, Y. Peng, C. Wang, Enhancing thermoelectric properties of Sb₂Te₃ flexible thin film through microstructure control and crystal preferential orientation engineering, Appl. Surf. Sci. 414 (2017) 197–204, <https://doi.org/10.1016/j.apsusc.2017.04.074>.
- [26] L.D. Zhao, B.-P. Zhang, W.S. Liu, H.L. Zhang, J.-F. Li, Effects of annealing on electrical properties of n-type Bi₂Te₃ fabricated by mechanical alloying and spark plasma sintering, J. Alloy Compd. 467 (2009) 91–97, <https://doi.org/10.1016/j.jallcom.2007.12.063>.
- [27] G. YuanWen, H. YueZhou, Z. LinLi, Impact of grain size on the Seebeck coefficient of bulk polycrystalline thermoelectric materials, Chinese Sci Bull 55 (2010) 16–21, <https://doi.org/10.1007/s11434-009-0705-2>.
- [28] D. Madan, A. Chen, P.K. Wright, J.W. Evans, Dispenser printed composite thermoelectric thick films for thermoelectric generator applications, J. Appl. Phys. 109 (2011) 034904, <https://doi.org/10.1063/1.3544501>.
- [29] H. Shen, S. Lee, J. Kang, T. Eom, H. Lee, C. Kang, S. Han, Thickness effects on the microstructure and electrical/thermoelectric properties of co-evaporated Bi-Te thin films, J. Alloy Compd. 767 (2018) 522–527, <https://doi.org/10.1016/j.jallcom.2018.07.125>.
- [30] M. Mizoshiri, M. Mikami, K. Ozaki, p-Type Sb₂Te₃ and n-Type Bi₂Te₃ Films for Thermoelectric Modules Deposited by Thermally Assisted Sputtering Method, Jpn. J. Appl. Phys. 52 (2013) 06GL071–06GL076, <https://doi.org/10.7567/JJAP.52.06GL07>.

Author biography

Name	Mr. Supasak Kianwimol
Date of Birth	19 August 1994
Address	129/2 Village No. 3, Donpru Sub-district, SiPrachan District, Suphanburi, Thailand, 72140
Education	(2012-2016) Bachelor of Science in GPA: 3.02 (King Mongkut's Institute of Technology Ladkrabang) (2016-2018) Master of Science in GPA: 3.81 (King Mongkut's Institute of Technology Ladkrabang)
Scholarship	King Mongkut's Institute of Technology Ladkrabang for student fund support
Academic Publication(s)	- S. Kianwimol, P. Wanaarattikan, R. Sakdanuphab, P. Pluengphon, T. Bovornratanaraks, A. Sakulkalavek, Experimental Study on Flexible Bismuth Telluride Thin Films Deposited by DC Sputtering at Different Powers, J. Electron. Mater. 48 (2019) 3490-3496, https://doi.org/10.1007/s11664-019-07100-1 . - S. Kianwimol, R. Sakdanuphab, N. Chanlek, A. Harnwungmoung, A. Sakulkalavek, Effect of annealing temperature on thermoelectric properties of bismuth telluride thick film deposited by DC magnetron sputtering, Surf. Coat. Technol. 393 (2020) 125808, https://doi.org/10.1016/j.surfcoat.2020.125808 .